EXPERIMENTS ON
ENTRAINMENT, MIXING AND CHEMICAL REACTIONS IN TURBULENT JETS AT LARGE SCHMIDT NUMBER

Thesis by
Werner Johann Anton Dahm

In Partial Fulfillment
of the Requirements for the Degree of
Doctor of Philosophy

California Institute of Technology
Pasadena, California

1985
(Submitted May 3, 1985)

To my parents,

Kaethe Elisabeth and Werner Karl Dahm

ACKNOWLEDGEMENTS

This work has involved valuable contributions from many people, with whom I have been fortunate to have had the chance to work. Outstanding among these have been Prof. Paul Dimotakis, who was the advisor and motivator for this work and provided of an endless source of creative suggestions, and Dr. Gene Broadwell, whose penetrating insight led to innumerable fruitful discussions from which many of the ideas in this work were born.

I am also indebted to many of my fellow graduate students in the Aeronautics Department at Caltech. Among these, Dr. Manooch Koochesfahani, whose earlier experience with the photodiode arrays proved invaluable, Dr. Godfrey Mungal, with whom I had many useful technical discussions, and Dr. Dan Lang, who provided his unique expertise with electronics and computers, deserve special mention.

My wife, Gisela, deserves particular thanks for her enduring patience and support, without which this work could not have been possible.

Lastly, I would like to acknowledge the personal financial support of the Donald Wills Douglas Prize Fellowship and the A.R.C.S. Fellowship. This research was supported, in part, by the Air Force Office of Scientific Research (AFOSR) under Grant no. 83-0213 and Contract no. F49620-79-0159 , by the Energy and Environmental Research Corporation (EERC) under Contract no. 8400-28 on behalf of the Environmental Protection Agency (EPA), and by the Gas Research Institute (GRI) under Grant no. 5083-260-0878 .

ABSTRACT

Entrainment, mixing and chemical reactions are investigated in the far field of steady, axisymmetric, momentum-driven, turbulent jets issuing into an unconfined, quiescent medium in the large Schmidt number (liquid-phase) regime. Visualization experiments using both passive and chemically sensitive planar laser induced fluorescence (LIF) techniques show the importance of large scale transport in the jet far field, and suggest that entrainment, mixing and chemical reactions in the far field are dominated by a large scale organization of the flow. Successive instantaneous profiles of the jet fluid concentration along the axial and radial directions in the jet far field are measured by combining these LIF techniques with direct, high-resolution, linear photodiode array imaging and high-speed digital data acquisition. These imaging measurements have revealed an axial similarity concentration variable for which probability density functions (PDFs) in the jet far field are self-similar along rays. A chemical reaction method is presented which allows the self-similar form of these PDFs to be measured with full resolution at all scales of transport and mixing. Furthermore, these imaging measurements have shown that instantaneous radial profiles of the jet fluid concentration do not resemble the mean concentration profile. Specifically, unmixed ambient fluid is found deep within the jet and the composition of molecularly mixed fluid within large regions in the jet is approximately uniform. The results from these experiments are interpreted in the context of a simple conceptual model for large scale organization of entrainment, mixing and chemical reactions in the far field of turbulent jets.

TABLE OF CONTENTS

APPENDICES

LIST OF FIGURES

LIST OF TABLES

LIST OF SYMBOLS

Symbol	Description
c	jet fluid concentration
c^*	reference jet fluid concentration
c_ϕ	concentration at the mixture ratio ϕ, equation (4.12)
C	dye concentration
C_o	dye concentration in pure jet fluid
C^*	reference dye concentration
d_o	physical diameter of the jet source
d^*	jet momentum diameter, Appendix A.2
D	molecular diffusivity
$f(\psi;\eta)$	mixed fluid part of the similarity PDF, equation (4.11)
$F(c;\chi,\eta)$	mixed fluid part of the conventional PDF, equation (4.10)
g	radial self-similar concentration, equation (5.1)
$\bar{g}_m$	mean self-similar concentration of mixed fluid
$h(\xi)$	transfer function, Appendix E.3
$I[\xi]$	beam attenuation per unit length, Appendix E.3
J_o	jet momentum flux
k	chemical reaction rate constant
L	dye path length in calibration cell, Appendix B.2
$\dot{m}_o$	jet source mass flux
$\dot{m}(x)$	local jet mass flux, equation (A.1)
M	molar concentration
$p_o(\eta,t)$	instantaneous unmixed ambient fluid probability
$\bar{p}_o(\eta)$	time-averaged unmixed ambient fluid probability

$P(\xi,t)$	laser beam power
$P_o(t)$	beam power entering calibration cell, Appendix B.2
r	radial coordinate
Re	Reynolds number; $\frac{u\delta}{\nu}$
s	jet breakpoint length
Sc	Schmidt number; $\frac{\nu}{D}$
t	time
u	local centerline axial component of velocity
$U(c)$	Heaviside unit function, equation (4.13)
u_o	uniform jet exit velocity
x	axial coordinate
x_o	virtual origin
δ	local jet visual diameter
$\delta(c)$	delta function of concentration, equation (4.10)
$\delta(\psi)$	delta function of similarity concentration, equation (4.11)
ε	dissipation, equation (C.5)
ζ	linear beam attenuation constant, equation (B.3)
η	dimensionless radial coordinate, r/x
λ	coefficient in concentration scaling law, equation (A.20)
λ_D	strain-limited diffusion length, equation (C.12)
λ_ν	viscous (Kolmogorov) length
$\Lambda(\chi)$	defined in equation (A.18)
μ	mass mixture ratio, equation (4.4)
ν	kinematic viscosity
ξ	beam propagation coordinate
ξ^*	beam reference location, equation (E.3)

ρ	density
ρ_o	uniform jet fluid density
ρ_∞	ambient fluid density
$\Delta\rho$	density excess or deficit $(\rho-\rho_\infty)$
σ	strain rate, equation (C.8)
τ_M	local large scale time, equation (C.1)
τ_ν	local small scale time, equation (C.5)
τ_D	molecular diffusion time, equation (C.13)
τ_r	chemical reaction time, equation (C.15)
ϕ	mixture ratio for chemical reaction
χ	dimensionless axial coordinate, equation (A.10)
$\chi_e(\phi)$	entrainment distance, equation (3.2)
$\chi_m(\phi)$	molecular mixing distance, equation (3.2)
ψ	similarity concentration, equation (4.5)
ψ_ϕ	similarity concentration at the ratio ϕ, equation (4.14)

$f(\eta)$	self-similar profile, defined in equation A.16a
$g(\eta)$	" " A.16b
$h(\eta)$	" " A.16c
$i(\eta)$	" " A.16d
$j(\eta)$	" " A.16e
$k(\eta)$	" " A.16f
$l(\eta)$	" " A.16g

I_1	integral invariant, defined in equation A.19a
I_2	" " A.19b
I_3	" " A.19c
I_4	" " A.19d

$\overline{(\quad)}$	time-averaged component
$(\quad)'$	fluctuating component
$(\dot{\ })$	time derivative
$(\quad)_\nu$	quantity at the Kolmogorov scale
$(\quad)_{rms}$	root-mean-square

CHAPTER 1

INTRODUCTION

1.1 Perspective

Experimental investigations over the past decade have demonstrated that entrainment and mixing in fully turbulent shear layers are dominated by organization that results from the dynamics of large scale vortical motions. These large scale motions have been shown to transport unmixed fluid, from both free streams, across the entire extent of the layer (Konrad 1976, Breidenthal 1978, Koochesfahani 1984). Furthermore, as a consequence of these motions, the probability of finding molecularly mixed fluid within a given range of compositions is essentially uniform across the entire layer (Fiedler 1974, Konrad 1976, Koochesfahani 1984). On the basis of these results and many others, it is now generally recognized that models of entrainment and mixing in turbulent shear layers probably need to incorporate features of these large scale motions.

Such large scale organization of entrainment and mixing may also be present in other free turbulent shear flows, including the axisymmetric turbulent jet. The existence of orderly vortical structure in the near field of turbulent jets has been recognized for some time (e.g., Bradshaw, Ferriss & Johnson 1964; Mollo-Christensen 1967; Becker & Massaro 1968; Crow & Champagne 1971; Yule 1978). The prevailing view, however, is that this near field structure does not survive in any organized form beyond the first few jet diameters. Entrainment and mixing in the far field of turbulent jets is classically viewed as a stochastic process, involving transport by eddies whose scale is small relative to the overall lateral extent of the flow and which characteristically lack any persistent large scale organization. This picture has arisen primarily from point measurements and flow visualizations which are unable to reveal features of transport and mixing within the jet.

If this picture of entrainment and mixing in the jet far field is correct, then at any point in the flow the resulting turbulent fluxes of mass, momentum, energy and scalars would be proportional to the local gradients in their mean profiles. Virtually all models that attempt to predict entrainment and mixing in turbulent jets, as well as in shear layers and other flows, currently use such a "gradient transport" basis for the turbulent fluxes. However, since these models attempt to work from the mean profiles, they inherently cannot distinguish between molecularly mixed fluid at a given composition and an average over mixed and unmixed fluids yielding the same composition in the mean. In this context the distinction between turbulent transport and molecular mixing is lost in such models.

As an example, one class of such models attempts to compute probability density functions (PDFs) of passive or reactive scalars for turbulent reacting flows (e.g., Pope 1980, Kollmann & Janicka 1982, Pope 1985). The resulting computed PDFs for mixing of a passive scalar in the turbulent shear layer, however, differ fundamentally from PDFs measured in that flow (Koochesfahani 1984). A second difficulty with such models for turbulent mixing is that the role of molecular diffusivity in mixing, characterized by the Schmidt number ($Sc = \nu/D$), is disregarded at large Reynolds number. Recent measurements in the shear layer show, however, that the amount of molecular mixing in gas and liquid layers differs roughly by a factor of two (Koochesfahani 1984). A comparison by Walker (1979) of the predictions from a wide range of classical turbulent mixing models with measurements obtained in shear layers and jets concludes that such models are not capable of accurately predicting mixing.

The results of several recent investigations have suggested that this classical picture of jet entrainment and mixing as resulting from transport by stochastic small scale eddies, on which these models are based, may not be correct, and that transport by large scale motions displaying a characteristic organization may play an important role in transport and mixing in the jet. Tso, Kovasznay & Hussain (1981) have attempted to show the existence of such large scale organization in the jet by means of conventional time-averaged space and time correlations based on point measurements of velocity. Dimotakis, Miake-Lye & Papantoniou (1983a) have shown direct evidence for large scale transport of unmixed ambient fluid into the jet from planar laser induced fluorescence visualizations of jet mixing. Dimotakis, Broadwell & Howard (1983b) have shown further visualizations of mixing which suggest that the jet fluid concentration within large regions in the jet is nearly constant.

1.2 Present Experiments

The present experiments were undertaken to investigate further the possible existence of a large scale organization of entrainment and mixing in the turbulent jet similar to that which has been found in the turbulent shear layer. Furthermore, as was noted above, measurements obtained in gas and liquid shear layers have established a Schmidt number dependence in the amount of molecular mixing in that flow. Little is known about the role of Schmidt number in jet mixing. To date, virtually all investigations of mixing in jets have been conducted in gases ($Sc \approx 1$). The present experiments, conducted in water ($Sc \approx 600$), are intended to provide a baseline to which future investigations can be compared to determine the role of Schmidt number for mixing in such jets.

These experiments investigate entrainment, mixing and chemical reactions in steady, axisymmetric, momentum-driven turbulent jets issuing into an unconfined, quiescent medium for the large Schmidt number (liquid-phase) regime. The experiments presented cover the axial range from the jet exit to 300 momentum diameters downstream, and span the range of Reynolds numbers from 1,000 to 20,000. Laser induced fluorescence (LIF) techniques are used to visualize entrainment and mixing in such jets, as well as to obtain direct, non-intrusive, high-resolution measurements of the jet fluid concentration field.

The visualization experiments in this investigation photograph the laser induced fluorescence from single or dual orthogonal laser sheets in non-reacting and chemically reacting jets. The technique for such planar LIF visualizations of non-reacting jets is similar to that used in earlier visualizations of mixing in turbulent flows by Dewey (1976), Lui et al (1977), Bernal (1981), Dimotakis & Papantoniou (1981) and Dimotakis et al (1983a,b). The chemically sensitive LIF techniques employed here to determine the extent of molecular mixing in turbulent jets are also similar to those used by Dimotakis et al (1983b).

The concentration measurements in this investigation image the LIF intensity directly onto a linear photodetector array to obtain quantitative information along a line in the jet concentration field. Robben et al (1976), Dewey (1976) and Lui et al (1977) have made non-intrusive point measurements of the LIF intensity with a single photodetector. Dimotakis et al (1983a) obtained line measurements, as opposed to point measurements, of the LIF intensity in the form of x-t diagrams by imaging the fluorescence onto a 1024-element linear, self-scanning photodiode array, the output of which was used to modulate an oscilloscope beam driven synchronously in a raster scan fashion. Koochesfahani (1984) and Koochesfahani & Dimotakis (1984) extended this technique to obtain direct quantitative information of the concentration along a line in a plane turbulent shear layer by digitally acquiring the photodiode array output through a high-speed computer data acquisition system. In these experiments, essentially the same linear photodiode array imaging technique is adapted to the jet to obtain instantaneous profile measurements of concentration along the axial and radial directions in the jet far field.

CHAPTER 2

EXPERIMENTAL FACILITY

2.1 Flow Facility

These experiments were entirely carried out in the water facility shown in figures 2-1 and 2-2. This facility was designed by G. L. Brown and P. E. Dimotakis (see Dimotakis et al 1983a) and was constructed, in part, by Mr. D. Papantoniou.

The facility consists of a stainless steel tank having 33½ × 33½ × 62½ inch interior dimensions, with 1 inch thick, 31 × 31 inch glass windows on four sides, and a 1 inch thick, 10 inch diameter glass window centered on the bottom face. Drainage is provided by four 6 inch diameter holes, also located on this bottom face, leading to a pair of 6¼ inch diameter PVC pipes with pneumatically driven variable-angle butterfly valves (RCS Model PA-100) actuated from a solenoid valve. The drain pipes lead to a large PVC holding tank, which is emptied by a 1/2 hp drain pump (F&W Model 92J105). The variable-angle butterfly valves also allow a controlled gravity-driven co-flow to be established in the tank. No such co-flow, however, was used in the experiments reported here.

The stainless steel tank can be filled either from an ordinary tap water line or from a softened filtered water line, which join into one of the PVC drain pipes. Acid or base can be mixed with the water in the tank by means of circulating pumps.

The jet was discharged by driving a plenum containing the jet fluid with an air supply system metered through a micrometer-controlled variable-throat sonic orifice, with a constant upstream pressure. A high pressure air line, regulated to 60 psi, led to a 550 cubic inch ballast tank, which served as the upstream reservoir for the micrometer-controlled metering valve (Whitey Model SS 22RS4) held at sonic conditions. The metering valve, in turn, led to the jet plenum. A solenoid valve in line between the ballast tank and the metering valve was opened to initiate the flow.

This pressure-driven discharge system has been documented previously (Dimotakis et al 1983a). Its principal advantage is that, for a constant upstream reservoir pressure, the mass flux of air driving the plenum fluid is constant by virtue of the fact that the metering valve is held at sonic conditions, regardless of any perturbations in the pressure at the jet exit. Any such impulsively started pressure-driven jet can, however, exhibit an oscillatory component in its exit velocity during the starting transient when the natural resonance of the second-order (spring-mass-damper) system formed by the volume above the free surface and the mass of jet fluid in the plenum is excited by the impulsive pressure rise (Dimotakis & Papantoniou 1981). After the starting transient, this resonance can in principle be re-excited, depending on the spectral content of the pressure driving the jet fluid. The plenum configuration used in the present experiments had a very short time constant for decay of the starting transient, after which the sonic orifice held the plenum pressure very nearly constant. As a result, no indications of such resonance-driven oscillations were observed in the present experiments.

An important consideration in such non-co-flowing jet mixing experiments is the recirculation and re-entrainment of jet fluid that must occur as the jet impinges on the bottom of the tank. In these experiments, the farthest downstream measurement location was sufficiently far from the bottom of the tank that, during the duration of the experiment, no such self-contamination of the flow occurred. A related consideration is the weak counterflow that must be induced in the ambient fluid by the displacement effect of the jet as it impinges on the bottom of the tank. For the dimensions of the present facility, it can be shown that the velocity of this induced counterflow does not exceed 2.5% of the mean centerline velocity at the farthest downstream measurement location.

2.2 Jet Plenum and Nozzle

The jet plenum and nozzle used in these experiments are shown in figure 2-3. The plenum consisted of a Lucite cylinder, 8 inches long, with a 3¾ inch internal diameter, having flanged ends sealed with an O-ring to accept the nozzle and end plates. The nozzle plate was a ½ inch thick Lucite disc with a smooth axisymmetric faired inlet, leading to a ¾ inch long axisymmetric nozzle with a ⅒ inch interior diameter, d_o. The exterior of the nozzle was tapered to give a thin lip at the exit. The nozzle had a length-to-diameter ratio of only 8-to-1 and was designed to give a nearly uniform exit velocity profile. The end plate also consisted of a ½ inch thick Lucite disc, with a connection to accept the air supply line from the metering valve and with a fill hole sealed with a neoprene stopper. In order to eliminate any swirl component in the jet velocity that could result from a slight component of swirl in the plenum, a cruxiform insert was fitted into the plenum. The plenum was mounted above the facility in a steel split-collar so that the nozzle protruded below the free surface in the tank.

The jet exit velocity, u_o, at any metering valve setting was determined directly from the jet mass flux. Exit velocities up to 8 m/sec were utilized. Reynolds numbers based on

$$Re = \frac{u_o d_o}{\nu} \tag{2.1}$$

as high as 20,000 were used in the experiments reported here.

The concentration of the water-soluble laser fluorescent dye used in these experiments was in all cases sufficiently weak for its effect on the jet fluid density to be neglected. As a result, for the experiments involving the passive LIF technique in Section 3.1 and Chapters 4 and 5 , the densities of the jet and ambient fluids could be matched by matching the jet and ambient fluid temperatures. For the experiments using the chemically sensitive LIF technique in Section 3.2 , the densities of the jet fluid (base) and ambient fluid (acid) were not precisely matched, however in no case did $(\rho_o - \rho_\infty)/\rho_\infty$ exceed 0.017 . For the chemical reaction method in Section 4.9 , the densities of the jet and ambient fluids were matched by dissolving salt (Na_2SO_4) in the ambient fluid.

CHAPTER 3

VISUALIZATION OF MIXING IN JETS

The present investigation is concerned with steady, unconfined, momentum-driven, turbulent jets issuing into a quiescent environment. Mixing in such jets has classically been visualized by a variety of techniques. One popular method is to mark the jet fluid with a tracer, such as smoke or dye, as is the case in figure 3-1 . This photograph shows the jet formed in the facility described in Chapter 2 by injecting a strong concentration of dye into water, in this case with diffuse illumination. Such tracer-based visualization methods, however, allow only an external view of the jet. They do not permit visualization of mixing within the jet. Other methods, such as shadowgraph and schlieren visualization, circumvent this limitation by using optical refraction techniques in transparent media. The integrating nature of these methods, however, produces an image from which it is difficult to interpret local features of mixing within the jet.

3.1 Visualization by the Passive LIF Technique

In recent years, laser induced fluorescence (LIF) techniques have been used to avoid these particular limitations in visualizing entrainment and mixing in turbulent shear layers and jets (Bernal 1981; Dimotakis, Miake-Lye & Papantoniou 1983a; Dimotakis, Broadwell & Howard 1983b; Koochesfahani 1984; Dahm, Dimotakis & Broadwell 1984; Dahm & Dimotakis 1985).

Briefly, for the planar LIF technique in the jet, a laser fluorescent dye (disodium fluorescein) was homogeneously mixed in a weak concentration with the jet fluid (water) and injected through the jet nozzle into the ambient fluid (water). The dye fluoresces efficiently when excited by the 514.5 nm line from an argon ion laser (Coherent Radiation CR-3 or CR-10). Through an appropriate combination of optical elements, the laser illumination was arranged to form either a single thin sheet containing the jet axis (see figure 3-2) or a pair of mutually orthogonal sheets, both containing the axis (see figure 3-3). The laser sheet(s) could be made as thin as a few hundred microns over the region of observation. Dye-containing fluid in the plane of the laser sheet(s) then fluoresced with an intensity proportional, in part, to the local concentration of jet fluid.

Figures 3-4a, 3-4b and 3-4c show the mixing in a thin slice through a turbulent jet at Reynolds numbers ranging from 1,500 to 20,000 , visualized over the first 350 jet exit diameters using the single-sheet planar LIF technique. At the lowest Reynolds number, the sheet is sufficiently thin to resolve even the smallest scales of turbulent transport near the bottom of the field of view. There are several features of particular interest in such visualizations of mixing in jets.

First, as the photographs in figure 3-4 show, <u>unmixed</u> ambient fluid is transported deep into the jet. This has been observed in previous visualization experiments using the LIF technique (Dimotakis et al 1983a). Conventional visualizations of transport and mixing in jets such as figure 3-1, as well as shadowgraph and schlieren visualizations, are not capable of directly indicating the presence of unmixed ambient fluid within the jet and, in fact, are generally interpreted as suggesting precisely the opposite. This interpretation has, in part, contributed to the classical notion that entrainment and subsequent transport of ambient fluid in the jet far field may be modeled as a gradient diffusion process, resulting from stochastic small scale eddies which are incapable of bringing unmixed ambient fluid far into the jet. Photographs such as those in figure 3-4, however, suggest a different mechanism, namely, that large scale eddies, capable of transporting unmixed ambient fluid to points deep within the jet, play an important role in the entrainment process. This observation was first made by Dimotakis et al (1983a), who noted that the resulting picture of jet entrainment differs fundamentally from the classical view. The specific issue of how much unmixed ambient fluid is present at various points along the jet radius in the far field is addressed quantitatively in Sections 4.8 and 5.4 .

Second, as has also been noted previously (Dimotakis et al 1983a,b), such visualizations of jet mixing suggest that the jet fluid concentration of the *mixed* fluid, hereafter meaning *molecularly* mixed fluid, is approximately constant in relatively large regions in the jet. Abrupt concentration "fronts" can be discerned in the photographs in figure 3-4, particularly at the higher Reynolds numbers, separating large regions within which the jet fluid concentration of the mixed fluid appears to be nearly uniform. As a result, while in the *mean* the concentration of jet fluid along the axial direction, x, must decrease uniformly like x^{-1} (see Appendix A), at any instant the concentration would be expected to decrease in a series of discrete steps. Similarly, while the concentration along the lateral direction must follow the well-known bell-shaped form in the *mean*, at any instant relatively little lateral gradient would be expected in the mixed fluid composition within one such large region. As a result, owing to the inability to distinguish between turbulent transport and molecular mixing in the mean (as was noted in Section 1.1), the mean profiles give a poor representation of the mixed fluid compositions within the jet. This picture of the instantaneous mixed fluid compositions within the jet also differs fundamentally from the classical view of jet mixing.

Third, the photographs in figure 3-4, together with motion picture data of jets visualized by this technique, suggest that unmixed ambient fluid is entrained into the jet and is carried into these large regions primarily from the rear of each region as the result of large scale rotational motions near the jet edges.

As an aside, a comparison between figures 3-4a and 3-4b shows that, at the lower Reynolds number, there is a laminar or transitional region immediately beyond the jet exit that does not exhibit the linear growth characteristic of the turbulent jet. The axial distance required for the onset of this linear growth, commonly referred to as the breakpoint length of the jet, s, is shown as a function of Reynolds number in figure 3-5 . Although for jets issuing from long tube nozzles this Reynolds number dependence of the breakpoint length may be related to a transition in the resulting pipe flow upstream of the jet exit, the present nozzle (see Section 2.2) has no such pipe flow, indicating that the breakpoint occurs from a natural instability of the shear flow downstream of the nozzle exit.

3.2 The Chemically Sensitive LIF Technique

Weddell (in Hottel 1953) first used an aqueous acid-base neutralization reaction in conjunction with a pH-sensitive dye (phenolphthalein) to monitor mixing at the molecular scale in the jet. In the present investigation, a similar acid-base neutralization reaction, exploiting the pH-sensitive characteristics of the laser fluorescent dye (see Appendix B), is used to measure the extent of molecular mixing in the jet.

In this case, the laser fluorescent dye was mixed with an aqueous base solution (NaOH) and injected through the nozzle into the ambient fluid, in this case an aqueous acid solution (H_2SO_4). The resulting acid-base reaction between the jet and ambient fluids was essentially isothermal. Owing to the pH-sensitivity of the dye, the relative intensity of fluorescence from dye-containing fluid in the plane of the laser sheet(s) varied with the pH of its local chemical environment at the molecular scale (see figure B-3). By selecting the acid and base solutions to be sufficiently strong, the span of pH over which the dye undergoes its fluorescence transition was crossed in a very narrow range of mixture ratio, as shown in figure 3-6 . The mixture ratio, μ, is defined here as the local mass ratio of ambient fluid (acid) to jet fluid (base) in an infinitesimal volume of (molecularly) mixed fluid. The resulting relative fluorescence intensity from mixed fluid as a function of its mixture ratio is shown in figure 3-7 . Note that the relative fluorescence intensity was constant up to a particular value of the mixture ratio, beyond which the dye was rendered essentially non-fluorescent. This particular mixture ratio is referred to here as the stoichiometric mixture ratio, ϕ, for the chemical reaction and could be set by selecting the relative strengths of the acid and base solutions.

Since the fluorescence transition for the dye was reversible and occurred on a very short (nanosecond) time scale, the dye fluorescence could be used to determine if the instantaneous local extent of molecular mixing between the jet and ambient fluids in the plane of the laser sheet(s) exceeded the selected stoichiometric mixture ratio ϕ. A photograph of a jet visualized with this chemically sensitive LIF technique is shown in figure 3-8 . Note that this photograph is intentionally over-exposed to allow the farthest downstream location of fluorescing fluid to be identified more easily.

3.3 Time-Averaged Characteristics of Mixing

An aspect of mixing in the jet that can be inferred directly from photographs such as figure 3-8 is the axial distance from the breakpoint of the jet required to mix every part of jet fluid with ambient fluid, on a molecular scale, to at least the stoichiometric mixture ratio ϕ, corresponding to the farthest axial location at which fluorescing fluid can be found (Broadwell 1982). The axial distance between the "flame" tip, L, and the breakpoint of the jet, s, is referred to here as the turbulent "flame" length (although a more appropriate term might be turbulent "reaction" length). The arguments in Appendix A suggest that the axial length scale which properly normalizes the concentration field of all momentum-driven turbulent jets is the jet "momentum diameter", d^*, giving the dimensionless axial coordinate as $\chi = x/d^*$ and giving the dimensionless turbulent flame length as $(L-s)/d^*$. Broadwell (1982) first recognized that the variation of this dimensionless turbulent flame length with the stoichiometric mixture ratio ϕ can be related to the rate of molecular mixing in the jet. In fact, it can be shown that this variation gives a lower bound for the molecular mixing rate.

The rate of molecular mixing was determined in this manner at Reynolds numbers ranging from 1,000 to 20,000 and for stoichiometric mixture ratios from 3.7 to 20. The ensemble-averaged mean flame length data at each condition are shown in figure 3-9, together with the earlier measurements by Weddell (in Hottel 1953) using a similar technique. As can be seen in this figure, for all values of ϕ, the mean flame lengths become independent of Reynolds number beyond a sufficiently large Reynolds number. The data in figure 3-9 are shown in figure 3-10 normalized by the Reynolds number-independent mean flame length at large Reynolds number for each value of ϕ.

Figures 3-9 and 3-10 show that increasing as well as decreasing mean turbulent flame lengths were observed with increasing Reynolds number, depending on the value of ϕ. For small values of ϕ, the decreasing flame lengths are consistent with the earlier results of Weddell. The increasing flame lengths for large ϕ, however, appear to be a new observation. However, as Broadwell (private communication) has pointed out, it may be worth cautioning that the densities of the acid and base reactants used in these experiments were not precisely equal, with the density difference being greatest for the larger values of ϕ (but with $(\rho_0 - \rho_\infty)/\rho_\infty$ in no case exceeding 0.017). Since the Reynolds number was varied through the jet momentum flux, any resulting buoyancy effects would be greatest at the lower Reynolds numbers and for the larger values of ϕ. The increasing flame lengths with increasing Reynolds number for the larger values of ϕ may be consistent with the increasing flame lengths observed for increasing ratios of momentum flux to buoyancy flux in partially buoyant turbulent jets (e.g., Zukoski et al 1984).

The data in figure 3-10 also show that, for all values of ϕ, at Reynolds numbers above 3,000 and as high as 20,000, no further change in the mean flame length was discernible. In terms of the jet fluid concentration field, this implies that the highest concentrations at any point in the jet far field do not change with Reynolds number beyond $Re \approx 3{,}000$. While this suggests that the molecular mixing rate has become independent of Reynolds number at $Re \approx 3{,}000$, it cannot be directly concluded that all time-averaged characteristics of mixing in the jet have become independent of Reynolds number. In fact, measurements by Ricou & Spalding (1961) suggest that the jet entrainment rate may not become independent of Reynolds number until $Re \approx 25{,}000$. This may, perhaps, be best viewed in the context of the local concentration probability density functions (PDFs), which describe the complete time-averaged statistics of the concentration field. From figure 3-10, for $Re > 3{,}000$ we are assured that the highest concentrations in the PDFs become independent of Reynolds number. We cannot, however, make any a priori statement about the remainder of the PDF. The dependence of the PDF on Reynolds number is discussed in Sections 4.8 and 4.9.

For $Re \geq 3{,}000$, the Reynolds number independent mean turbulent flame lengths are observed to increase in direct proportion with ϕ, as shown in figure 3-11, following the scaling law

$$\frac{L}{d^*} \approx 10\,\phi \,, \qquad (3.1)$$

confirming the earlier measurements of Weddell. In the context of jet mixing, equation (3.1) states that the extent of molecular mixing in the jet far field is directly proportional to the dimensionless axial distance, implying that the rate of molecular mixing is constant in the jet far field (Broadwell 1982).

If the jet momentum diameter, d^*, is the appropriate length scale normalizing the axial coordinate in the far field of all momentum-driven turbulent jets at large Reynolds number, then the rate of molecular mixing in all such jets should follow the same scaling law with ϕ, regardless of the details of their velocity and density profiles at the jet source or of the absolute densities and mass diffusivities of the jet and ambient fluids. Indeed, as shown in figure 3-12, when normalized by d^*, the mean flame lengths of momentum-driven exothermic gas-phase turbulent jet flames (Wohl et al 1948, Hawthorne et al 1948, Brown 1971, Becker et al 1978a,b) as well as isothermal and exothermic vapor-into-liquid condensing reacting turbulent jets (Kerney et al 1972, Weimer et al 1973, Avery & Faeth 1974) follow the same scaling for flame length with their reaction stoichiometric mixture ratio as do the present isothermal liquid-phase jets. Such a correlation with d^* over the wide range of density ratios in figure 3-12 was first noted by Avery & Faeth (1974).

Broadwell (1982) and Tyson, Kau & Broadwell (1982) use a form similar to figure 3-12 to argue that, for entrainment-limited mixing, the rate of molecular mixing is set by the entrainment rate of the jet. The jet entrainment rate has been measured by Ricou & Spalding (1961) (see equation (A.3)) and is shown together with the scaling law for molecular mixing from equation (3.1) in figure 3-13. Note that, for any value of μ in this figure, at an axial location $\chi_e(\mu)$ the jet has already entrained a sufficient amount of ambient fluid to, in principle, bring every part of jet fluid to the mixture ratio μ, but that such mixing on the molecular scale is not actually completed until the axial location $\chi_m(\mu)$, where

$$\chi_m(\mu) \approx 3 \cdot \chi_e(\mu) . \tag{3.2}$$

From the slopes of the lines in figure 3-13, the lower bound for the molecular mixing rate in the jet far field is seen to be at least one-third of the jet entrainment rate.

3.4 Time-Dependent Characteristics of Mixing

In Section 3.3, data were presented for the mean flame lengths of reacting jets, corresponding to the time-averaged characteristics of mixing in the far field of turbulent jets. Mixing in such jets, however, displays inherently time-dependent characteristics.

3.4.1 The flame length fluctuations

The time-dependent character of jet mixing is demonstrated in the sequence of photographs in figure 3-14. This sequence shows every fifth frame of an excerpt from a motion film of a turbulent jet visualized in the plane of a single laser sheet with the chemically sensitive LIF technique at $Re = 10,000$ and $\phi = 15$. As figure 3-14 indicates, these "flames" exhibit roughly periodic fluctuations in length about their mean value. A similar sequence, shown in figure 3-15, from a visualization using the dual-orthogonal laser sheet technique confirms that these flame length fluctuations occur simultaneously in orthogonal planes. In this sequence, the fluorescence from mixed fluid intersected by each of a pair of mutually orthogonal laser sheets is imaged, without perspective distortion, by a system of mirrors onto the film plane to produce two simultaneous views of mixing in the jet (see also Dimotakis & Papantoniou 1981). Such roughly periodic flame length fluctuations were observed for all values of ϕ and at all Reynolds numbers.

It is instructive to sight down the time axis in figures 3-14 and 3-15 to observe the reaction process at the flame tip. In the context of the time-varying concentration field of the jet, these fluctuations are indicative of a roughly periodic large scale organization of entrainment and mixing in the jet far field. Specifically, at the beginning of the sequence in figure 3-14, for example, mixed fluid in a large region near the flame tip fluoresces, implying that its composition has not yet exceeded the stoichiometric mixture ratio ϕ. A relatively short time later, as evidenced by the fact that this region has progressed downstream only about one local jet diameter, all of this mixed fluid has been rendered non-fluorescent, implying that its composition throughout this large region has crossed over the stoichiometric mixture ratio ϕ. The fact that this process repeats roughly periodically for all values of ϕ (i.e., at all axial locations) suggests a roughly periodic large scale organization in the instantaneous concentration field of the jet.

These flame length fluctuations are consistent with the observation of large regions of essentially uniform mixed fluid composition noted in Section 3.1 and by Dimotakis et al (1983a,b). Additionally, the observation that within such a large region the last point to reach the stoichiometric mixture ratio is typically near the farthest downstream edge of the large region is an indication that there may be a slight decrease in the mixed fluid composition from the "front" to the "rear" of these regions. This is consistent with the observation in Section 3.1 that unmixed ambient fluid is entrained and brought into these regions primarily from the rear.

3.4.2 Fluctuation scaling laws

By virtue of the fact that these large regions of approximately uniform mixed fluid composition are, in the case of a chemically reacting jet, responsible for the flame length fluctuations, scaling laws for these flame length fluctuations can be used to determine the scaling of these regions. The maximum and minimum flame lengths for the data at each value of ϕ in figure 3-11 are shown in figure 3-16. These data suggest that the flame length fluctuations scale with ϕ as

$$\Delta\left(\frac{L}{d^*}\right) \approx 4\phi . \tag{3.3}$$

Using the mean flame length scaling law in equation (3.1) and the relation for the local jet visual diameter $\delta(x)$, namely,

$$\delta(x) \approx 0.4\, x , \tag{3.4}$$

indicates that, for all flame lengths, the magnitude of the flame length fluctuation is approximately equal to the local jet diameter at the mean flame tip, namely,

$$\Delta L \approx \delta(L) , \tag{3.5}$$

as reported recently (Dahm et al 1984). Equation (3.5) indicates that the flame length fluctuations occur on the largest local length scale of the flow.

The temporal scaling of these fluctuations was determined by measuring the instantaneous turbulent flame length directly from over 2400 individually projected film frames of a motion film of a turbulent jet at $Re = 10{,}000$ and $\phi = 15$, visualized with the chemically sensitive LIF technique. The resulting time-varying flame length data, spanning roughly 50 periods of the flame fluctuation, are shown in figure 3-17. Defining fluctuation events delimited by tic marks in this figure allowed a length and time scale to be determined for each fluctuation. Histograms of the resulting fluctuation length and time scales, normalized by δ, the local jet visual diameter, and τ_M, the local large scale time of the flow, where

$$\tau_M = \frac{\delta}{u} \tag{3.6}$$

with u the local centerline mean axial velocity, are shown in figure 3-18. The degree to which these flame length fluctuations can be termed periodic is demonstrated by the lower histogram in this figure. These histograms indicate that both the length and time scales of the flame length fluctuations are approximately equal to the corresponding local characteristic large scales of the flow.

3.5 Implications for organized mixing

The visualizations of jet entrainment and of mixing described in Section 3.1, together with the observed flame length fluctuations in Section 3.4.1 and the scaling laws for these fluctuations in Section 3.4.2, suggest the idealized conceptual picture for organized entrainment and mixing in the jet far field shown in figure 3-19 and described below. Elements of this picture have been described by Dimotakis et al (1983a,b).

Figure 3-19 shows the instantaneous concentration field of the jet as consisting of large regions with an axial and radial extent approximately equal to the largest local scale of the flow. Within each region, the composition of mixed fluid is approximately uniform, decreasing slightly from front to rear. Each region also contains unmixed ambient fluid at all scales of the local turbulent cascade, with entrainment primarily the result of transport at large scales capable of bringing unmixed ambient fluid deep into the jet, and occurring principally from the rear of each region. The jet fluid concentration of the mixed fluid within each region decreases with time as the result of mixing with the entrained ambient fluid as the region evolves, giving rise to the flame length fluctuations in the case of a chemically reacting jet.

An important aspect of figure 3-19 is that, while the conventional axial and radial forms of the mean concentration field of the jet are preserved in a time-averaged picture, the instantaneous concentration field does not resemble the time-averaged picture. In fact, the mean concentration field of the jet gives a misleading picture of the mixed fluid compositions within the jet and of the mechanisms responsible for entrainment and mixing. The differences between this instantaneous picture and the conventional time-averaged picture may have particularly important implications for the modeling and prediction of chemical reactions between the jet and ambient fluids.

In Chapters 4 and 5, specific elements of the conceptual picture in figure 3-19 of organized entrainment and mixing in the jet far field are evaluated from direct quantitative measurements of the jet concentration field.

CHAPTER 4

AXIAL CONCENTRATION MEASUREMENTS

Individual axial profiles of jet fluid concentration in a non-reacting jet were measured using an LIF passive scalar technique in conjunction with linear photodiode array imaging and high speed digital data acquisition. The technique was similar to earlier line measurements of concentration in the plane shear layer (Koochesfahani 1984).

4.1 The Axial Measurement Technique

The laser fluorescent dye was again premixed with the jet fluid (water) and discharged into the ambient fluid (water). This was a "dilution experiment" in the sense that no chemical reaction was involved. For these quantitative experiments, to eliminate the possible effects of pH variations in the water on the dye fluorescence characteristics, filtered softened water brought to $pH \approx 9$ by the addition of a small amount of NaOH was used for both the jet and ambient fluids.

The beam (514.5 nm) from an argon ion laser (Coherent Radiation CR-3 or CR-10) was collimated and oriented coincident with and propagating up the jet axis. The laser induced fluorescence from dye along the beam was imaged onto a 1024-element Reticon self-scanning linear photodiode array (see Appendix D.1). An orange filter (Hoya No. 15) effectively eliminated directly scattered laser light at

514.5 nm from any particulates in the flow. The imaging configuration is shown schematically in figure 4-1 .

The imaged portion of the jet axis spanned the axial range $0 \leq \chi \leq 300$, where χ is the dimensionless axial coordinate x/d^*, with d^* the jet momentum diameter (see Appendix A). Successive individual profiles of fluorescence intensity along the jet axis were measured at $Re = 1{,}500$ and $Re = 5{,}000$, on either side of the $Re = 3{,}000$ limit at which the molecular mixing rate becomes independent of Reynolds number (see Section 3.3), as well as at $Re = 20{,}000$.

Each of the 1024 photodiode array elements (pixels) had a sensitive detector aperture of $25\mu m \times 26\mu m$. The optics used produced an image ratio of 30 : 1, and the beam diameter varied from roughly 0.5 mm to about 1 mm, defining the volume imaged onto each photodiode array element. At any axial location, the smallest scale of turbulent transport, λ_ν, could be estimated by assuming that Kolmogorov scaling applied at these Reynolds numbers. Taking the scaling constant to be of order 1 gives

$$\lambda_\nu/\delta \approx Re^{-3/4} \tag{4.1}$$

and gave the estimates in Table 1 for the Kolmogorov scale. Based on these estimates, the spatial resolution of these measurements was sufficient to resolve the Kolmogorov scale for $\chi \geq 250$ at $Re = 1{,}500$. At none of these Reynolds numbers could the strain-limited molecular diffusion layer thickness (the Batchelor scale, see Batchelor 1952) be resolved, which is of the order $\lambda_\nu \cdot Sc^{-1/2}$. In these experiments, with $Sc \approx 600$, the Batchelor scale was estimated to be approximately 25 times smaller than the estimates for the Kolmogorov scale in Table 1.

χ Re	100	200	300
1,500	0.41 mm	0.83 mm	1.24 mm
5,000	0.17 mm	0.34 mm	0.50 mm
20,000	0.06 mm	0.12 mm	0.18 mm

Table 1. Estimates of the Kolmogorov scale, λ_ν.

The 1024-element photodiode array was clocked at a pixel rate of 256 kHz, corresponding to a scan rate of 235 scans/sec (including a blanking period of 64 additional clock cycles per scan), giving a scan time of 4.3 msec. Using the estimates for λ_ν in Table 1 gave the estimates in Table 2 for the Kolmogorov passage time, λ_ν/u, with u the local mean axial velocity on the centerline, at various points along the axis.

χ Re	100	200	300
1,500	11.9 msec	47.6 msec	107.0 msec
5,000	1.5 msec	5.8 msec	13.0 msec
20,000	0.1 msec	0.5 msec	1.2 msec

Table 2. Estimates of the Kolmogorov passage time, λ_ν/u.

Based on these estimates, the temporal resolution of these measurements was sufficient to resolve the Kolmogorov passage time for $\chi \geqq 60$ at $Re = 1{,}500$, and for $\chi \geqq 180$ at $Re = 5{,}000$.

The array output was digitized through a single channel high-speed 8-bit A/D converter and recorded on a computer disk (see Appendix D.2). Since, for large axial distances, the scan time was fast relative to the local time scales in the flow, and in order to keep the amount of data collected manageable, only every 16th scan of the array was actually recorded on the disk at $Re = 1{,}500$, while every 6th scan was recorded at $Re = 5{,}000$ and every 4th scan at $Re = 20{,}000$. Each measurement at the two lower Reynolds numbers consisted of 4000 recorded scans of the array (in excess of 4 million individual measurements), while at $Re = 20{,}000$ a total of 1000 array scans were recorded during each measurement. In all cases, the data spanned approximately twelve local characteristic large scale flow times δ/u at $\chi = 300$, this limit being imposed by the duration of each experiment.

Such simultaneous measurements of concentration in the jet over this range of the dimensionless axial coordinate χ pose a significant dynamic range problem. Specifically, the mean jet fluid concentration profile over the range $0 \leqq \chi \leqq 300$ spans well over a decade in magnitude. Digitizing direct measurements of concentration to a resolution of 8 bits would permit distinguishing sufficiently many concentration levels very near the jet exit, where the concentrations are high, but for $\chi > 150$ the concentrations have decreased to the point where fewer than 7 digital levels could be distinguished. By digitizing measurements of the fluorescence intensity, however, this problem can be circumvented, since the fluorescence intensity depends on the product of the local dye concentration and the local beam intensity (see Appendix E.3). While the dye concentration in the mixed fluid along the jet axis decreases due to mixing, the intensity of the beam, propagating in the opposite direction, decreases due to absorption and fluorescence of energy by the dye. By appropriately choosing the concentration of dye in the pure jet fluid to be sufficiently strong, the attenuation along the beam could be arranged to very nearly offset the dilution of the dye, producing a fluorescence intensity profile along the axis that is nearly uniform in the mean, thereby offering essentially uniform digital resolution over the entire field of measurement.

A typical individual fluorescence intensity profile, measured at $Re = 5000$ using this technique, is shown in figure 4-2. Each such measured profile was subsequently converted to the corresponding profile of jet fluid concentration, $c(\chi,t)$, using the technique outlined in Appendix E.3. An exact line attenuation integral accounted for the effects of attenuation along the beam, with the pixel imaging the nozzle exit providing the reference condition, while a measured transfer function accounted for the effects of collection non-idealities in the optical system. The jet fluid concentration profile obtained from the fluorescence intensity profile in figure 4-2 using this technique is shown in figure 4-3.

4.2 Mean Axial Concentration Measurements

The mean jet fluid concentration profile, $\bar{c}(\chi)$, along the jet centerline determined by an ensemble average of the 4000 individually measured concentration profiles at $Re = 5{,}000$, is shown in figure 4-4. As demonstrated in Appendix A.4, self-similarity in the jet far field requires that the mean concentration profile along any ray in the jet ($r/x = \text{constant}$) follow a χ^{-1} scaling. The extent to which this scaling is satisfied by the mean profile in figure 4-4 can be determined by examining the corresponding $\chi \cdot \bar{c}(\chi)$ profile, shown in figure 4-5. No virtual origin was used in these data. The uniformity of the profile in figure 4-5 for sufficiently large χ, and continuing for the full extent of the measurement, is a strong verification of the similarity scaling demanded of the mean concentration profile.

Profiles of $\chi \cdot \bar{c}(\chi)$ obtained from other experiments over the range $0 \leqq \chi \leqq 100$ are shown together with the present measurements in figure 4-6. The numerical value for the mean concentration scaling coefficient in the jet far field obtained from these measurements, namely,

$$\chi \cdot \bar{c}(\chi) \approx 5.4 \pm 0.14 , \tag{4.2}$$

compares well with the other experiments. Furthermore, this scaling coefficient compares well with the value of 5.7 obtained in Appendix A. The $\chi \cdot \bar{c}(\chi)$ profile thus serves to validate this technique for measuring individual concentration profiles along the jet axis.

The rms concentration fluctuation intensity profile along the jet axis, $(c')_{rms} = (\overline{c'^2})^{1/2}$, determined from these measurements at

$Re = 5{,}000$ is shown in figure 4-7 together with the profiles reported from other experiments. Although for small χ the present measurements cannot accurately resolve concentration fluctuations, the profiles in figure 4-7 agree well.

It is generally assumed that, at a sufficiently large axial distance, these concentration fluctuation intensities will reach a constant level. In fact, as seen in figure 4-7, few measurements actually report attaining such a constant level, it generally being assumed that the measurements did not extend sufficiently far downstream. This has been taken to be an indication of "the long memory of turbulence" (Lockwood & Moneib 1980). It is noteworthy, however, that for the present experiments, extending to axial distances as large as $\chi = 300$, the measured concentration fluctuation intensities still have not reached a constant state. (It should be noted that the temperatures of the jet and ambient fluids were matched to within 0.5 ^{o}C to ensure that buoyancy effects were negligible). In light of the large range of χ spanned by these measurements, it is likely that these fluctuation intensities will not attain a constant level at any axial distance, suggesting that the conventionally assumed form of the fluctuation similarity may not be correct. This issue is addressed further in Section 4.5 .

4.3 Measurements of Concentration Time Histories

Measurements of the jet fluid concentration versus time, at a fixed point on the axis ($\chi = 300$, $\eta = 0$), are shown in figure 4-8 for each Reynolds number.

Perhaps the most noteworthy feature of such concentration traces is that they do not show the distinct "ramp-like" features that have been observed in gas-phase (low Sc) jets. Such ramps are evident, for example, in figures 24b and 25 of Antonia et al (1975) and figure 18 of Chevray & Tutu (1978). It may be relevant to note that a similar observation has been made in plane mixing layers. Mungal (1983) reports traces of product concentration (temperature) in a gas-phase mixing layer which exhibit similar ramp-like features, while traces of product concentration in a liquid-phase mixing layer (Koochesfahani 1984) do not exhibit these ramps.

Also noteworthy in the concentration traces in figure 4-8 is the quantitative verification that unmixed ambient fluid is transported deep into the jet, as was noted in the planar visualization experiments in Section 3.1 . More unmixed fluid is detected at $Re = 1{,}500$ than at the two higher Reynolds numbers. It must be kept in mind, however, that the relative resolution in these measurements decreases with increasing Reynolds number, and that at least part of this difference may be attributable to this fact. This issue is addressed further in Sections 4.8 and 4.9 .

4.4 Axial PDFs of Concentration

While the profiles of mean concentration and rms concentration fluctuation intensity in Section 4.2 may be of specific interest in certain cases, the complete time-averaged statistics contained in these measurements can be derived at any point from the local concentration probability density function (PDF). Interest in the concentration PDF also arises from statistical approaches to the modeling and prediction of mixing and chemical reactions in turbulent shear flows (e.g., Pope 1980, Kollmann & Janicka 1982, Pope 1985).

PDFs of jet fluid concentration at several points along the jet axis over the range $0 \leq \chi \leq 300$, obtained from these measurements at $Re = 5{,}000$, are shown in figure 4-9. The χ^{-1} scaling of the mean concentrations along the jet axis can be obtained as the first moment of these PDFs. Similarly, the second moment of each PDF, indicative of its width, is related to the rms value of the local concentration fluctuations. In terms of these PDFs, the increasing concentration fluctuation intensities in figure 4-7 imply that, with increasing χ, the means of these PDFs decrease faster than do their widths.

4.5 The Similarity Concentration ψ

The right-hand edge of each of the PDFs in figure 4-9 corresponds to the highest concentration observed at that axial location. It can be argued that the axial location χ at which any particular concentration c is the highest value observed corresponds to the last axial location at which that concentration will be observed. The relation between this axial location and the particular concentration for $Re > 3{,}000$ can be inferred directly from equation (3.1) as

$$\frac{\chi}{\mu} \approx 10 \,, \tag{4.3}$$

where μ is the mixture ratio corresponding to the particular concentration c, related as

$$\mu = \frac{1-c}{c} . \tag{4.4}$$

This implies that an alternative concentration variable, ψ, can be defined as

$$\psi = \frac{\chi}{\mu} , \tag{4.5}$$

for which, by virtue of equation (4.3), the highest concentrations in PDFs of ψ will occur at $\psi \approx 10$ for all sufficiently large χ.

Furthermore, from the similarity scaling demanded of the mean concentration in equation (4.2), it can be argued that for large χ the first moment of PDFs of ψ will occur at $\psi \approx 5.4$. This suggests that, in terms of this alternative concentration ψ, the entire PDF may display self-similarity in the jet far field.

The conventional concentration PDFs in figure 4-9 are shown in terms of this proposed similarity concentration in figure 4-10 . These results indicate that, in terms of ψ, the concentration PDF does in fact become self-similar for sufficiently large values of χ. It should be kept in mind that the resolution in these measurements increases with χ and that at least part of the deviation from strict self-similarity for large χ may be attributable to this.

In light of the self-similarity demonstrated by PDFs of ψ, it might be hypothesized that PDFs of another variable, $(\chi \cdot c)$, might also exhibit self-similarity. The first moment of such PDFs would certainly be independent of χ, since from equation (4.4) at a fixed χ,

$$\begin{aligned}\overline{(\chi\cdot c)} &= \chi\cdot\overline{c} \\ &\approx 5.4 \; .\end{aligned} \qquad (4.6)$$

However, the widths of such PDFs, corresponding to $[(\chi\cdot c)']_{rms}$, are found not to become independent of χ. This is directly related to the observation in figure 4-7 that the conventional concentration fluctuation intensities do not become independent of χ. Specifically, at a fixed χ,

$$[(\chi\cdot c)']_{rms} = \chi\cdot(c')_{rms} \qquad (4.7)$$

$$= (\chi\cdot\overline{c})\;\frac{(c')_{rms}}{\overline{c}} \qquad (4.8)$$

$$\approx 5.4\;\frac{(c')_{rms}}{\overline{c}} \; . \qquad (4.9)$$

As a result, PDFs of $(\chi\cdot c)$ should not be expected to demonstrate self-similarity.

As was shown in figure 4-7, the conventional concentration fluctuation intensities do not reach a constant level for values of χ as large as 300. The self-similarity demonstrated in figure 4-10 by PDFs of the similarity concentration ψ, however, necessarily implies that the fluctuation intensities of ψ will become independent of χ and, in fact, will reach this constant level by $\chi \approx 20$ (see Section 4.6). Referring to the related discussion in Section 4.2, it must be concluded, therefore, that "the memory of turbulence" is considerably "shorter" than has previously been inferred from the conventional concentration fluctuation intensities, which it now appears inherently do not reach a constant level at any axial distance.

4.6 The Transition to Far Field Self-Similar Mixing

The self-similarity displayed by PDFs of ψ may be used to investigate the transition from mixing in the near field of the jet to the self-similar mixing that characterizes the jet far field.

PDFs of the conventional jet fluid concentration measured at $Re = 5{,}000$ on the jet axis over the range $0 \leqq \chi \leqq 40$ are shown in figure 4-11. It should be noted that, at small values of χ, these measurements lack the necessary spatial and temporal resolution to accurately resolve the concentration field. As would be expected for very small values of χ, the PDF just beyond the jet exit essentially consists of a delta function corresponding to pure (unmixed) jet fluid. With increasing χ, the PDFs eventually display the χ^{-1} scaling required of the mean concentration.

The PDFs in figure 4-11 are shown in terms of the similarity concentration ψ in figure 4-12. Note that pure jet fluid corresponds to $\psi \rightarrow \infty$. As would be expected, the PDFs do not display self-similarity for small values of χ. At sufficiently large axial distances, however, the PDFs display the self-similarity characteristic of far field jet mixing. Although the approach to this self-similar state is asymptotic, the PDFs in figure 4-12 suggest that the far field self-similar mixing state has, for all practical purposes, been attained by $\chi \approx 20$.

4.7 χ-t Diagrams of the Similarity Concentration

Although these measured axial concentration profiles can be displayed individually, as in figure 4-3, a means for simultaneously displaying these profiles which allows a direct interpretation of the time-varying jet concentration field is shown in figure 4-13. These are photographs of a 512×512 digital image display screen, on which the digitized similarity concentration ψ at every second pixel of the 1024 array elements was displayed for 500 successive individual concentration profiles. The 256 different grey levels were assigned to denote the various similarity concentration levels, with pure white corresponding to $\psi = 11$ and decreasing linearly to pure black for $\psi = 0$, namely, unmixed ambient fluid. These are, therefore, χ-t reconstructions of the jet concentration field, displayed in the similarity concentration ψ. It should be noted that each of these diagrams is composed of over a quarter of a million individual measurements of the jet fluid concentration. The technique for displaying these diagrams is similar to earlier displays of LIF data from the plane mixing layer (Koochesfahani 1984).

Note that unsteadiness in the breakpoint of the jet at low Reynolds numbers (see Section 3.1) gives a time-varying definition for $\chi = 0$. To avoid this complication for the data at $Re = 1{,}500$, $\chi = 0$ was taken slightly beyond the longest breakpoint observed. The absence of pure white at small values of χ in figure 4-13a is simply an artifact of this choice for $\chi = 0$.

The grey level histogram for any fixed χ in figure 4-13, related to the local PDF of the similarity concentration, will be the same for all values of $\chi \geqq 20$ owing to the self-similarity demonstrated by PDFs of ψ. Strictly speaking, since this self-similarity holds for $Re > 3{,}000$, this does not apply literally to figure 4-13a, but the use of this grey level assignment scheme in that case may also give a useful interpretation of the concentration field.

These data are shown with color assignments denoting the various ψ levels in figure 4-14. In this case, pure green denotes mixed fluid at the mean similarity concentration ($\psi \approx 5.4$), and tends uniformly toward blue to denote mixed fluid at similarity concentrations correspondingly below the mean value and, conversely, tends uniformly toward red to denote mixed fluid at similarity concentrations correspondingly above the mean value. Consequently, any blue shading denotes fluid at an unusually low concentration for its axial location, while red shading denotes fluid at an exceptionally high concentration its location. The principal feature of this color assignment is that, owing to the similarity demonstrated in the scaled concentration variable ψ, the physical interpretation of the colors in the same everywhere in the jet far field.

In figure 4-14a, large regions are discernible which can be seen to persist over relatively long durations and within which the similarity concentration of the mixed fluid displays a tendency toward red shades at the downstream edge and blue shades at the upstream edge. Such a repeating color pattern in the similarity concentration is consistent with the notion of large regions within which the jet fluid concentration in the mixed fluid is approximately uniform. The axial scaling of these regions increases roughly linearly with χ, while the temporal scaling increases roughly quadratically with χ. These regions increase in scale with χ and persist over relatively long times. Similar regions are discernible in figure 4-14b, although the resolution in this case is correspondingly lower. These large regions can be interpreted as a direct manifestation of the organized mixing in the jet far field described in Section 3.5. A composite χ-t diagram from contiguous data of the type displayed in figure 4-14 is shown, for both Reynolds numbers, in figure 4-15. Each of these diagrams displays over 2 million individual concentration measurements. This method of displaying the measured profiles allows the most direct interpretation of the time-varying concentration field in these data. Similar large regions, having the appropriate scaling in χ and t, can be discerned in these diagrams and support the picture of organized entrainment and mixing in figure 3-19.

The χ-t diagrams in figures 4-14a, 4-14b and 4-15, as well as earlier x-t diagrams by Dimotakis et al (1983a), give some indication of the dynamics of these large regions. In particular, there is evidence of upstream regions running into and coalescing with regions further downstream.

4.8 Unmixed Ambient Fluid on the Jet Axis

The time-varying probability of finding unmixed ambient fluid at a fixed point on the ray η, namely $p_0(\eta,t)$, was measured for $\eta = 0$ using a different axial imaging technique. For these measurements, the 1024-element photodiode array was positioned to image the fluorescence from a segment along the beam, again coincident with the jet axis, centered at $\chi = 300$ and extending from $285 \leq \chi \leq 315$ (roughly one-fifth the scale of the local jet diameter). All other aspects of the measurement technique were the same as before. In this case, however, it was not necessary to convert the measured fluorescence intensities to jet fluid concentration, but only to distinguish between mixed and unmixed fluid (see figure 5-7 and the related discussion). At any given time, the instantaneous probability of finding unmixed ambient fluid at a particular point on the jet axis, $p_o(0,t)$, corresponded to the fraction of the 1024 pixels imaging unmixed ambient fluid. Measurements of $p_o(0,t)$ at $Re = 1,500$ and $Re = 5,000$ are shown in figure 4-16.

Note that $p_o(0,t)$ varies considerably in time. These data indicate that the probability of finding unmixed ambient fluid at a point on the jet axis in the far field shows marked increases at intervals typically separated by about one local characteristic large scale time of the flow. Such increases in the probability of finding pure ambient fluid are consistent with the entrainment mechanism described in the conceptual picture of organized jet entrainment and mixing in Section 3.5 and by Dimotakis et al (1983a).

In figure 4-16, the time-averaged probability of detecting unmixed ambient fluid, $\overline{p}_o(0)$, is 29% at $Re = 1,500$ and only 3% at $Re = 5,000$. To a certain extent, this difference may be ascribed to the decrease in relative spatial resolution of the measurement at the higher Reynolds number. The effect of resolution on these measurements can be estimated, however, by purposely degrading the effective resolution at the lower Reynolds number by averaging the measured LIF intensity over two or more pixels before applying the mixed/unmixed criterion. The result of such a procedure is shown in figure 4-17, and indicates that the probability of detecting pure ambient fluid falls off rapidly with decreasing resolution. When the effective resolution at $Re = 1{,}500$ is made equivalent to that in the original measurement at $Re = 5{,}000$, however, $\bar{p}_0(0)$ is still 24%. This suggests that there may, in fact, be less unmixed ambient fluid reaching the jet axis at the higher Reynolds number. This point is addressed further in Section 4.9 .

4.9 A Chemical Reaction Method for the Similarity PDF

The self-similarity demonstrated by PDFs of the concentration variable ψ can be used in conjunction with the chemically sensitive LIF technique in Section 3.2 to measure the self-similar form of PDFs in the jet far field without the compromising resolution inherent in any direct concentration measurement. The method exploits the pH-sensitivity of the dye at the molecular scale and the similarity of the PDF in the scaled concentration variable to allow the self-similar form of the concentration PDF for a passive scalar to be determined directly from the mean profile of unreacted jet fluid concentration, which can be measured without resolution error.

As shown in figure 4-18, the jet fluid concentration PDF at any axial location χ on any ray η may be conceptually decomposed into a mixed fluid part, $F(c;\chi,\eta)$, and a part accounting for the unmixed ambient fluid, $\bar{p}_0(\eta)\,\delta(c)$, where $\delta(c)$ denotes the Dirac delta function, so that

$$\mathrm{PDF}(c;\chi,\eta) = F(c;\chi,\eta) + \bar{p}_0(\eta)\,\delta(c) \,. \tag{4.10}$$

The self-similar form of the PDF in the scaled concentration variable ψ may also be decomposed in the same manner to give

$$\mathrm{PDF}(\psi;\eta) = f(\psi;\eta) + \overline{p}_0(\eta)\,\delta(\psi) \,, \tag{4.11}$$

where $f(\psi;\eta)$ is the self-similar form of the mixed fluid part of the PDF.

For a measurement using the chemically-sensitive LIF technique with a stoichiometric mixture ratio ϕ, the PDF of unreacted jet fluid concentration will consist of the previous mixed fluid part $F(c;\chi,\eta)$ truncated at c_ϕ, where

$$c_\phi = (1+\phi)^{-1} \tag{4.12}$$

is the value of c at which the reaction occurs (i.e. at which the dye is rendered non-fluorescent). In addition, the previous unmixed ambient fluid part $\overline{p}_0(\eta)\,\delta(c)$ is, in this case, augmented by the mixed fluid at concentrations below c_ϕ, so that

$$\mathrm{PDF}(c;\chi,\eta) = F(c;\chi,\eta)\,U(c-c_\phi) + \left[\,\overline{p}_0(\eta) + \int_{0^+}^{c_\phi} F(c;\chi,\eta)\,dc\,\right]\delta(c), \tag{4.13}$$

where $U(c-c_\phi)$ is a unit step function at $c = c_\phi$. In terms of the similarity concentration ψ, the reaction occurs at ψ_ϕ, where

$$\psi_\phi = \chi/\phi \,. \tag{4.14}$$

The self-similar form of the PDF in this case will depend parametrically on ψ_ϕ as

$$\mathrm{PDF}(\psi;\psi_\phi,\eta) = f(\psi;\eta)\,U(\psi-\psi_\phi) + \left[\,\overline{p}_0(\eta) + \int_{0^+}^{\psi_\phi} f(\psi;\eta)\,d\psi\,\right]\delta(\psi). \qquad (4.15)$$

While the resolution limitations of any instantaneous concentration measurement do not permit an exact determination of ψ, the inherent linear averaging over each photodiode measurement volume and time responsible for these resolution limitations does allow an exact measurement of the <u>mean</u> concentration $\overline{\psi}$. For every ψ_ϕ in equation (4.13), the local $\overline{\psi}(\psi_\phi;\eta)$ is related to the corresponding PDF by

$$\overline{\psi}(\psi_\phi;\eta) = \int_0^\infty \psi \cdot \mathrm{PDF}(\psi;\psi_\phi,\eta)\,d\psi\ . \qquad (4.16)$$

Substituting $\mathrm{PDF}(\psi;\psi_\phi,\eta)$ from (4.15) gives

$$\overline{\psi}(\psi_\phi;\eta) = \int_{\psi_\phi}^\infty \psi \cdot f(\psi;\eta)\,d\psi\ . \qquad (4.17)$$

The mixed fluid part of the similarity PDF, $f(\psi;\eta)$, can then be obtained from equation (4.17) by differentiating with respect to the lower limit to give

$$f(\psi_\phi;\eta) = -\frac{1}{\psi_\phi}\frac{d}{d\psi_\phi}\overline{\psi}(\psi_\phi;\eta)\ . \qquad (4.18)$$

The remaining unmixed fluid part of the similarity PDF, $\overline{p}_0(\eta)\,\delta(\psi)$, can then be determined from the normalization condition as

$$\overline{p}_0(\eta) = 1 - \int_{0^+}^{\infty} f(\psi;\eta)\, d\psi \; . \qquad (4.19)$$

Equations (4.18) and (4.19) permit the complete self-similar form of the concentration PDF to be determined, without resolution error, from a single measurement of the mean profile of unreacted jet fluid concentration along any ray η in the jet.

Koochesfahani (1984) has proposed a chemical reaction method for the plane turbulent shear layer which, in that case, yields the exact mean profile for the product concentration across the layer. The exact PDFs for a passive scalar concentration could, in principle, be determined across the shear layer from a large number of such measurements at differing values of ϕ. The chemical reaction method described above for the jet, however, takes advantage of the self-similarity displayed by PDFs of the variable ψ to directly yield the exact self-similar form of the concentration PDF from a single measurement. If the self-similarity in the PDF on which this method is based were valid for all $\chi > 0$, then the PDF could be determined for all $\psi \geqq 0$. However, as was shown in Section 4.6, the self-similar mixing characteristic of the jet far field appears to be reached for $\chi > 20$, so in principle $f(\psi;\eta)$ in equation (4.18) can only be determined for $\psi > 20/\phi$.

The self-similar form of the PDF on the jet axis was measured using this chemical reaction method, with ϕ ranging from 23.5 to 28 . To reduce beam refraction difficulties in these measurements with the chemically sensitive LIF technique, the densities of the jet fluid (base) and ambient fluid (acid) were matched by dissolving salt (Na_2SO_4) in the ambient fluid. In practice, the PDF could only be determined for $\psi \geqq 3$ using this method, this limitation presumably being imposed by the sensitivity of the method to the asymptotic approach of the PDF to strict self-similarity. Figure 4-19a reasonable agreement between the simialrity PDFs from two separate measurements with this chemical reaction method at $Re = 5{,}000$ and the PDF determined from the direct concentration measurements in Section 4.4. The differences at low values of ψ are qualitatively as would be expected from the resolution limitations of the direct measurement. The similarity PDFs from two measurements with the chemical reaction method at $Re = 20{,}000$ are shown in figure 4-19b. Note that, while the highest concentrations in these PDFs remain essentially unchanged when the Reynolds number is increased from 5,000 to 20,000, these results suggest that the shape of the PDF may undergo a change over this range of Reynolds number (see also the related discussion in Section 3.3).

The values of $\overline{p}_o(0)$ obtained from these measurements with the chemical reaction method are shown in Table 3 together with the estimates from the direct concentration measurements in Section 4.8. It should be noted that, in view of the inability to determine the similarity PDF for $\psi \leqq 3$, the values of $\overline{p}_o(0)$ obtained from these measurements must also be considered approximations. These values do, however, exceed those obtained by the direct measurements, as would be expected. More importantly, and regardless of their absolute values, they confirm the trend toward decreasing values of $\overline{p}_o(0)$ with increasing Reynolds number, suggested by the direct measurements. increasing Reynolds number. It is concluded, therefore, that less unmixed ambient fluid reaches the jet centerline as the Reynolds number is increased over this range. This observation appears to be consistent with the observation by Ricou & Spalding (1961) that the jet entrainment rate decreases with increasing Reynolds number, reaching its Reynolds number independent rate at $Re \approx 25{,}000$.

	Direct Measurement	Chemical Reaction Method
Re	$\bar{p}_o(0)$	$\bar{p}_o(0)$
1,500	0.28 (0.24)[1]	—
5,000	0.03	0.13
20,000	—	0.01

Table 3. $\bar{p}_o(0)$ vs. Re from various measurements. ([1] Denotes value at $Re = 1{,}500$ with resolution equivalent to direct measurement at $Re = 5{,}000$.)

CHAPTER 5

RADIAL CONCENTRATION MEASUREMENTS

Instantaneous radial profiles of jet fluid concentration were measured with high resolution using a passive LIF scalar technique in conjunction with linear photodiode array imaging and high speed digital data acquisition. These measurements were recently reported (Dahm & Dimotakis 1985) and were similar in many respects to the axial concentration measurements described in Chapter 4.

5.1 The Radial Measurement Technique

As was the case for the axial concentration measurements in Chapter 4, the laser fluorescent dye was premixed with the jet fluid and discharged into the ambient fluid. Filtered softened water, fixed at $pH \approx 9$ by the addition of NaOH, was again used for both the jet and ambient fluids. No chemical reaction was involved in these measurements.

The argon ion laser beam (514.5 nm) was again collimated, but for these measurements was oriented to cross that jet radially at $\chi = 300$, perpendicular to the jet axis. The laser induced fluorescence from mixed fluid along the beam was imaged onto the 1024-element Reticon self-scanning linear photodiode array. In this case, the fluorescence from a small transparent vessel containing a circulating solution of dye at a known concentration, positioned about one-and-a-half local jet diameters from the centerline, was also imaged onto the array to set the reference condition for the line attenuation integral. An orange filter eliminated any directly scattered laser light. The array was again clocked at a pixel rate of 256 kHz, corresponding to a scan rate of 235 scans/sec (including a blanking period of 64 additional clock cycles per scan), giving a scan time of 4.3 msec and yielding successive instantaneous profiles of the fluorescence intensity along the beam. A schematic of the imaging configuration is shown in figure 5-1 .

Instantaneous radial profiles of the fluorescence intensity across the jet were measured at $Re = 1,500$ and $Re = 5,000$. From Table 2, the Kolmogorov passage time λ_ν/u at $\chi = 300$ for each of these Reynolds numbers is estimated to be 107 msec and 13 msec, respectively. Comparing these times to the array scan time of 4.3 msec indicates that temporal resolution was not an issue in these radial measurements. Each of the 1024 array pixels had a sensitive detector aperture of $25\mu m \times 26\mu m$. The imaging optics used in this case produced an image ratio of 26:1, and the beam diameter again varied from roughly 0.5 mm to about 1 mm, thereby defining the measurement volume corresponding to each pixel. From Table 1, the Kolmogorov scale λ_ν at each of these Reynolds numbers is estimated to be 1.2 mm and 0.5 mm, respectively, indicating that the even smallest turbulent scales of motion can be resolved at the lower Reynolds number, while at the higher Reynolds number nearly the full range of turbulent scales can be resolved. As was the case for the axial measurements in Chapter 4, at neither Reynolds number could the strain-limited molecular diffusion layer thickness (the Batchelor scale) be resolved, which at this Schmidt number is approximately 25 times smaller than the Kolmogorov scale at each Reynolds number.

Since the scan time was fast relative to the local time scales in the flow, only every 16th scan of the array was recorded on the disk at $Re = 1{,}500$, while every 6th array scan was recorded at $Re = 5{,}000$. Each measurement again consisted of 4000 recorded array scans (in excess of 4 million individual measurements of fluorescence intensity), spanning approximately 12 local characteristic large scale flow times, this limit again being imposed by the duration of each experiment.

The measured instantaneous fluorescence intensity profiles were subsequently converted to instantaneous profiles of jet fluid concentration using the technique outlined in Appendix E.3. These instantaneous concentration profiles were then expressed in the conventional radial self-similar form $g(\eta,t)$, where $\eta = r/x$, by normalizing each individual profile by the local mean centerline concentration as

$$g(\eta,t) = \frac{c(\eta,t;\chi)}{\bar{c}(0;\chi)} \quad . \tag{5.1}$$

5.2 Mean Profiles from Radial Measurements

The mean radial concentration profile, determined by an ensemble average of the 4000 individual concentration profiles measured at $Re = 5{,}000$ in these experiments, compares well in figure 5-2 with the mean profiles reported from other experiments. Note that this form of the radial variable η does not force the profiles to match at the jet half-width, and thus provides a more rigorous comparison than does normalization of the radial coordinate by the concentration half-width.

The radial profile of rms concentration fluctuations measured in these experiments at $Re = 5{,}000$ is shown in figure 5-3, together with the profiles reported from other experiments. In the top curve of this figure, the concentration fluctuation profiles match at $\eta = 0$ as a result of the normalization chosen and show reasonable agreement over the remainder of the profile. If, however, as in the lower curve of figure 5-3, the rms concentration fluctuation intensities are compared, the various profiles do not agree well. This is directly related to the observation in Section 4.2 that the conventionally defined concentration fluctuation intensities in the jet far field are <u>not</u> independent of χ. Even if the various measurements in figure 5-3 were completely accurate, the fluctuation intensity profiles would still be expected to differ simply because the measurements were made at different axial locations.

5.3 Measurements of Concentration Time Histories

Temporal traces of the concentration $g(\eta,t)$ at several values of η, measured at $\chi = 300$ and $Re = 5{,}000$, are shown in figure 5-4. There are several points of particular interest in such traces.

First, as was observed in similar traces along the jet centerline (see Section 4.3), a noteworthy features for all values of η is the absence of the "ramps" that have been observed in such traces in gas-phase (low Sc) jets.

Second, the presence of unmixed ambient fluid deep within the jet is directly evident in these data. This had been observed in the planar LIF visualizations in Section 3.1 and is discussed further in

Section 5.4 .

Furthermore, these traces directly show that when mixed fluid is detected near the jet edges (e.g., figure 5-4d) its concentration is not nearly as low as suggested by the mean concentration profile in figure 5-2 . The situation is similar to earlier observations in the turbulent shear layer (Mungal 1983, Koochesfahani 1984) regarding the validity of the mean profile for representing the mixed fluid compositions. The local mean concentration averages over the mixed fluid concentration and the unmixed fluid present within the jet, but is itself a poor representation of the mixed fluid states in the jet. This was noted in Section 3.5 and is discussed further in Section 5.4 .

Lastly, intervals can be seen in the traces in figure 5-4 during which the concentration fluctuates less rapidly.

5.4 Instantaneous Radial Concentration Profiles

Several representative instantaneous radial concentration profiles from these measurements at $Re = 5{,}000$, each covering the entire radial extent of the jet, are shown in figure 5-5 .

Perhaps the most significant feature of such instantaneous profiles is how little they resemble the mean profile in figure 5-2 . Most of these instantaneous profiles can be qualitatively classified into either a "top-hat" type, such as those in figures 5-5a and 5-5b, where the mixed fluid concentrations across the entire jet diameter are within a relatively narrow range of values (compared with what the mean profile suggests), or a "two-level" type, such as figures 5-5c and

5-5d, where the mixed fluid concentrations in a large region near the jet axis are within one such narrow range of values, while the mixed fluid concentrations across the remainder of the jet are within a second, lower range of values. Broadwell & Breidenthal (1982) have noted that such "top-hat" shapes in the mixed fluid compositions can also be recognized in instantaneous concentration profiles from plane turbulent jets by Uberoi & Singh (1975).

Furthermore, the instantaneous profiles in figure 5-5 also confirm that unmixed ambient fluid can be found deep within the jet. The mean concentration profile in figure 5-2 then results from an average over these top-hat and two-level instantaneous mixed fluid profiles and the unmixed ambient fluid present within the jet, but is itself a poor representation of the mixed fluid states within the jet. As was noted in Section 3.5, the fundamental differences between these instantaneous profiles and the conventional mean profile may have particularly important implications for the modeling and prediction of chemical reactions between the jet and ambient fluids.

The instantaneous concentration profile shapes in figure 5-5 can be reconciled with the idealized picture of the instantaneous concentration field of the jet described in Section 3.5. As shown in figure 5-6, the approximately uniform mixed fluid composition within large regions in the jet leads to the top-hat and two-level instantaneous profile shapes shown schematically.

The mean mixed fluid concentration profile can be determined from these measurements. The effect of varying the mixed/unmixed threshold level, expressed as a percent of the mean centerline concentration, is shown in figure 5-7. Note that the profile is largely insensitive to the threshold level over this range of values. The resulting mean mixed fluid concentration profile, $\bar{g}_m(\eta)$, using the 5% threshold is shown in figure 5-8. The profile $\bar{g}_m(\eta)$, however, is still not a good representation of the top-hat and two-level instantaneous profiles. This is notably different from the corresponding situation in the turbulent shear layer, where the observation (Konrad 1976, Koochesfahani 1984) that the instantaneous mixed fluid composition is at all times nearly uniform across the layer leads to an essentially uniform mean mixed fluid concentration profile, which in that case may be a useful conceptual picture of the instantaneous mixed fluid states in the layer (see also Broadwell & Breidenthal 1982).

Within the resolution limitations inherent in these direct concentration measurements, the time-averaged probability of finding unmixed ambient fluid at any given point on the ray η, namely $\bar{p}_o(\eta)$, can be determined from the mean concentration profile in figure 5-2 and the mean <u>mixed</u> fluid concentration profile in figure 5-7 as

$$\bar{p}_o(\eta) = 1 - \frac{\bar{g}(\eta)}{\bar{g}_m(\eta)} \quad . \tag{5.2}$$

The resulting profile at $Re = 5{,}000$ is shown in figure 5-9. The profile is also compared to the "intermittency", γ, obtained by Antonia et al (1975) from temperature measurements in a heated air jet (low Sc) at $Re \approx 46{,}000$ and by Chevray & Tutu (1978) from velocity measurements in an air jet at $Re \approx 400{,}000$. It must be borne in mind, however, that the interpretation of their "intermittency" may not be directly equivalent to $\bar{p}_o$ in these measurements. Assuming that these quantities can be related, it is noteworthy that they compare as well as they do in view of the range of Reynolds numbers and Schmidt numbers represented.

5.5 η-t Diagrams of Concentration in the Jet

The instantaneous concentration profiles from these measurements can be simultaneously interpreted in the form of η-t reconstructions of the jet concentration field, as shown in figure 5-10 . These are again photographs of a 512×512 digital image display screen, in this case displaying the concentration data from the 512 array elements centered on the jet axis and extending over the entire jet width for 500 successive instantaneous profile measurements. In this case, the 256 different grey levels denote the various normalized concentrations $g(\eta,t)$, with pure white corresponding to $g = 1.5$ and decreasing linearly to pure black, denoting $g = 0$, namely unmixed ambient fluid. These are, therefore, η-t reconstructions of the jet concentration field. It must be emphasized that these are not equivalent to still photographs of the concentration field in a plane, such as those in Section 3.1, as becomes evident near the jet edges.

It is apparent in the data in figure 5-10 that, at both Reynolds numbers, unmixed ambient fluid is transported throughout the entire radial extent of the jet. This figure also suggests that the topology of a stoichiometric surface between the mixed and unmixed fluids, commonly used in combustion studies, may be considerably more complex than that which might be suggested by the classical picture of mixing in turbulent jets. Furthermore, as the individual concentration profiles in figure 5-5 suggested, the data in figure 5-10 show that the instantaneous mixed fluid composition is approximately uniform, relative to what the mean concentration profile would suggest, across a large part of the local jet diameter. These same data are shown in figure 5-11 with color assignments denoting the various concentration levels. The uniformity of the mixed fluid composition within large regions in the jet is evident in this figure.

A composite sequence from consecutive photographs of the type shown in figure 5-10 is shown, for each Reynolds number, in figure 5-12 . Each of these sequences displays over 2 million individual concentration measurements. This method of displaying the measured profiles allows a direct interpretation of the time-varying concentration field in these data.

5.6 Radial PDFs of Concentration

PDFs of the concentration $g(\eta,t)$, measured at $Re = 1{,}500$ and $5{,}000$, are shown for several values of η covering the entire radial extent of the jet in figures 5-13a and 5-13b . Note that the PDFs displayed in this form, together with the self-similarity of the PDFs in the scaled concentration variable ψ noted in Section 4.5 , allow the concentration PDF for a passive scalar to be determined any point in the jet far field.

CHAPTER 6

DISCUSSION

6.1 Organized Mixing in the Jet Far Field

Strong evidence for organized mixing in the far field of turbulent jets is provided by the roughly periodic large scale fluctuation of the flame lengths of chemically reacting jets, noted in Section 3.4.1 . The scaling laws in Section 3.4.2 for these flame length fluctuations verify that the fluctuations occur at the local characteristic large scale length and time of the flow at all axial locations in the jet far field.

The visualizations of entrainment and mixing in the jet far field using the planar LIF technique in figures 3-4 a-c directly show the transport of unmixed ambient fluid deep into the jet. These visualizations also show the existence of large regions in the jet within which the composition of mixed fluid is nearly uniform. The flame length fluctuations of chemically reacting jets are a direct manifestation of these large regions. The scaling laws for these regions of nearly uniform mixed fluid composition show that they span approximately one local jet diameter in both the axial and radial directions in the jet far field, and lead to the idealized picture of the instantaneous concentration field of the jet shown in figure 3-19 .

The features of this picture of organized entrainment and mixing in the far field of turbulent jets are borne out by the direct concentration imaging measurements in Chapters 4 and 5 . Specifically, the instantaneous radial concentration profile measurements confirm the existence of unmixed ambient fluid deep within the jet and the presence of large regions in the jet within which the mixed fluid composition can be nearly uniform. χ-t diagrams constructed from successive individual axial concentration profiles show these same features.

6.2 The Conceptual Model of Organized Jet Mixing

The conceptual model of organized entrainment and mixing in the far field of momentum-driven turbulent jets is shown in figure 3-19 and discussed in Section 3.5 .

Several additional details of the model can be determined directly from the jet scaling laws. For example, since the axial extent of each region is roughly one local jet diameter, the average spacing between the centers of these regions can be determined. With

$$\delta(\chi) \approx 0.44\,\chi \,, \tag{6.1}$$

the spacing between the centers of any two successive regions, "i" and "i+1", must conform to the requirement

$$\chi_{i+1} \approx \chi_i + \frac{1}{2}\,\delta(\chi_i) + \frac{1}{2}\,\delta(\chi_{i+1}) \,. \tag{6.2}$$

Using $\delta(\chi)$ from equation (6.1) gives

$$\chi_{i+1} \approx \chi_i + 0.22\,\chi_i + 0.22\,\chi_{i+1} \,, \tag{6.3}$$

giving the typical positions of the centers as

$$\chi_{i+1} \approx 1.56\,\chi_i \,. \tag{6.4}$$

Similarly, the average "jump" in the jet fluid concentration of the mixed fluid in going from one of these regions to the next can also be determined. The χ^{-1} scaling required of the mean concentration along rays in the jet requires that

$$\chi_i \cdot \bar{c}_i = \chi_{i+1} \cdot \bar{c}_{i+1} . \qquad (6.4)$$

The spacing in equation (6.4) then gives

$$\bar{c}_{i+1} \approx 0.64 \, \bar{c}_i . \qquad (6.5)$$

Similarity of mixing in the jet far field requires that the average fraction of each region occupied by unmixed ambient fluid is the same for every region. As a result, in going from one region to the next, the jet fluid concentration of the mixed fluid must follow the same scaling as the mean concentration in equation (6.5).

A discussion of the Reynolds number dependence of this picture is appropriate. It is important to bear in mind that the most direct evidence for organized mixing in the jet, namely the nearly periodic large scale flame length fluctuations of chemically reacting jets, persists to the highest Reynolds numbers investigated (in excess of 20,000). In fact, motion picture data such as those discussed in Section 3.4.1 suggest that these fluctuations become even more distinct at the higher Reynolds numbers. This is also borne out by the planar LIF visualizations of the jet concentration field in Section 3.1 (see figures 3-4 a-c), and suggests that the qualitative features of this conceptual picture of jet mixing will persist to higher Reynolds numbers. The measurements in Chapters 4 and 5 have demonstrated, however, that at least some quantitative aspects of this picture may change with Reynolds number over the range of values spanned in these experiments. For example, the amount of unmixed ambient fluid reaching the jet centerline decreases as the Reynolds number is increased from 1,500 to 20,000 . This Reynolds number dependence in the amount of entrained fluid on the jet centerline may be consistent with the observation by Ricou & Spalding (1961) that the jet entrainment rate does not become independent of Reynolds number until $\mathrm{Re} \approx 25{,}000$.

This picture of entrainment and mixing in the far field of turbulent jets differs fundamentally from the classical view jet entrainment and mixing. In the classical view, which has arisen largely from point measurements and flow visualization techniques which are unable to reveal the internal structure of the flow, entrainment and mixing are pictured as resulting from transport by stochastic eddies whose scale is small relative to the local large scale of the flow. If this transport mechanism is correct, it can then be shown that the turbulent fluxes of mass, momentum, energy and scalars would follow gradient transport scaling laws and could be determined from the mean profiles of these quantities. The experiments on which the proposed picture in figure 3-19 is based, however, indicate that entrainment and mixing involve transport at the largest local scales of the flow. Furthermore, the significance of mean profiles for determining the turbulent fluxes, as postulated in gradient transport models, appears questionable since the instantaneous concentration profiles do not resemble the resulting mean profile.

This picture of organized entrainment and mixing in turbulent jets bears certain resemblances to entrainment and mixing in plane turbulent shear layers. In particular, the transport of unmixed fluid deep into the region of shear is common to both flows. In the mixing layer, the role of nearly periodic, large scale, spanwise vortical structures in such transport is, by now, largely understood. Such large scale transport in the jet suggests the presence of a similar large scale vortical structure in that flow, as has been noted by Dimotakis et al (1983a). In addition, the nearly uniform composition of the mixed fluid within large areas in the shear region of both flows is also a common feature. In the mixing layer, the role of the large vortices in preventing gradients in the mixed fluid composition is also understood, and lends further support to the notion of similar large structures in the jet.

Little discussion has been given thus far of the time-evolution of this picture for jet entrainment and mixing, and in particular of the dynamics of these large regions. Such a discussion requires certain assumptions about the vorticity field responsible for this organization. While it has been recognized (Dimotakis et al 1983a) that such vortices could be either axisymmetric, helical or in a transition between these two states, for simplicity the case of axisymmetric vortex rings will be considered. On dimensional grounds, it can be argued that the circulation of such vortex rings must be constant along the axial direction in the far field, and that the ring diameter and spacing must increase proportionally with x. The self-induced velocity of such rings must then decrease along the axial direction, rendering any given ring slower than its upstream neighbor and faster than its downstream neighbor. As a consequence, an ordered configuration of these rings will undergo interactions during which any given ring is "rear-ended" by its upstream neighbor and, in turn, "rear-ends" its downstream neighbor while the overall order in the ring configuration may be maintained. There is evidence of such "rear-ending" in motion picture data of jets visualized with the planar LIF technique, as well as in the χ-t diagrams in Chapter 4 and the earlier x-t diagrams of Dimotakis et al (1983a). However, no quantitative conclusions regarding the dynamics of these jets have been drawn.

In comparing the organized mixing in jets and shear layers, certain characteristic differences must be noted. The organization of mixing in the far field of the axisymmetric turbulent jet appears to be topologically, and perhaps dynamically, more complex than that in the plane turbulent shear layer. The different topologies of these two flows allows visualization of the large vortices in the plane shear layer with integrating methods such as shadowgraph or schlieren, but disguises similar large structures in the jet. It may be for this reason that organization of entrainment and mixing in the jet has eluded earlier flow visualization studies. From the topological and dynamical point of view, the plane turbulent jet might be expected to more closely resemble the planar mixing layer, while the axisymmetric mixing layer may be more significant for the round jet.

Finally, a discussion of the effects of Schmidt number is appropriate. The dynamics of the flow are independent of the mass diffusivity and, consequently, the overall organization of entrainment and mixing will be the same in gas-phase jets as in the present liquid-phase experiments. Similarly, the dimensionless turbulent flame lengths of chemically reacting gas and liquid jets are essentially equal. However, the ramp-like features observed in concentration time histories in gas-phase jets are not observed in similar traces from the present liquid-phase jets. Furthermore, the lower molecular diffusivity in the liquid phase implies that relatively more of the molecular mixing occurs at the small scales of the turbulent cascade in these liquid-phase jets than will be the case in gas-phase jets. In particular, for these liquid-phase jets with $Sc \approx 600$, the strain-limited molecular diffusion layer thickness (the Batchelor scale, see Batchelor 1952) is approximately 25 times smaller than the smallest turbulent scale of transport (the Kolmogorov scale). In the gas phase, with $Sc \approx 1$, the Batchelor scale is approximately equal to the Kolmorogov scale. The specific effects of these differences at the small scales of the flow on the quantitative features of mixing and chemical reactions in jets must await further investigation.

CHAPTER 7

CONCLUSIONS

These experiments have investigated entrainment, turbulent transport and molecular mixing in the far field of steady, axisymmetric, momentum-driven turbulent jets issuing into an unconfined, quiescent medium in the large Schmidt number (liquid-phase) regime. Direct visualizations of entrainment and mixing in such jets by planar laser induced fluorescence techniques and line imaging measurements of instantaneous concentration profiles by a passive scalar technique were used over the range of Reynolds number from 1,000 to 20,000 and for axial distances extending from the jet exit to 300 momentum diameters downstream. A summary of the results is presented below :

1. The instantaneous concentration field of such jets is organized into large regions spanning approximately one local jet diameter in both the axial and radial directions, containing both mixed fluid and unmixed ambient fluid. The jet fluid concentration in the mixed fluid is nearly uniform within each of these regions.

2. Unmixed ambient fluid is transported deep into the jet by large scale motions and mixes into these large regions primarily from the rear, producing slightly lower jet fluid concentrations in the mixed fluid near the rear of these regions.

3. In chemically reacting jets, this large scale organization in the jet concentration field manifests itself as a roughly periodic, large scale fluctuation of the flame length.

4. The time-varying probability of finding unmixed ambient fluid at a given point in the jet shows marked increases typically separated by about one local characteristic large scale time of the flow.

5. The time-averaged probability of finding unmixed ambient fluid at various points across the jet agrees with profiles of the "intermittency" measured in low Schmidt number (gas-phase) jets, supporting the notion that ambient fluid is brouht into the jet primarily at large scales.

6. Instantaneous profiles of the jet fluid concentration across the jet typically have a "top-hat" or "two-level" shape resulting from the nearly uniform composition of the mixed fluid within these large regions. The conventional mean concentration profiles across the jet give a misleading representation of the expected mixed fluid compositions in the jet.

7. The resulting picture of the instantaneous concentration field of the jet does not resemble that predicted by gradient transport models. It suggests, instead, that entrainment and mixing in jets are dominated by the large scale organization of the flow.

8. The jet "momentum diameter" d^* properly non-dimensionalizes the axial coordinate x in the far field of all momentum-driven turbulent jets as $\chi = x/d^*$, regardless of the details of their

velocity and density profiles at the jet source, or of the absolute densities or diffusivities of the jet and ambient fluids.

9. The scaling constant in the resulting dimensionless form of the mean concentration scaling law along the centerline in the jet far field has been determined to be approximately 5.4 ± 0.14 .

10. The molecular mixing rate in the jet far field reaches a constant value and becomes independent of Reynolds number at $Re \approx 3{,}000$. At Reynolds numbers above 3,000, the lower bound for the molecular mixing rate is at least one-third of the jet entrainment rate.

11. At any axial location χ in the far field, the jet has already entrained a sufficient amount of ambient fluid to, in principle, mix every part of jet fluid molecularly to the mixture ratio $\chi/10$, however such mixing of every part of jet fluid to at least this mixture ratio is not actually accomplished until the axial location 3χ .

12. Concentration time histories in such large Schmidt number jets do not display the characteristic "ramp-like" features previously observed in similar time histories in low Schmidt number gas-phase) jets.

13. Probability density functions (PDFs) of a proposed scaled concentration variable, $\psi = \chi/\mu$ with $\mu = \frac{1-c}{c}$ and with c the conventional jet fluid concentration, are self-similar along rays in the jet far field.

14. PDFs of the similarity concentration ψ along the jet centerline show that the self-similar mixing which characterizes the jet far field is reached by $\chi \approx 20$.

15. PDFs of the jet fluid concentration along the jet radius, together with the self-similarity displayed by PDFs of ψ, allow the concentration PDF to be determined everywhere in the jet far field.

16. A chemical reaction method allows the self-similar form of these PDFs to be determined along rays in the jet without the compromising resolution associated with any direct measurement of the PDF.

17. The amount of unmixed ambient fluid reaching the jet centerline decreases when the Reynolds number is increased from 1,500 to 20,000 .

18. The conventional jet fluid concentration fluctuation intensities, which are generally assumed to reach a constant level in the jet far field, are found not to attain such a constant level for axial distances as large as $\chi = 300$. The self-similarity demonstrated by PDFs of the proposed similarity concentration variable ψ necessarily implies that fluctuation intensities of this scaled concentration will reach a constant level by $\chi \approx 20$.

APPENDIX A

THE MEAN CONCENTRATION SCALING IN THE FAR FIELD

The mean concentration scaling law along the jet centerline is used in Section 4.2 to validate the axial imaging technique for measuring instantaneous concentration profiles along the jet axis. While the x^{-1} functional form of this scaling law is well known, the coefficient in the scaling law has not been determined accurately. Chen & Rodi (1980) suggest the value of this scaling coefficient from a number of experiments as being about 5 .

In the following analysis, an integral mass balance and self-similar radial mean profiles of concentration and velocity are used to obtain a more accurate value for this scaling coefficient. In addition, this analysis leads to the proper dimensionless form of the axial coordinate of the concentration field for all momentum-driven turbulent jets, regardless of the details of their velocity and density profiles at the jet source, or of the absolute densities or mass diffusivities of the jet and ambient fluids.

A.1 The Mass Flux Averaged Concentration

At axial distances for which the mass flux of the jet, $\dot{m}(x)$, defined as

$$\dot{m}(x) = \int_0^\infty \overline{\rho(x,r)\, u(x,r)}\; 2\pi r \, dr \ , \tag{A.1}$$

is sufficiently large compared to its source mass flux, $\dot{m}_o$, the jet may be characterized solely by its momentum flux, J_o, and the ambient fluid density, ρ_∞. The scaling law for the jet mass flux can then be derived from dimensional consideration as

$$\dot{m} = \dot{m}(\,x\,;\,\rho_\infty, J_o) \quad \rightarrow \quad \dot{m}(x) \sim (\rho_\infty J_o)^{1/2} \cdot x\,. \tag{A.2}$$

Measurements by Ricou & Spalding (1961) have verified this functional form and suggest the complete relation

$$\dot{m}(x) \;=\; 0.282\,(\rho_\infty J_o)^{1/2} \cdot x\,. \tag{A.3}$$

From an integral mass balance, the jet fluid concentration, density and velocity fields can be related to the mass flux of the jet source, $\dot{m}_o$, as

$$\int_0^\infty \overline{c(x,r)\,\rho(x,r)\,u(x,r)}\;2\pi r\,dr \;=\; \dot{m}_o\,. \tag{A.4}$$

Using $\dot{m}(x)$ from equation (A.1), equation (A.4) can be written as

$$\frac{\displaystyle\int_0^\infty \overline{c(x,r)\,\rho(x,r)\,u(x,r)}\;2\pi r\,dr}{\displaystyle\int_0^\infty \overline{\rho(x,r)\;u(x,r)}\;2\pi r\,dr} \;=\; \frac{\dot{m}_o}{\dot{m}(x)}\,, \tag{A.5}$$

where the ratio of integrals is the "mass flux averaged" jet fluid concentration. With $\dot{m}(x)$ from equation (A.3), equation (A.5) can be written as

$$\frac{\int_0^\infty \overline{c(x,r)\,\rho(x,r)\,u(x,r)}\;2\pi r\;dr}{\int_0^\infty \overline{\rho(x,r)\;u(x,r)}\;2\pi r\;dr} = 3.14\;\frac{2\,\dot{m}_o}{(\pi\rho_\infty J_o)^{1/2}}\;x^{-1}\;. \qquad (A.6)$$

A.2 The Jet Momentum Diameter d^*

The grouping on the right side of equation (A.6) suggests a proper dimensionless form for the axial coordinate x of the jet far field. We will define the jet "momentum diameter", d^*, as

$$d^* = \frac{2\,\dot{m}_o}{(\pi\rho_\infty J_o)^{1/2}}\;. \qquad (A.7)$$

Physically, d^* is the diameter through which fluid at density ρ_∞ would flow with mass flux $\dot{m}_o$ and momentum flux J_o. Note that, if the density and velocity profiles at the jet source are uniform, then

$$d^* = \left(\frac{\rho_o}{\rho_\infty}\right)^{1/2} d_o\;. \qquad (A.8)$$

If, furthermore, $\rho_o = \rho_\infty$, then we simply have

$$d^* = d_o\;, \qquad (A.9)$$

where d_o is the physical diameter of the jet source.

This momentum diameter was first introduced by Thring & Newby (1952), and has been used by Avery & Faeth (1974) and by Becker et al (1978a,b) to correlate the flame lengths of a variety of turbulent reacting jets. However, equation (A.6) suggests a universal scaling with d^* in the form of a dimensionless axial coordinate for the far field of all momentum-driven turbulent jets, defined as

$$\chi = (x/d^*) \ . \tag{A.10}$$

If the coordinate x includes a "virtual origin" x_o, then the appropriate form would be $\chi = (x-x_o)/d^*$. The correlation demonstrated in figure 3-12 for the wide range of density ratios and mass diffusivities represented is a strong verification of the validity of this dimensionless coordinate for all momentum-driven turbulent jets.

Note that, if we examine the scaling law for velocity from dimensional analysis, namely,

$$u = u(x\,;\,\rho_\infty, J_o) \quad \rightarrow \quad u(x) \sim (\rho_\infty J_o)^{1/2} \cdot x^{-1} \ , \tag{A.11}$$

and non-dimensionalize the velocity by $(J_o/\dot{m}_o)$, we obtain

$$\frac{u(\chi)}{(J_o/\dot{m}_o)} \sim \chi^{-1} \ , \tag{A.12}$$

where the same form of the dimensionless axial coordinate appears. Avery & Faeth (1974) have correlated the centerline velocities of momentum-driven turbulent jets over a wide range of density ratios using this form (see their figure 8).

A.3 The Mean Centerline Concentration Scaling Law

The concentration, density and velocity fields appearing in equation (A.6) can be expressed in terms of their conventional temporal mean and fluctuating components as

$$c(x,r) = \overline{c}(x,r) + c'(x,r) \quad (A.13a)$$

$$\rho(x,r) = \rho_\infty + \overline{\Delta\rho}(x,r) + \Delta\rho'(x,r) \quad (A.13b)$$

$$u(x,r) = \overline{u}(x,r) + u'(x,r) \ . \quad (A.13c)$$

If radial profiles of the mean and fluctuation correlation terms, which arise when equations (A.13a) ••• (A.13c) are introduced in equation (A.6), are self-similar, then profiles of these quantities can be expressed in terms of their centerline values as

$$\overline{c}(x,r) = \overline{c}(x)\ f(\eta) \quad (A.14a)$$

$$\overline{\Delta\rho}(x,r) = \overline{\Delta\rho}(x)\ g(\eta) \quad (A.14b)$$

$$\overline{u}(x,r) = \overline{u}(x)\ h(\eta) \quad (A.14c)$$

$$\overline{c'\Delta\rho'}(x,r) = \overline{c}(x)\,\overline{\Delta\rho}(x)\ i(\eta) \quad (A.14d)$$

$$\overline{\Delta\rho' u'}(x,r) = \overline{\Delta\rho}(x)\,\overline{u}(x)\ j(\eta) \quad (A.14e)$$

$$\overline{c'u'}(x,r) = \overline{c}(x)\,\overline{u}(x)\ k(\eta) \quad (A.14f)$$

$$\overline{c'\Delta\rho' u'}(x,r) = \overline{c}(x)\,\overline{\Delta\rho}(x)\,\overline{u}(x)\ l(\eta)\ , \quad (A.14g)$$

where

$$\eta = \frac{r}{x} \quad (A.15)$$

and

$$f(\eta) = \frac{\overline{c}(\eta)}{\overline{c}(0)}\ , \qquad g(\eta) = \frac{\overline{\Delta\rho}(\eta)}{\overline{\Delta\rho}(0)} \quad (A.16a,b)$$

$$h(\eta) = \frac{\overline{u}(\eta)}{\overline{u}(0)} , \qquad i(\eta) = \frac{\overline{c'\Delta\rho'}(\eta)}{\overline{c'\Delta\rho'}(0)} \tag{A.16c,d}$$

$$j(\eta) = \frac{\overline{\Delta\rho'u'}(\eta)}{\overline{\Delta\rho'u'}(0)} , \qquad k(\eta) = \frac{\overline{c'u'}(\eta)}{\overline{c'u'}(0)} \tag{A.16e,f}$$

$$l(\eta) = \frac{\overline{c'\Delta\rho'u'}(\eta)}{\overline{c'\Delta\rho'u'}(0)} . \tag{A.16g}$$

In terms of these self-similar profiles, equation (A.6) gives the scaling law for the mean concentration along the jet centerline as

$$\overline{c}(\chi) = \frac{3.14}{\Lambda(\chi)} \chi^{-1} , \tag{A.17}$$

where

$$\Lambda(\chi) = \frac{I_1 + \dfrac{\overline{\Delta\rho}(\chi)}{\rho_\infty} I_2}{I_3 + \dfrac{\overline{\Delta\rho}(\chi)}{\rho_\infty} I_4} , \tag{A.18}$$

and where $I_1 \cdots I_4$ are integral invariants, given by

$$I_1 = \int_0^\infty [f(\eta)\, h(\eta) + k(\eta)]\ \eta\ d\eta \tag{A.19a}$$

$$I_2 = \int_0^\infty f(\eta)\, g(\eta)\, h(\eta)\ \eta\ d\eta + \int_0^\infty [h(\eta)\, i(\eta) + f(\eta)\, j(\eta) + g(\eta)\, k(\eta) + l(\eta)]\ \eta\ d\eta \tag{A.19b}$$

$$I_3 = \int_0^\infty h(\eta)\ \eta\ d\eta \qquad (A.19c)$$

$$I_4 = \int_0^\infty \left[g(\eta)\,h(\eta) + j(\eta)\right]\ \eta\ d\eta\ . \qquad (A.19d)$$

If the initial densities are matched, or at axial distances for which $\frac{\overline{\Delta\rho}}{\rho_\infty} \ll 1$, then

$$\Lambda(\chi) = \lambda = \frac{I_1}{I_3}\ , \qquad (A.20)$$

giving the scaling law for the mean concentration along the jet centerline as

$$\bar{c}(\chi) = \frac{3.14}{\lambda}\ \chi^{-1}\ . \qquad (A.21)$$

A.4 Evaluation of the Scaling Coefficient

The numerical scaling coefficient in equation (A.21) can be evaluated from the profiles $f(\eta)$, $h(\eta)$ and $k(\eta)$ using equations (A.19) and (A.20). While accurate measurements of the $k(\eta)$ profile for the jet are not readily available in the literature, there are indications (Dibble et al 1984) that, to a good approximation, the contribution from $\overline{c'u'}$ to the integral mass balance can be neglected. The profile $f(\eta)$ is given in figure 5-2, while the profile $h(\eta)$ is available in the literature (e.g., Wygnanski & Fiedler 1969). Using these profiles, a simple numerical quadrature gives

$$\lambda \approx 0.551\ , \qquad (A.22)$$

thereby giving the complete scaling law for the mean centerline concentration in the jet far field as

$$\bar{c}(\chi) \approx 5.70 \ \chi^{-1} . \qquad \text{(A.23)}$$

The principal features of equation (A.23) are the properly non-dimensionalized form of the scaling law and the numerical value of the scaling coefficient.

The mean concentration profile along the jet centerline is shown in the form $\chi \cdot \bar{c}(\chi)$ for a number of experiments in figure 4-6 . In particular, note that the value of the scaling coefficient in equation (A.23) compares well with the measurements.

APPENDIX B

CHARACTERISTICS OF DISODIUM FLUORESCEIN DYE

Disodium fluorescein belongs to the class of xanthene dyes, a family of water-soluble, organic, laser dyes with a strong absorption band in the visible spectrum and exhibiting spontaneous emission, with very high quantum yields, in the wavelength region from 500 - 700 nm. The absorption and fluorescence characteristics of these dyes are directly attributable to the symmetry of an extended system of alternating single and double bonds. The details of their interaction with an excitation field, however, cannot be derived rigorously from their molecular structure owing to the intractability of the resulting quantum mechanical problem.

Some of the relevant phenomenological features of fluorescein dye are discussed by Koochesfahani (1984). Several others, measured directly or available in the literature, are summarized below. A more complete description of the structure and properties of laser dyes is given by Drexhage (1973).

B.1 Absorption and Emission Spectra

The spectra for absorption and stimulated emission bby aqueous solutions of disodium fluorescein dye, measured by Robben et al (1976), are shown in figure B-1 . It should be kept in mind, however, that the stimulated emission spectrum is not directly equivalent to the fluorescence (spontaneous emission) spectrum for the dye.

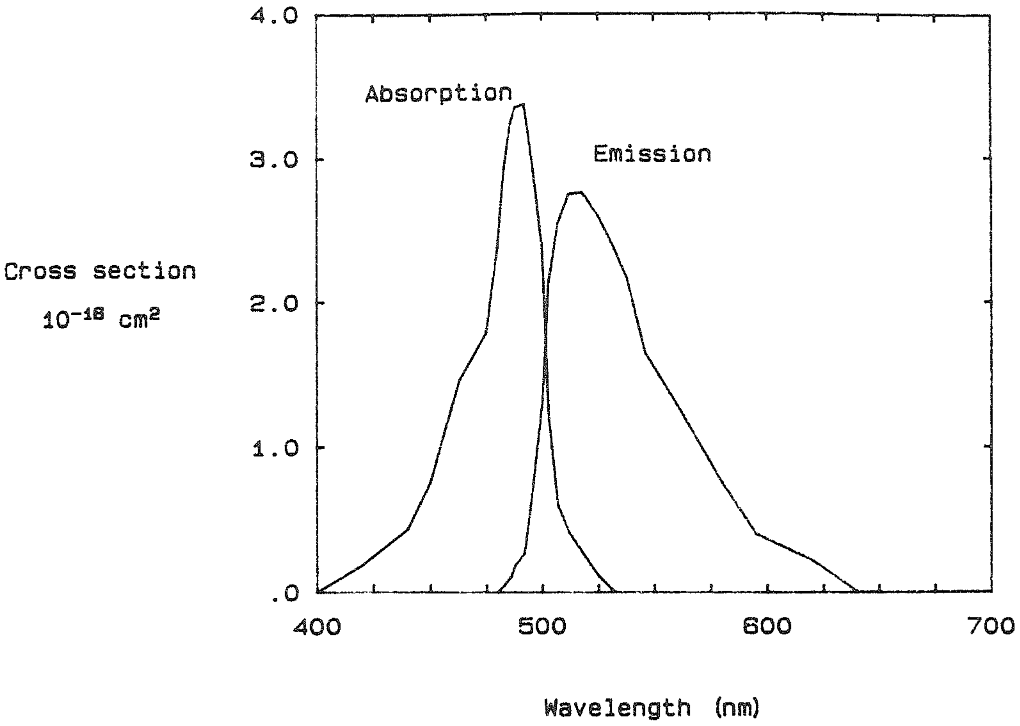

Figure B-1 Spectra for absorption and stimulated emission by disodium fluorescein dye.

Figure B-1 demonstrates that fluorescein absorbs at both the 488.0 nm (blue) and 514.5 nm (green) lines of the argon ion laser. While the peak in the absorption spectrum is very closely matched to the 488.0 nm blue line, the inferior pH-sensitivity of the dye when excited at that wavelength (see Section B.3) made excitation at the 514.5 nm line more desirable. The laser power available in the green line was more than sufficient to accommodate the lower absorption at that wavelength. Furthermore, the relatively small overlap between the absorption and emission spectra in figure B-1 indicates a low probability of an emitted photon being reabsorbed. As a result, the dye can be treated as being optically transparent to its own emission.

B.2 Beam Attenuation Characteristics

Absorption of photons from the excitation field by dye molecules produces a consequent attenuation in the excitation field intensity. The resulting fractional attenuation per unit length can be determined as a function of the dye concentration by a simple procedure. The intensity of a beam propagating through a uniform concentration dye solution can be expressed (see Section E.3) as

$$\frac{P(L)}{P_o} = e^{-I[C]\cdot L} , \tag{B.1}$$

where P_o is the beam intensity entering the solution and $P(L)$ the exiting intensity after propagating through the dye for a distance L, with $I[C]$ the fractional beam attenuation per unit propagation length at the concentration C. Using a power meter to measure P_o and $P(L)$, $I[C]$ can be found from

$$I[C] = -\frac{1}{L} \ell n \frac{P(L)}{P_o} . \tag{B.2}$$

Such a calibration for $I[C]$ is shown in figure B-2, where C is expressed as a nominal molar concentration. For nominal dye concentrations below about $2(10^{-5})$ M, $I[C]$ is linear in the dye concentration and may be expressed as

$$I[C] = \zeta \cdot C , \tag{B.3}$$

where the constant ζ is determined from the calibration.

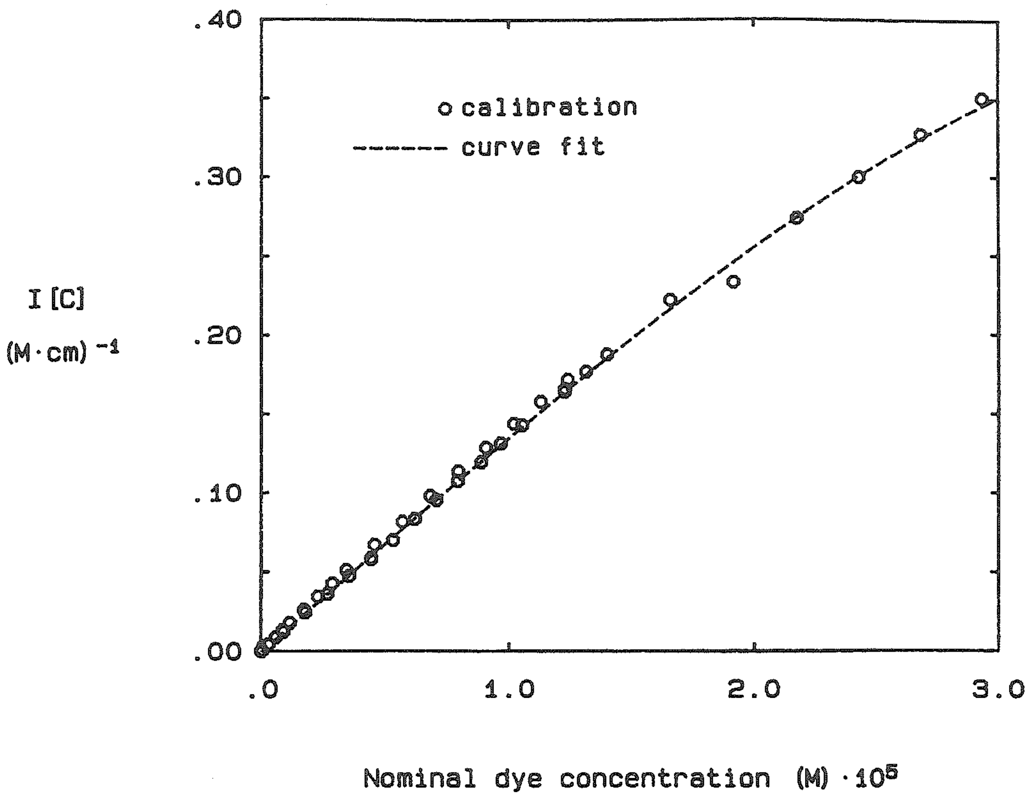

Figure B-2 Calibration for I[C].

B.3 pH-Sensitivity of the Fluorescence Intensity

The symmetry in the conjugate bond structure of the fluorescein chromophore responsible for the resonant absorption of photons can be interrupted when one or more H^+ ions, present in acidic solutions, associates with an end group of the chromophore. The probability that any given fluorescein molecule will exhibit a reduced capacity for resonant absorption will depend on the instantaneous local concentration of H^+ ions (i.e., the local solution pH) and on the wavelength of the excitation photons. This mechanism gives rise to a reversible, wavelength-dependent pH variation in the fluorescence intensity of fluorescein solutions.

A direct measurement of the variation in fluorescence intensity with pH for fluorescein excited at 514.5 nm is shown in figure B-3. For pH > 7.5, the dye fluoresces at its maximum strength independent of the pH, while for pH < 3, the dye is rendered essentially non-fluorescent. The corresponding pH-sensitivity calibration at 488.0 nm indicates that the fluorescence transition at that wavelength is not nearly as steep and spans a wider range of pH.

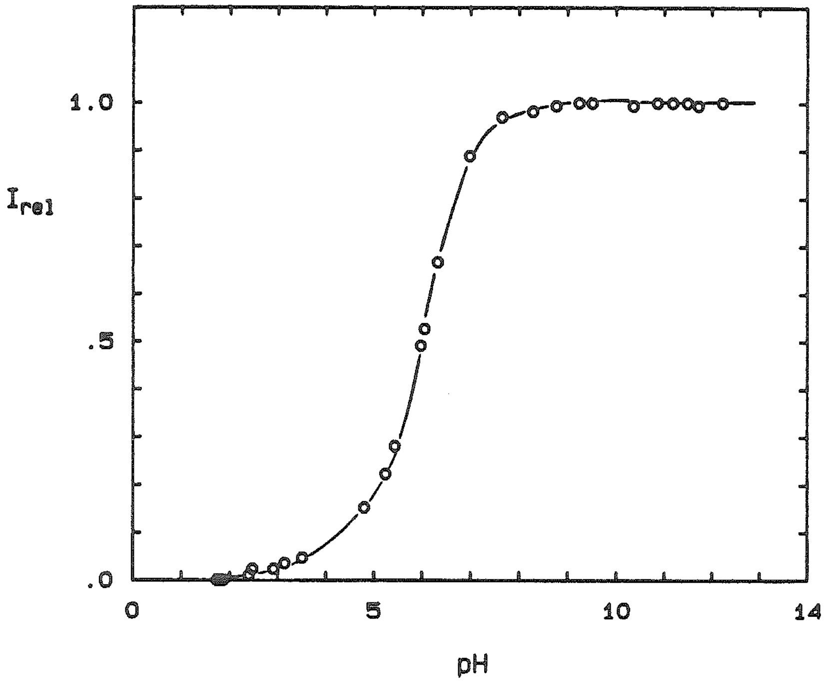

Figure B-3 pH-Sensitivity of the fluorescence intensity for fluorescein dye.

The pH-sensitivity exhibited by fluorescein dye is not found in all members of the xanthene family (e.g. the rhodamines) and is one of the most attractive features of this dye for the purposes of the present investigation.

B.4 Fluorescence Time Scales

Upon absorption of a photon, dye molecules are typically excited from the electronic ground state S_0 to some higher vibrational level within the first excited singlet state S_1, from which they relax, within picoseconds (Drexhage 1973), to the lowest vibrational level of S_1. The subsequent transition $S_1 \rightarrow S_0$ is responsible for spontaneous emission by the dye. Owing to the typically large dipole moment for this transition, the rate of spontaneous emission is very high, with typical radiative lifetimes on the order of nanoseconds (Drexhage 1973). Becker (1969) has measured a fluorescence lifetime of 4 nanoseconds for fluorescein. This fluorescence time scale may be compared with the reaction time of 2 to 20 nanoseconds for the combination of H^+ and OH^- ions in Section C.4 . The fact that, strictly speaking, the fluorescence time scale is not in a fast limit relative to the reaction time scale is of little consequence here, since both times are fast relative to the time scales for turbulent transport and molecular mixing developed in Appendix C .

APPENDIX C

TIME SCALES FOR MIXING AND CHEMICAL REACTION

C.1 The Local Large Scale Time

The local characteristic large scale time of the flow can be defined in terms of the local jet visual diameter, δ, and the local mean centerline velocity, u, as

$$\tau_M = \frac{\delta}{u} . \tag{C.1}$$

In the jet far-field, dimensional consideration requires

$$\begin{aligned} \delta &\approx c_1 \, x \\ u &\approx c_2 \, (J_o/\dot{m}_o) \, \chi^{-1} \quad , \end{aligned} \tag{C.2}$$

where c_1 and c_2 are generally taken to be 0.4 and 6.5, respectively, giving the local large scale time as

$$\tau_M \approx 0.06 \, \frac{d^*}{(J_o/\dot{m}_o)} \, \chi^2 . \tag{C.3}$$

For the case of uniform density and velocity profiles at the jet source with matched densities, equation (C.3) gives

$$\tau_M \approx 0.06 \, \frac{d_o}{u_o} \, \chi^2 . \tag{C.4}$$

C.2 The Local Small Scale Time

The time τ_ν associated with the smallest turbulent scales (the Kolmogorov time) is given by

$$\tau_\nu \sim (\nu/\varepsilon)^{1/2} . \tag{C.5}$$

This small scale time can be locally related to the large scale time τ_M in equation (C.3) as

$$\frac{\tau_\nu}{\tau_M} \sim \mathrm{Re}^{-1/2} . \tag{C.6}$$

C.3 The Molecular Mixing Time

It may be shown that molecular diffusion at any turbulent scale, λ_i, reaches a strain-imposed limiting thickness after a dimensionless time

$$(\sigma_i \cdot t) \approx 1 , \tag{C.7}$$

where σ_i is the local strain rate associated with motions at the scale λ_i, where

$$\sigma_i \sim \frac{u_i}{\lambda_i} . \tag{C.8}$$

The associated velocity scale u_i can be estimated by equating the kinetic energy flux through the scale λ_i to the energy flux into the (inviscid) inertial range of the turbulent cascade to give

$$u_i \approx u \left(\frac{\lambda_i}{\delta}\right)^{1/3} . \tag{C.9}$$

For molecular diffusion at the smallest turbulent mixing scale, λ_ν, this gives the associated strain rate as

$$\sigma_\nu \approx \tau_M^{-1} \cdot Re^{1/2} . \tag{C.10}$$

With $\tau_\nu \leqq t \leqq \tau_M$, the dimensionless time in equation (C.7) is in the range

$$1 < (\sigma_\nu \cdot t) < Re^{1/2} , \tag{C.11}$$

indicating that molecular diffusion at the scale λ_ν is strain-limited.

For such strain-limited diffusion, the molecular diffusion layer thickness, λ_D (the Batchelor scale), is related to the Kolmogorov scale, λ_ν, as

$$\frac{\lambda_D}{\lambda_\nu} \sim Sc^{-1/2} . \tag{C.12}$$

The associated time τ_D required for diffusion to reach the Batchelor scale can then be related to the Kolmogorov time as

$$\frac{\tau_D}{\tau_\nu} \sim \text{constant} , \tag{C.13}$$

and from equation (C.6) can be related to the large scale time τ_M as

$$\frac{\tau_D}{\tau_M} \sim Re^{-1/2} . \tag{C.14}$$

C.4 The Chemical Reaction Time

The time scale on which chemical reaction occurs can be expressed as

$$\tau_r \sim \frac{1}{k} , \tag{C.15}$$

where k is the reaction rate constant.

For the acid - base neutralization reaction used in these measurements, Koochesfahani (1984) quotes reaction rates for the combination of H^+ and OH^- ions given by Laidler & Meiser (1982) and Gutman et al (1983) in the range 10^{10} to 10^{11} $(M \cdot sec)^{-1}$. With the concentration of the weaker reactant (H_2SO_4) in these experiments typically around 10^{-2} M, this gives

$$\tau_r \approx 2 - 20 \quad \text{nsec} . \tag{C.16}$$

C.5 Dimensionless Time Scales

In these experiments, with d_o of order 10^{-3} m and Reynolds numbers of order 10^4 in water, equation (C.4) gives characteristic large scale times of the order of

$$\tau_M \approx 10^{-1} \text{ to } 10^1 \text{ sec} , \tag{C.17}$$

for χ over the range from 30 to 300. The corresponding strain-limited diffusion times are of the order of

$$\tau_D \approx 10^{-5/2} \text{ to } 10^{-1} \text{ sec} . \tag{C.18}$$

From equation (C.17), the reaction time is of the order of

$$\tau_r \approx 10^{-8} \text{ sec.} \qquad (C.19)$$

As a result, the ratio of the molecular mixing time to the large scale time in these experiments is in the range

$$\frac{\tau_D}{\tau_M} \approx 10^{-3/2} \text{ to } 10^{-2} , \qquad (C.20)$$

indicating that molecular diffusion is fast relative to turbulent mixing. Similarly, the ratio of the chemical reaction time to the faster mixing time, τ_D, is in the range

$$\frac{\tau_r}{\tau_D} \approx 10^{-5/2} \text{ to } 10^{-7} , \qquad (C.21)$$

indicating that these reactions may be viewed in the limit of fast chemistry.

APPENDIX D

THE PHOTODIODE ARRAY AND DATA ACQUISITION SYSTEM

The RL1024G solid-state linear image array is commercially available from the Reticon Corporation. When used in conjunction with the RC100B/106 integrating sample-and-hold circuit, also available from Reticon, the only required inputs are a pair of -15 V and +5 V DC sources, together with a single-phase TTL clock signal. The output is a single video signal train consisting of the serial output from each consecutive array element, along with a synchronization pulse, which can be connected to a laboratory data acquisition system.

D.1 The Photodiode Array and Associated Electronics

The RL1024G image array, shown in figure D-1, is a self-scanning array of 1024 photodiodes, configured linearly on 25 μm centers with a 26 μm aperture width, arranged on a 22-pin standard dual-in-line integrated circuit package with an optical quality glass window.

Conceptually, each sensing element is a diffused p-n junction silicon photodiode in parallel with a storage capacitor, to which there is associated a dummy diode also with a storage capacitor. A small charge is placed on the capacitor corresponding to each of the diodes via an integrated digital shift register circuit, operating at the clock frequency, that serially closes a MOS multiplex switch associated with each diode and ties the corresponding capacitor to a recharge line. Light incident on the photodiode produces a photocurrent that gradually removes the charge stored on its associated capacitance. The multiplex switches then serially reconnect the individual photodiode capacitances to the recharge line, with the charge replenished on each capacitor being proportional to the photocurrent integrated over the time between successive recharges. Replenishing each photodiode capacitance differentially with its associated dummy diode capacitance provides cancellation of multiplex switching transients. The RC100B/106 circuit senses the voltage change as each diode capacitor is replenished, and then samples and holds the video line voltage until the next diode is replenished.

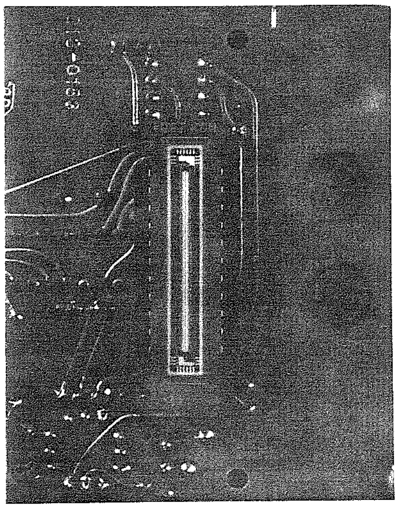

Figure D-1 Photograph of the RL-1024G linear photodiode array.

The diode-to-diode sampling rate is set by the clock frequency driving the shift register scanning circuit. In this manner, the clocking period offers control over the photocurrent integration time and thus sets the temporal resolution of the measurement.

The dark output signal of the array contains components due to random pixel noise and the small leakage current through the photodiodes. The random pixel noise is not removable through signal processing, but is typically less than 0.1% of the saturation level for the array. The leakage current contribution to the dark noise is also typically 0.1% of the array saturation level at room temperature and at the clock frequencies used in these measurements.

D.2 The Data Acquisition System

The acquisition of fluorescence intensity measurements in these experiments was accomplished with an LSI 11/23 - based laboratory computer data acquisition system that has been in development at GALCIT for several years.

A unique feature of this system is a single channel A/D conversion system capable of performing 8-bit conversions at rates up to 20 MHz (presently re-rated to 10 MHz to accommodate to lower data rates of other components in the system). Features of this A/D board include programmable gain, offset and delay, together with capabilities for real-time front end data processing. The design of this board was begun in 1979 by P.E. Dimotakis and D.B. Lang, and was completed, fabricated and tested in 1982 by D. Kerns.

The A/D system communicates through a synchronous device bus (D-bus) and a D-bus interface/controller with the direct memory access (DMA) interface to a DEC Q-bus, upgraded to handle data rates up to 1.2 MBytes/sec. The designs for the D-bus and D-bus interface/controller, which are capable of 12 MBytes/sec data rates, were also defined by D.B. Lang and P.E. Dimotakis.

The data can be written at rates up to 300 KBytes/sec on a high-speed Winchester disk. The software driving the A/D system and its DMA interface is capable of writing selectively at regular intervals onto the disk.

APPENDIX E

DATA REDUCTION TECHNIQUES

E.1 A/D Converter Calibration

The voltage characteristic for the A/D converter was calibrated immediately prior to each set of measurements by digitizing a sufficient number of cycles of a triangle waveform, having a low frequency relative to the digitization rate and an amplitude spanning the voltage range of the converter, to construct a histogram of the number of digitizations at each occurrence of every digital level. The resulting histogram was used to infer the mean voltage range for each digital level of the A/D converter. Digital data from the converter could subsequently be "re-converted" to voltages and interpreted through an ideal linear voltage characteristic.

E.2 Background Pattern and Noise Subtraction

The pattern of background illumination, as well as the fixed component of the dark noise, were determined from the array output in the absence of any fluorescence signal. This fixed background and noise pattern was subsequently subtracted from the fluorescence intensity measurements.

E.3 Conversion from Fluorescence to Concentration

The fluorescence intensity profiles measured by the array were converted to profiles of concentration following the procedure outlined below.

The intensity of fluorescence measured by the photodiode array, $F(\xi,t)$, was at every point along the beam related to the local instantaneous dye concentration and local beam intensity as

$$F(\xi,t) \;=\; h(\xi) \cdot I[C(\xi,t)]\, P(\xi,t) \;, \qquad (E.1)$$

where ξ is a coordinate along the beam in the direction of propagation. Here, $C(\xi,t)$ is the instantaneous dye concentration profile along the beam, $P(\xi,t)$ is the instantaneous beam power profile, $I[C]$ relates the local intensity of fluorescence to the local beam intensity (see Appendix B.2), and $h(\xi)$ is the transfer function relating the fluorescence intensity to that measured by the photodiode array.

The instantaneous beam intensity profile $P(\xi,t)$ was, in turn, related to the dye concentration profile $C(\xi,t)$ through the attenuation integral

$$P(\xi,t) \;=\; P_0(t)\, \exp\!\left(- \int_0^{\xi} I[C(\lambda,t)]\, d\lambda \right) , \qquad (E.2)$$

where $P_0(t)$ is the beam power at $\xi = 0$. With equation (E.2), the fluorescence intensity profile in equation (E.1) becomes

$$F(\xi,t) \;=\; h(\xi) \cdot I[C(\xi,t)]\, P_0(t)\, \exp\!\left(- \int_0^{\xi} I[C(\lambda,t)]\, d\lambda \right) . \qquad (E.3)$$

The transfer function $h(\xi)$ was determined from a measurement of $F(\xi)$ at a uniform dye concentration C_1 as

$$[\, h(\xi) \,/\, h(\xi^*) \,] \;=\; [\, F(\xi) \,/\, F(\xi^*) \,] \;\exp(\, I[C_1]\,(\xi-\xi^*)\,)\;, \tag{E.4}$$

where ξ^* is an arbitrary reference location. The transfer function $h(\xi)$ represents, therefore, a de facto accounting of the collective non-idealities in the optical system and the array.

Normalizing each instantaneous measured fluorescence intensity profile by its value at ξ^*, where the dye concentration was at a constant reference value C^*, gave the profile $I[C(\xi,t)]$ relative to this reference as

$$\frac{I[C(\xi,t)]}{I[C^*]} \;=\; \frac{[F(\xi,t) \,/\, F(\xi^*,t)]}{[h(\xi) \,/\, h(\xi^*)]} \;\exp \int_{\xi^*}^{\xi} I[C(\lambda,t)]\, d\lambda\;. \tag{E.5}$$

The dye concentration profile could be determined from $I[C(\xi,t)]$ in equation (E.5) as

$$C(\xi,t) \;=\; I^{-1}[\; I[C(\xi,t)] \;]\;. \tag{E.6}$$

Denoting the known concentration of dye issuing from the jet exit as C_o allowed the instantaneous jet fluid concentration profile, $c(\xi,t)$, to be determined from equation (E.6) as

$$c(\xi,t) \;=\; \frac{C(\xi,t)}{C_o}\;. \tag{E.7}$$

As shown in figure B-2, for sufficiently weak dye concentrations, I[C] was linearly related to the dye concentration as

$$I[C] \;=\; \zeta \cdot C \,, \tag{E.8}$$

in that case giving the jet fluid concentration profile directly from the measured fluorescence intensity profile as

$$c(\xi,t) \;=\; c^* \,\frac{\left[F(\xi,t)\,/\,F(\xi^*,t)\right]}{\left[h(\xi)\,/\,h(\xi^*)\right]}\, \exp\left(\zeta\, C_o \int_{\xi^*}^{\xi} c(\lambda,t)\, d\lambda \right) . \tag{E.9}$$

REFERENCES

ANTONIA, R.A., PRABHU, A. and STEPHENSON, S.E. 1975, Conditionally sampled measurements in a heated turbulent jet, J. Fluid Mech., 72, 455.

AVERY, J.F. and FAETH, G.M. 1974, Combustion of a submerged gaseous oxidizer jet in liquid metal, Fifteenth (International) Symposium on Combustion, The Combustion Institute.

BATCHELOR, G.K. 1952, The effect of homogeneous turbulence on material lines and surfaces, Proc. Roy. Soc. A, 213, 349.

BECKER, H.A., HOTTEL, H.C. and WILLIAMS, G.C. 1967, The nozzle-fluid concentration field of the round turbulent jet, J. Fluid Mech., 30, 285.

BECKER, H.A. and MASSARO, T.A. 1968, Vortex evolution in a round jet, J. Fluid Mech., 31, 435.

BECKER, H.A. and LIANG, D. 1978a, Visible lengths of vertical free turbulent diffusion flames, Comb. and Flame, 32, 115.

BECKER, H.A. and YAMAZAKI, S. 1978b, Entrainment, momentum flux and temperature in vertical free turbulent diffusion flames, Comb. and Flame, 33, 123.

BECKER, R.S. 1969, Theory and Interpretation of Fluorescence and Phosphorescence, Wiley Interscience, 85.

BERNAL, L.P. 1981, The coherent structure of turbulent mixing layers: I. Similarity of the primary vortex structure. II. Secondary streamwise vortex structure, Ph.D. Thesis, Caltech.

BIRCH, A.D., BROWN, D.R., DODSON, M.G. and THOMAS, J.R. 1978, The turbulent concentration field of a methane jet, J. Fluid Mech., 88, 431.

BRADSHAW, P., FERRISS, D.H. and JOHNSON, R.F. 1964, Turbulence in the noise-producing region of a circular jet, J. Fluid Mech., 19, 591.

BREIDENTHAL, R.E. 1978, A chemically reacting turbulent mixing layer, Ph.D. Thesis, Caltech.

BROADWELL, J.E. 1982, A model of turbulent diffusion flames and nitric oxide production. Part I., TRW Document No. 38515-6001-UT-00.

BROADWELL, J.E. and BREIDENTHAL, R.E. 1982, A simple model of mixing and chemical reaction in a turbulent shear layer, J. Fluid Mech., 125, 397.

BROWN, A.P.G. 1971, Structure of the round free turbulent propane-air diffusion flame, Ph.D. Thesis, Queen's University, Kingston, Canada.

CHEN, C.J. and RODI, W. 1980, Vertical Turbulent Buoyant Jets: A Review of Experimental Data, Pergamon Press, New York.

CHEVRAY, R. and TUTU, N.K. 1978, Intermittency and preferential transport of heat in a round jet, J. Fluid Mech., 88, 133.

CORRSIN, S. and UBEROI, M.S. 1950, Further experiments on the flow and heat transfer in a heated turbulent jet, NACA Report 988.

CROW, S.C. and CHAMPAGNE, F.H. 1971, Orderly structure in jet turbulence, J. Fluid Mech., 48, 547.

DAHM, W.J.A., DIMOTAKIS, P.E. and BROADWELL, J.E. 1984, Non-premixed turbulent jet flames, AIAA Paper 84-0369.

DAHM, W.J.A. and DIMOTAKIS, P.E. 1985, Measurements of entrainment and mixing in turbulent jets, AIAA Paper 85-0056.

DEWEY, C.F., Jr. 1976, Qualitative and quantitative flow field visualization utilizing laser induced fluorescence, in Proc. AGARD Conf. on Applications of Non-Intrusive Instrumentation in Fluid Flow Research, AGARD-CP-193.

DIBBLE, R.W., KOLLMANN, W. and SCHEFER, R.W. 1984, Conserved scalar fluxes measured in a turbulent nonpremixed flame by combined laser doppler velocimetry and laser Raman scattering, Comb. and Flame, 55, 307.

DIMOTAKIS, P.E. and PAPANTONIOU, D.A. 1981, Investigation of the relation of the structure of turbulence in the near field of a turbulent jet to the noise emitted in the far field, Final Scientific Report, Contract No. Y-481468-0935N, Boeing Commercial Airplane Company.

DIMOTAKIS, P.E., MIAKE-LYE, R.C. and PAPANTONIOU, D.A. 1983a, Structure and dynamics of round turbulent jets, Physics of Fluids, 26, 3185.

DIMOTAKIS, P.E., BROADWELL, J.E. and HOWARD, R.D. 1983b, Chemically reacting turbulent jets, AIAA Paper 83-0474.

DREXHAGE, K.H. 1973, Structure and properties of laser dyes, 144-193 in Dye Lasers, ed. F.P. Schafer, Springer Verlag, New York.

FIEDLER, H.F. 1974, Transport of heat across a plane turbulent mixing layer, Adv. Geophys., 18A, 93.

GUTMAN, M., NACHLIEL, E., GERSHON, E., GINGER, R., and PINE, E. 1983, pH Jump : kinetic analysis and determination of the diffusion-controlled rate constants, J. Am. Chem. Soc., 108, 2210.

HAWTHORNE, W.R., WEDDELL, D.S. and HOTTEL, H.C. 1948, Mixing and combustion in turbulent gas jets, Third (International) Symposium on Combustion, The Williams and Wilkins Co.

HOTTEL, H.C. 1953, Burning in laminar and turbulent fuel jets, Fourth (International) Symposium on Combustion, The Williams and Wilkins Co.

KERNEY, P.J., FAETH, G.M. and OLSON, D.R. 1972, Penetration characteristics of a submerged steam jet, AIChE, 18, 548.

KOLLMANN, W. and JANICKA, J. 1982, The probability density function of a passive scalar in turbulent shear flows, Physics of Fluids, 25, 1755.

KONRAD, J.H. 1976, An experimental investigation of mixing in two-dimensional turbulent shear flows with application to diffusion-limited chemical reactions, Ph. D. Thesis, Caltech; also Project SQUID Technical Report CIT-8-PU.

KOOCHESFAHANI, M.M. 1984, Experiments on turbulent mixing and chemical reactions in a liquid mixing layer, Ph.D. Thesis, Caltech.

KOOCHESFAHANI, M.M. and DIMOTAKIS, P.E. 1984, Laser induced fluorescence measurements of concentration in a plane mixing layer, AIAA Paper 84-0198.

LAIDLER, K.J., and MEISER, J.H. 1982, Physical Chemistry, The Benjamin/Cummings Publishing Co., Inc., 392.

LOCKWOOD, F.C. and MONEIB, H.A. 1980, Fluctuating temperature measurements in a heated round jet, Comb. Sci. Tech., 22, 3.

LUI, H.T., LIN, J.T., DELISI, D.P. and ROBBEN, F.A. 1977, Application of a fluorescence technique to dye-concentration measurements in a turbulent jet, NBS Special Publication 484, in Proc. Symp. on Flow in Open Channels and Closed Conduits.

MOLLO-CHRISTENSEN, E. 1967, Jet noise and shear flow instability seen from an experimenter's viewpoint, J. Appl. Mech., 89, 1.

MUNGAL, M.G. 1983, Experiments on mixing and combustion with low heat release in a turbulent shear flow, Ph.D. Thesis, Caltech.

NAKAMURA, I, SAKAI, Y. and MIYATA, M. 1982, A study on the fluctuation concentration field in a turbulent jet, Nagoya Univ. Reports, 34, 113.

POPE, S.B. 1980, Probability distributions of scalars in turbulent shear flow, 7-16, in Turbulent Shear Flows II, ed. Bradbury et al, Springer Verlag, New York.

POPE, S.B. 1985, Calculations of a plane turbulent jet, AIAA Journal, 22, 896.

RICOU, F.P. and SPALDING, D.B. 1961, Measurements of entrainment by axisymmetrical turbulent jets, J. Fluid Mech., 11, 21.

ROBBEN, F.A., LIN, J.T., DELISI, D.P. and LIU, H.T. 1976, Feasibility study of a dye-fluorescence technique for measuring concentrations in fluids, Flow Research Note No. 91, Flow Research Inc.

THRING, M.W. and NEWBY, M.P. 1952, Combustion length of enclosed turbulent jet flames, 4th (International) Symposium on Combustion , The Williams and Wilkins Co.

TSO, J., KOVASZNAY, L.S.G. and HUSSAIN, A.K.M.F. 1981, Search for large-scale coherent structure in the nearly self-preserving region of a turbulent axisymmetric jet, Transactions of the ASME, J. Fluids Engr., 103, 503.

TYSON, T.J., KAU, C.J. and BROADWELL, J.E. 1982, A model of turbulent diffusion flames and nitric oxide production. Part II., TRW Document No. 38515-6001-UT-00.

UBEROI, M.S. and SINGH, P.I. 1975, Turbulent mixing in a two-dimensional jet, Physics of Fluids, 18, 764.

WALKER, B.J. 1979, Turbulence model comparisons for shear layers and axisymmetric jets, U.S. Army Missile Command Technical Report RD-80-1.

WEIMER, J.C., FAETH, G.M. and OLSON, D.R. 1973, Penetration of vapor jets submerged in subcooled liquids, AIChE, 19, 552.

WILSON, R.A.M. and DANCKWERTS, P.V. (1964), Studies in turbulent jet mixing - II. A hot air jet, Chem. Engr. Sci., 19, 885.

WOHL, K., GAZLEY, C. and KAPP, N. 1948, Diffusion flames, Third (International) Symposium on Combustion, The Williams and Wilkins Co.

WYGNANSKI, I. and FIEDLER, H.E. 1969, Some measurements in the self-preserving jet, J. Fluid Mech., 38, 577.

YULE, A.J. 1978, Large scale structure in the mixing layer of a round jet, J. Fluid Mech., 89, 413.

ZUKOSKI, E.E., CETEGEN, B. and KUBOTA, T. 1984, Visible structure of buoyant diffusion flames, Twentieth (International) Symposium on Combustion, The Combustion Institute.

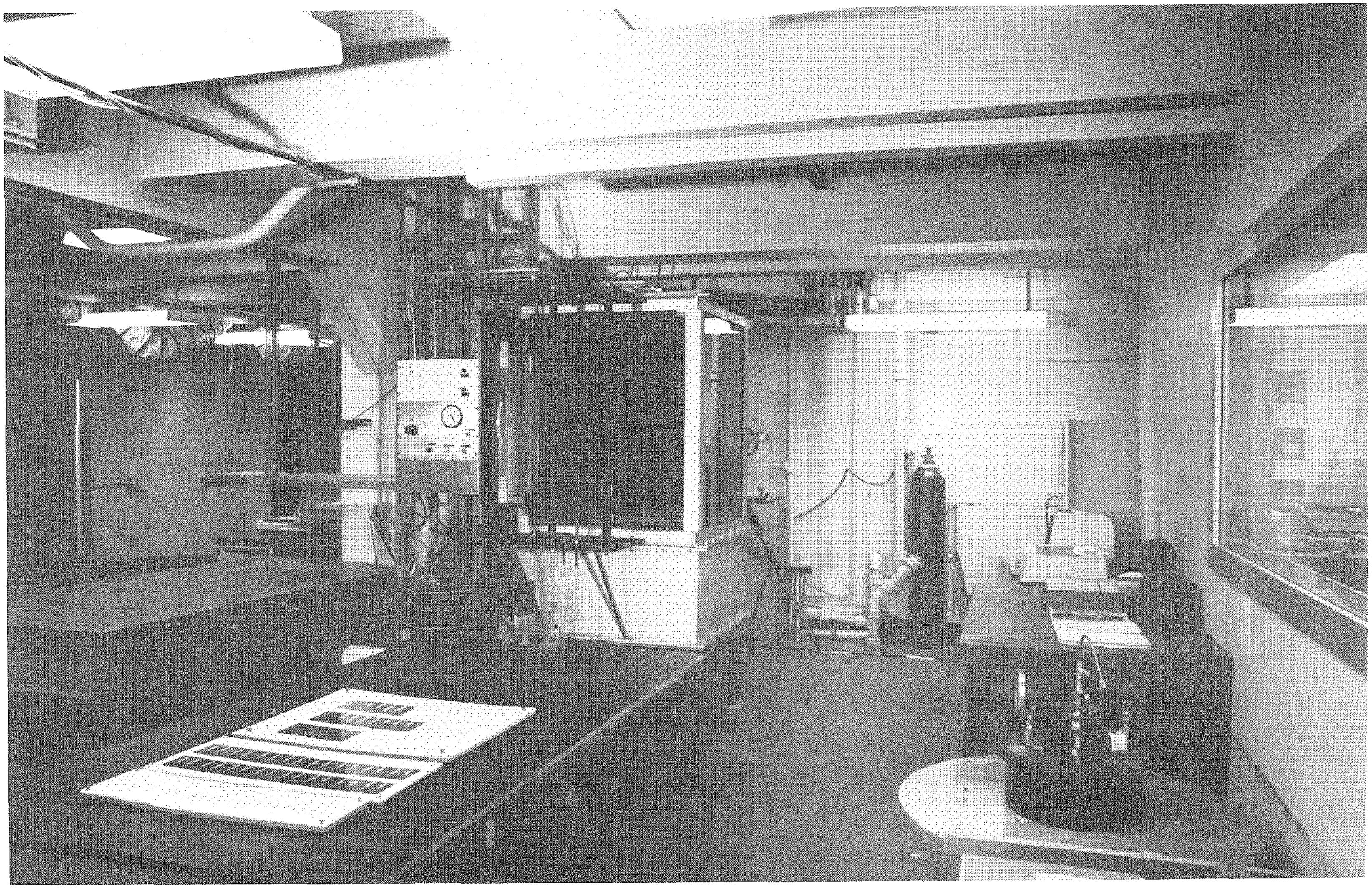

Figure 2-1. Overview of the experimental facility.

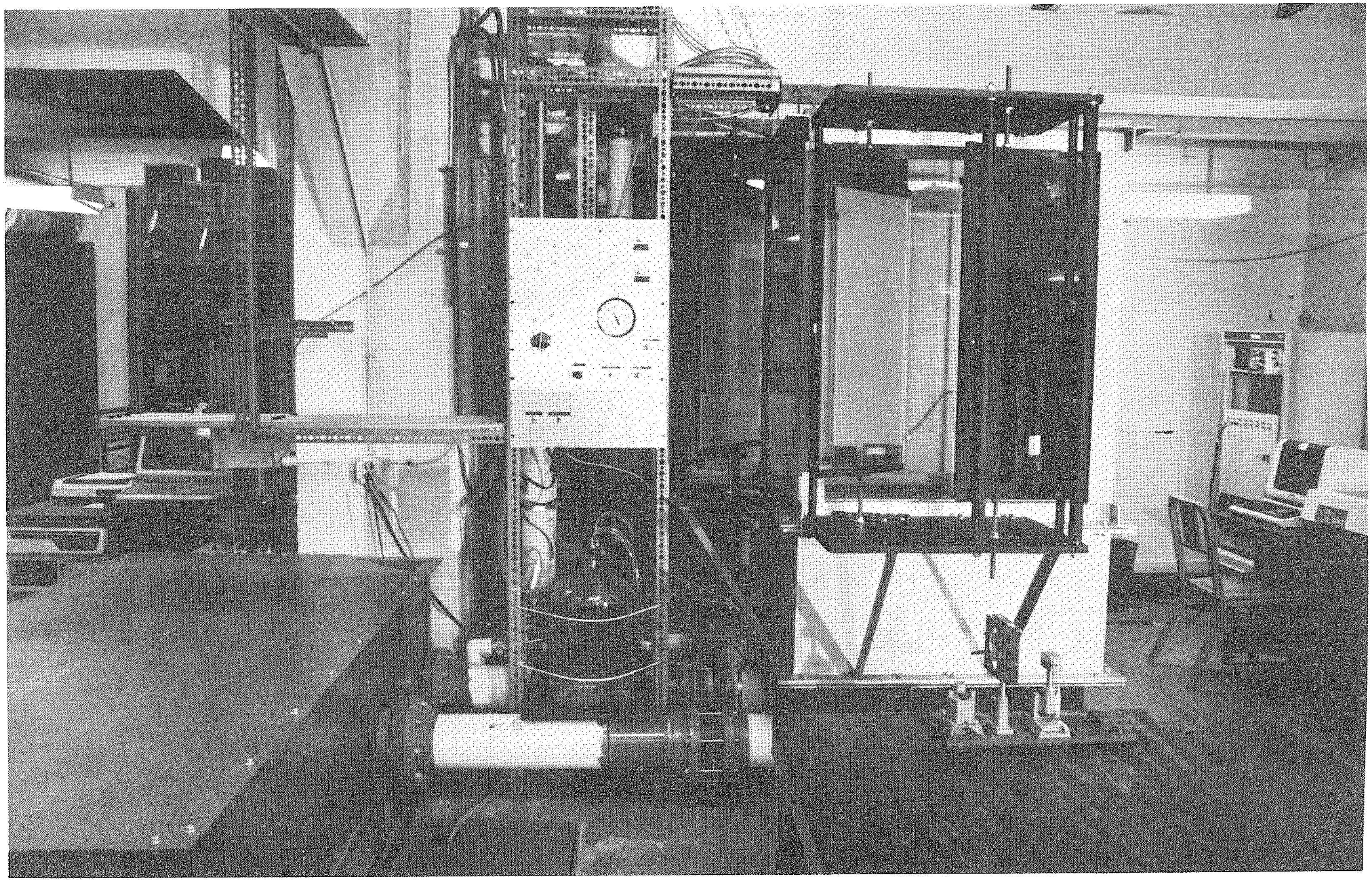

Figure 2-2. Detail view of the experimental facility.

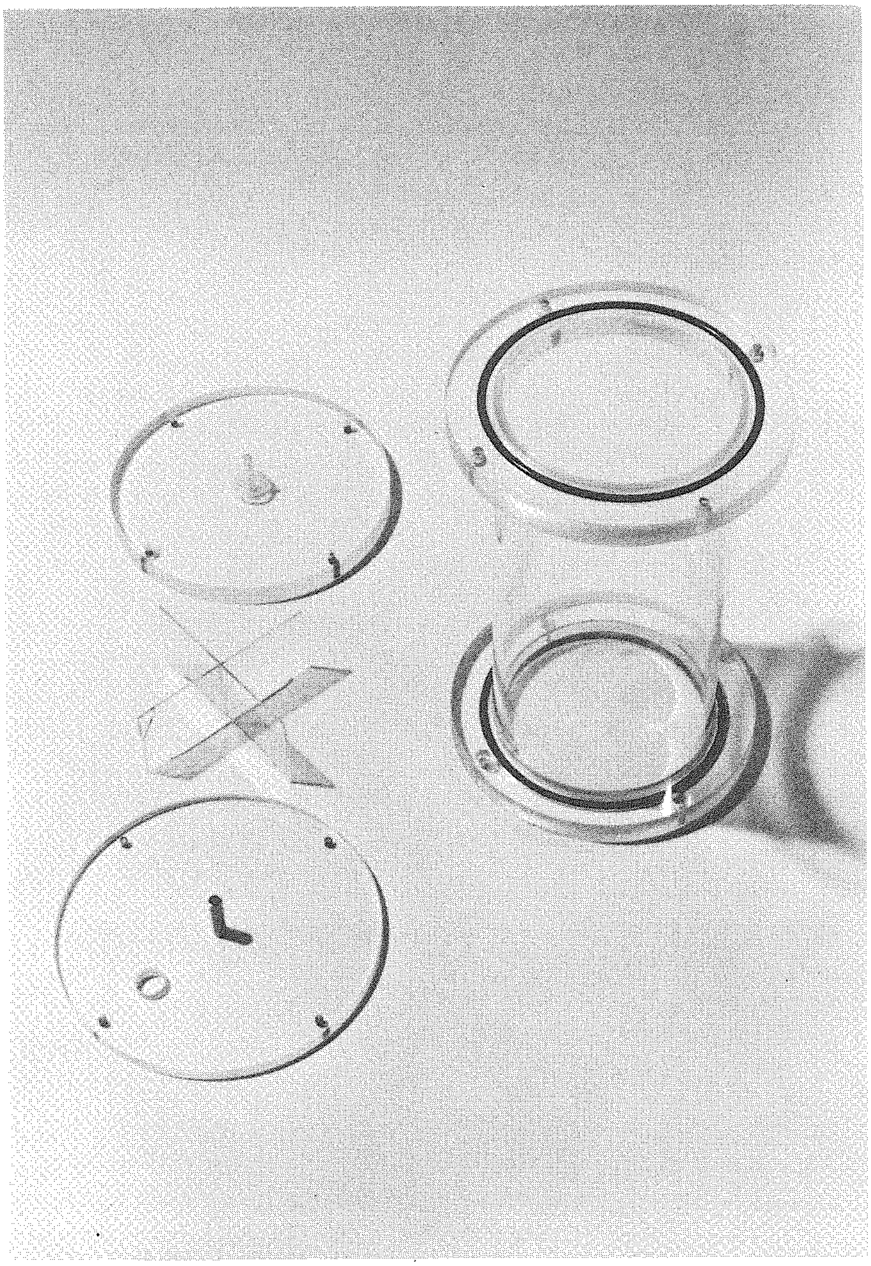

Figure 2-3. Photograph of the jet plenum and nozzle.

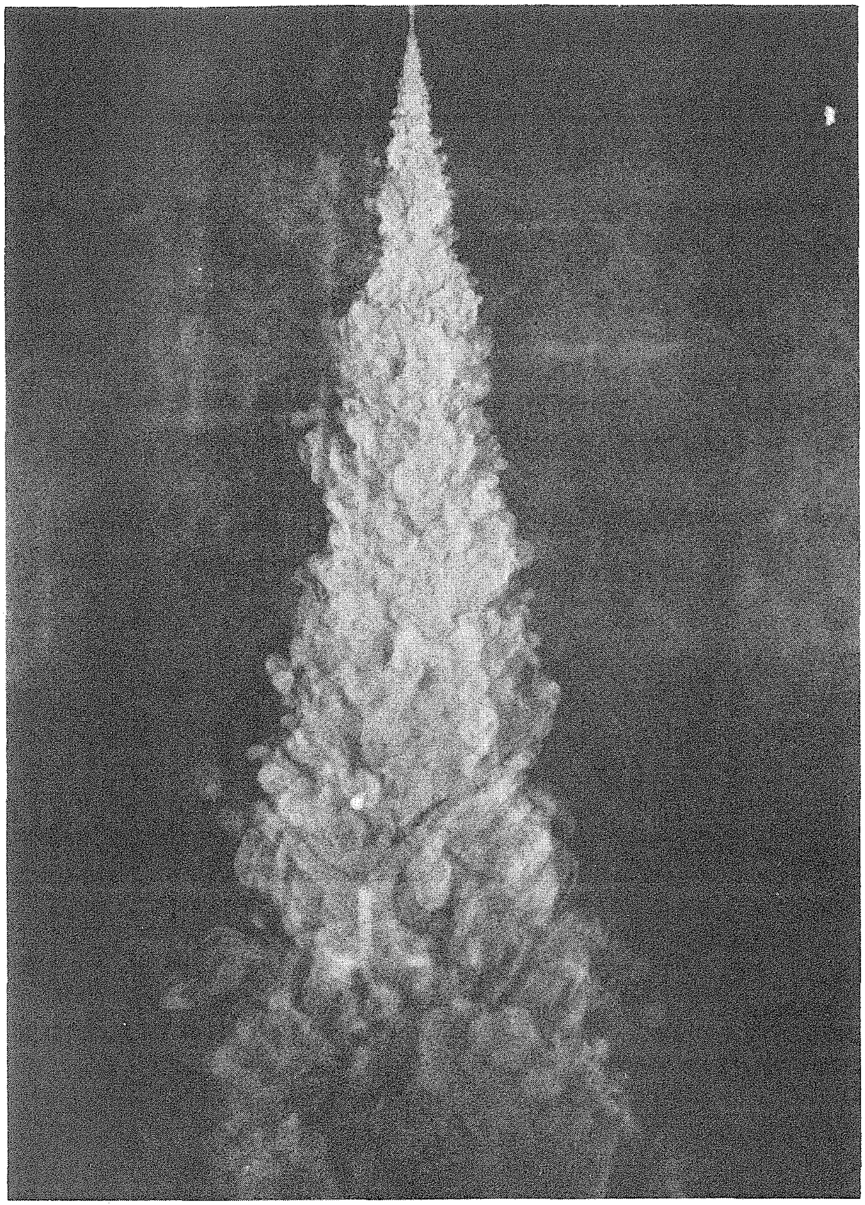

Figure 3-1. Conventional visualization of jet mixing; Re = 5,000 .

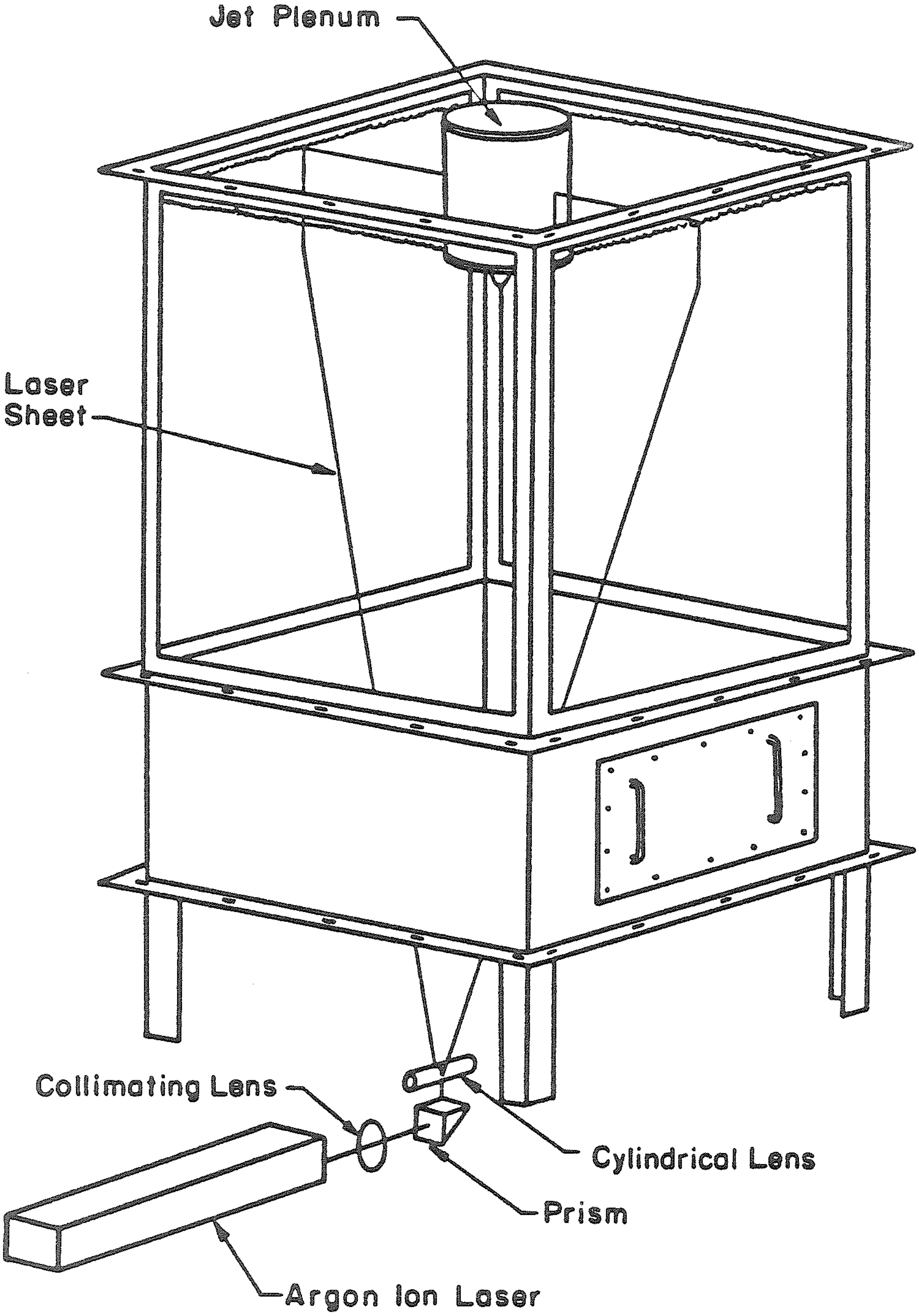

Figure 3-2. Single-sheet planar LIF optical configuration.

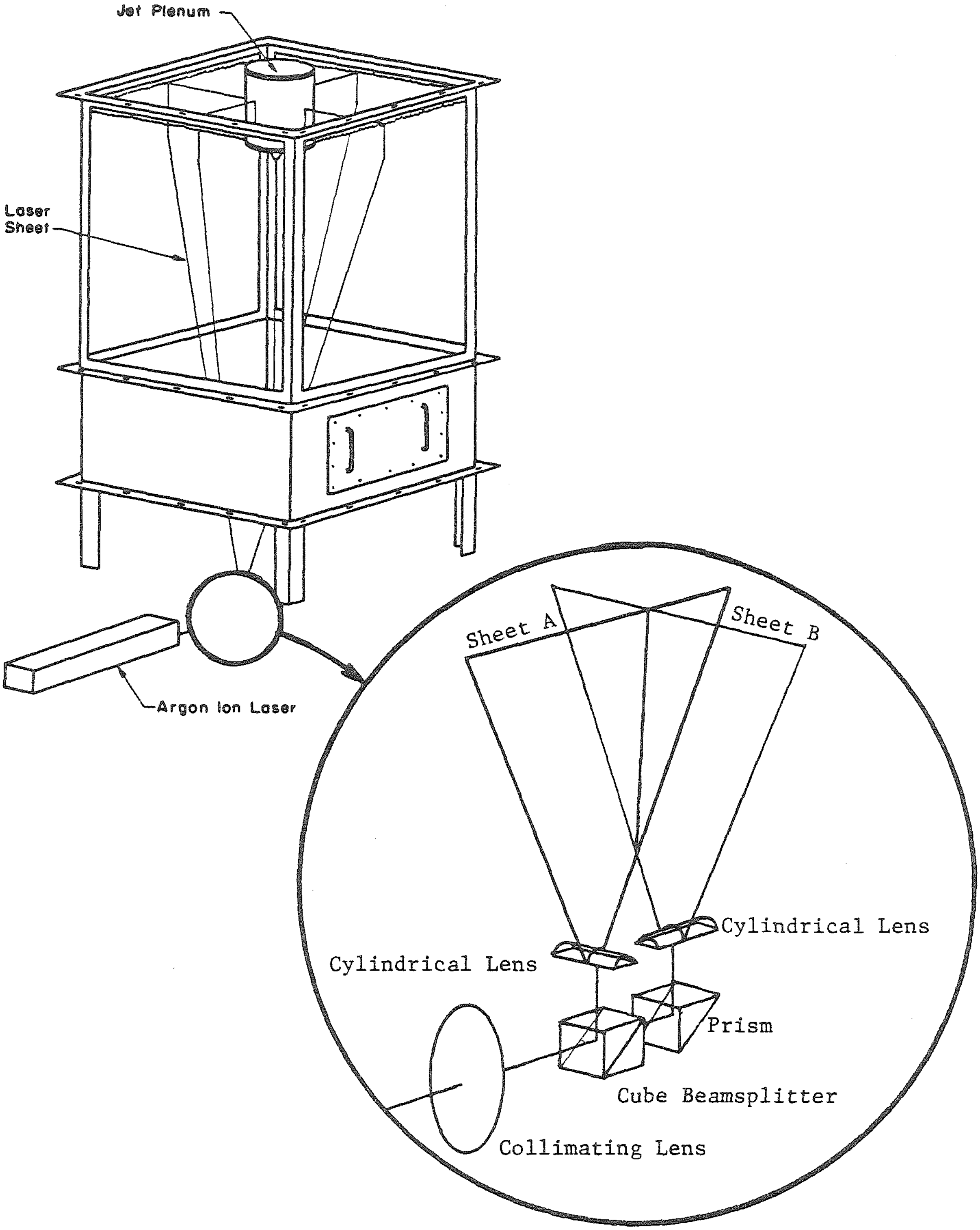

Figure 3-3. Double-sheet planar LIF optical configuration.

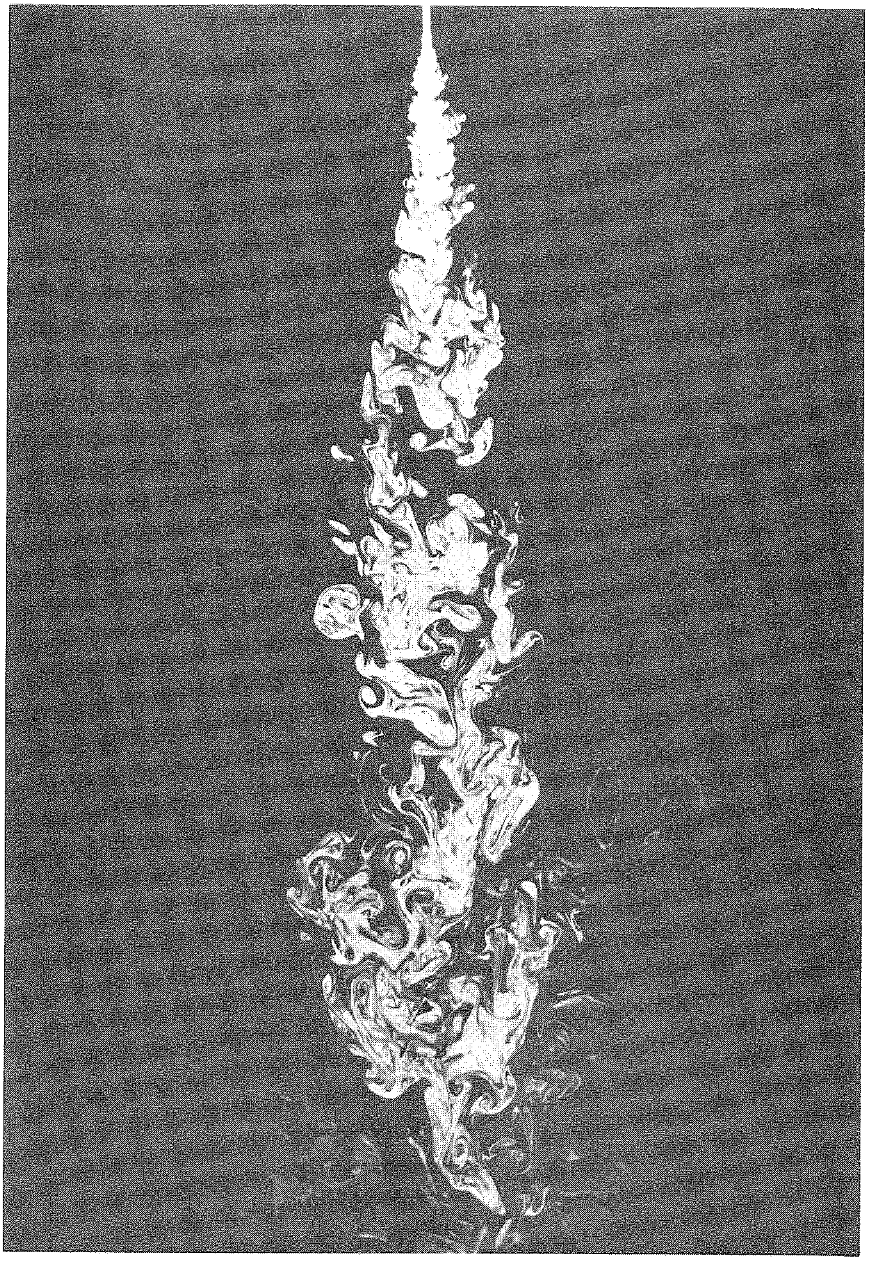

Figure 3-4a. Planar LIF photograph of jet mixing; Re = 1,500 .

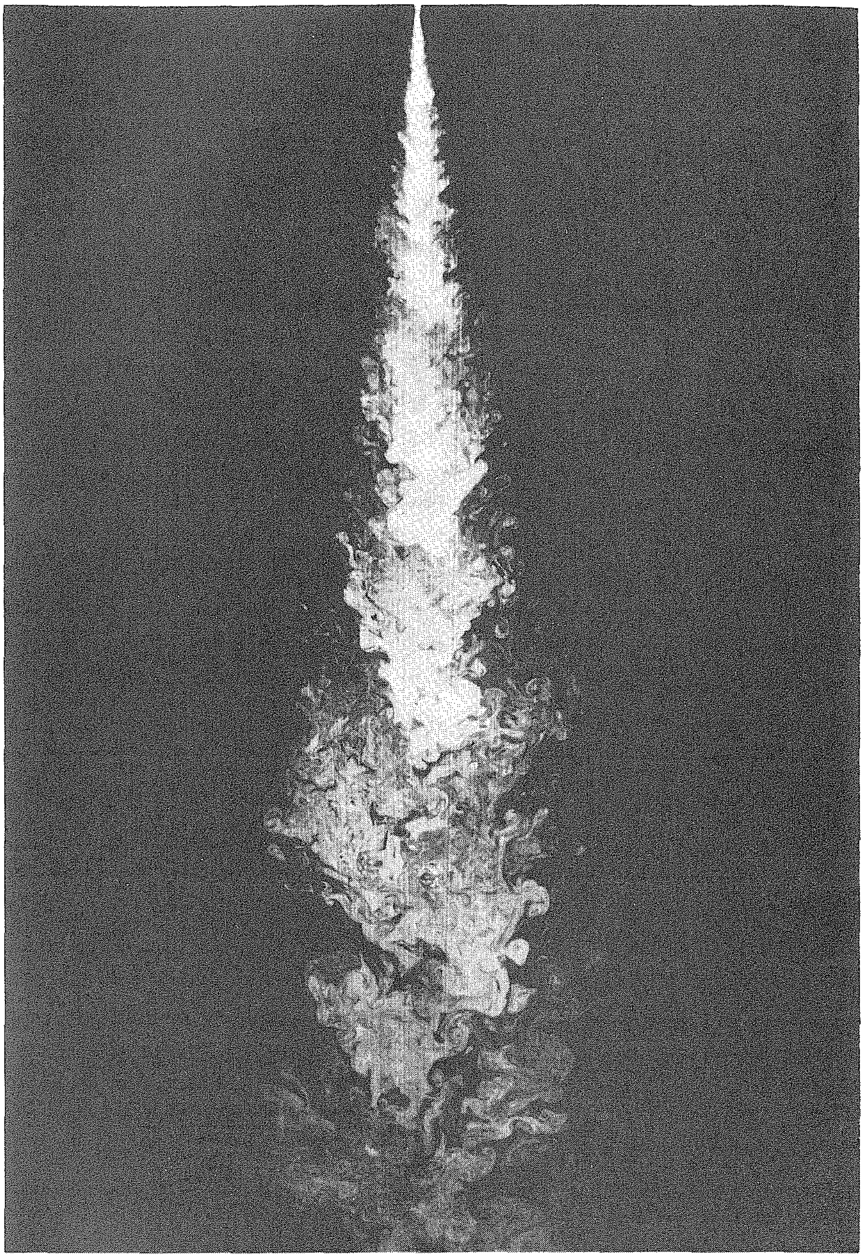

Figure 3-4b. Planar LIF photograph of jet mixing; Re = 5,000 .

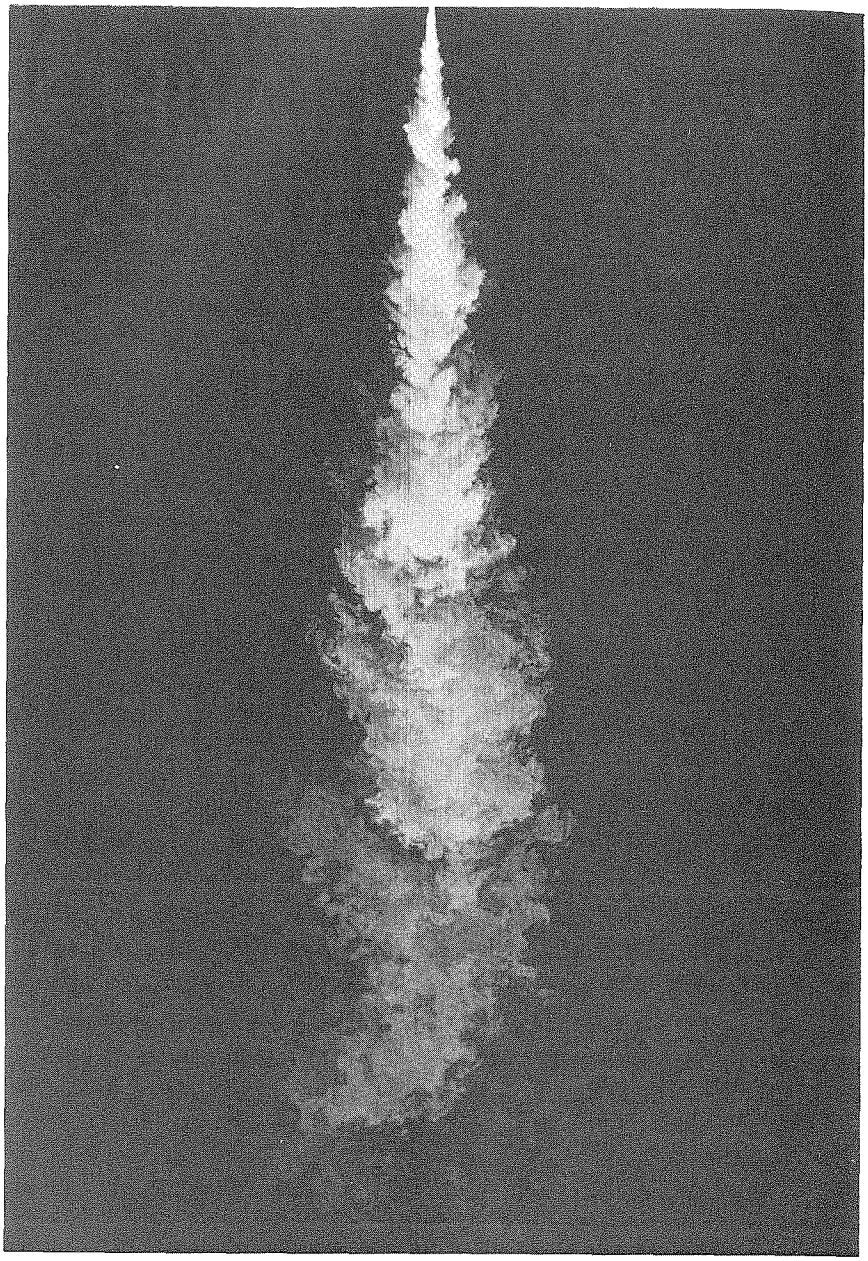

Figure 3-4c. Planar LIF photograph of jet mixing; Re = 20,000 .

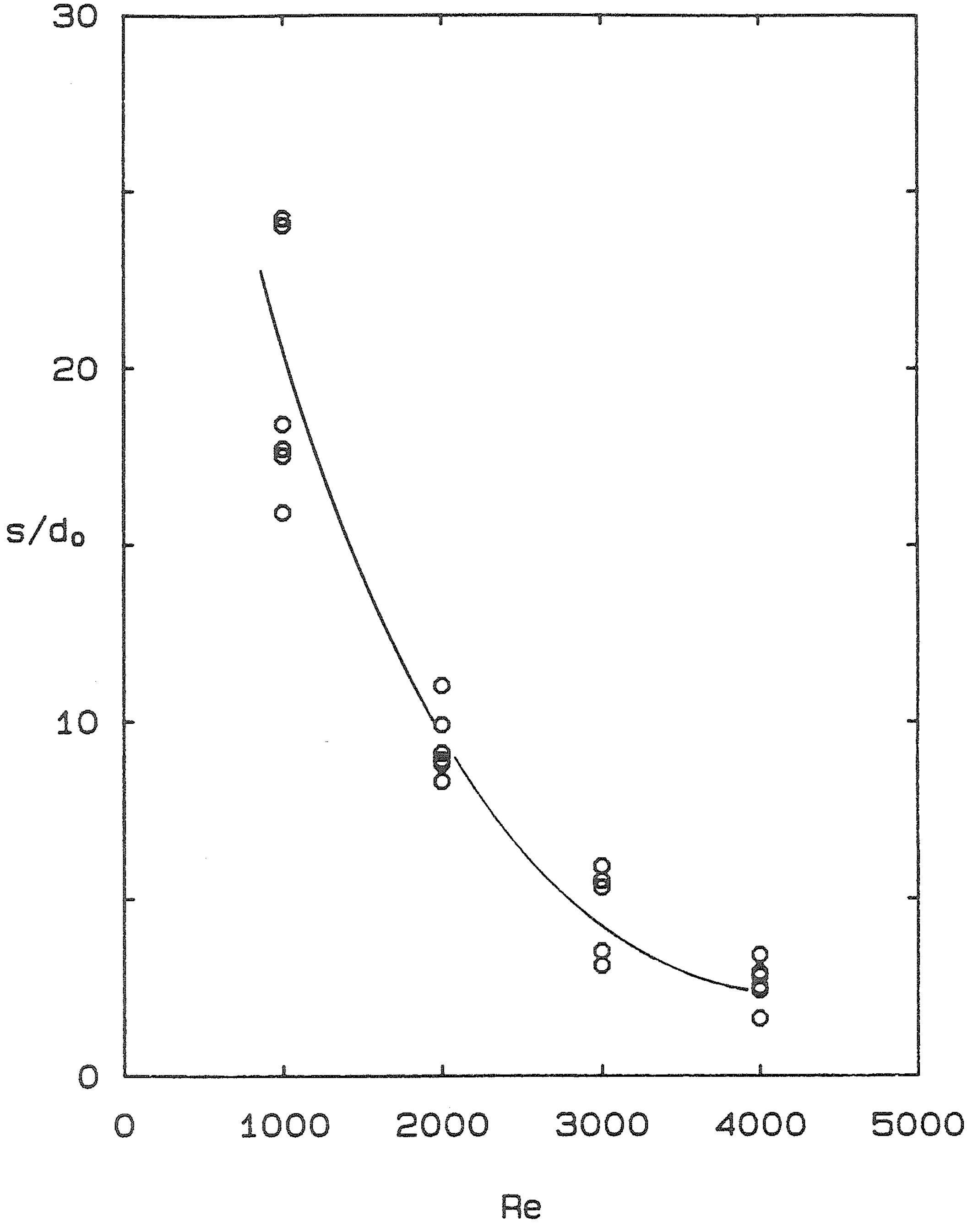

Figure 3-5. Breakpoint length vs. Reynolds number.

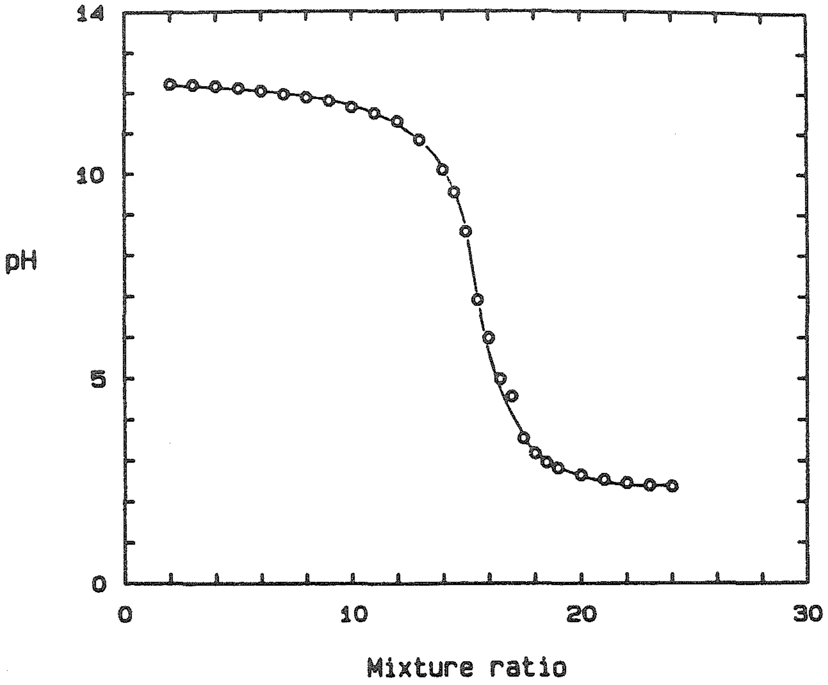

Figure 3-6. Titration curve for typical acid/base reactants.

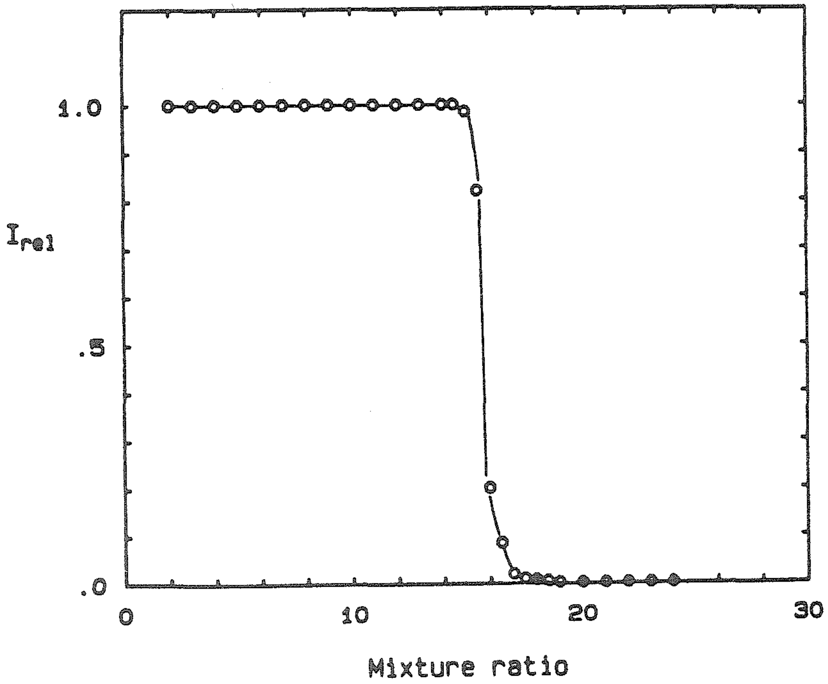

Figure 3-7. Fluorescence intensity vs. mixture ratio from figure 3-6 .

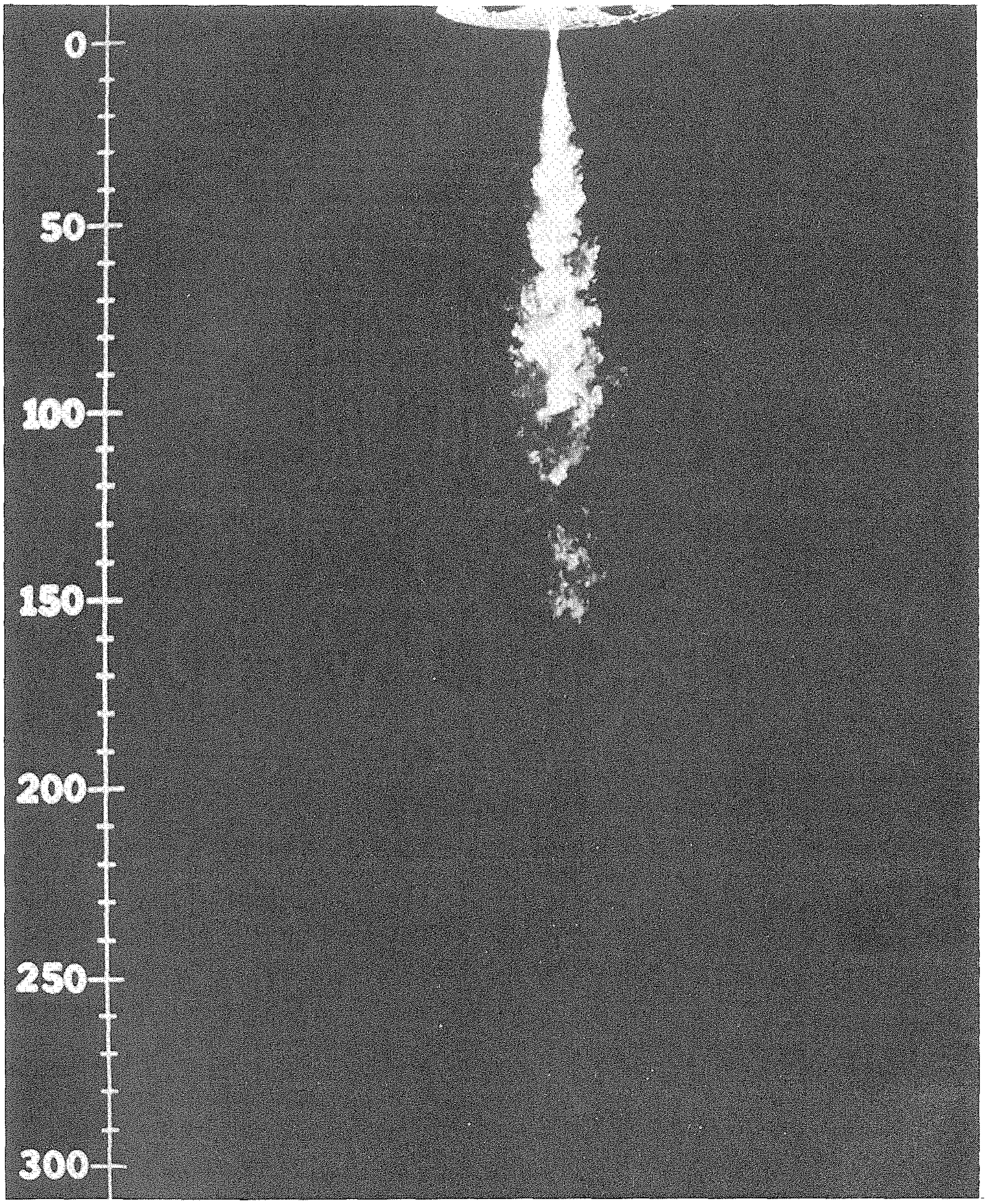

Figure 3-8. Photograph using the chemically sensitive LIF technique; Re = 10,000 , ϕ = 15 .

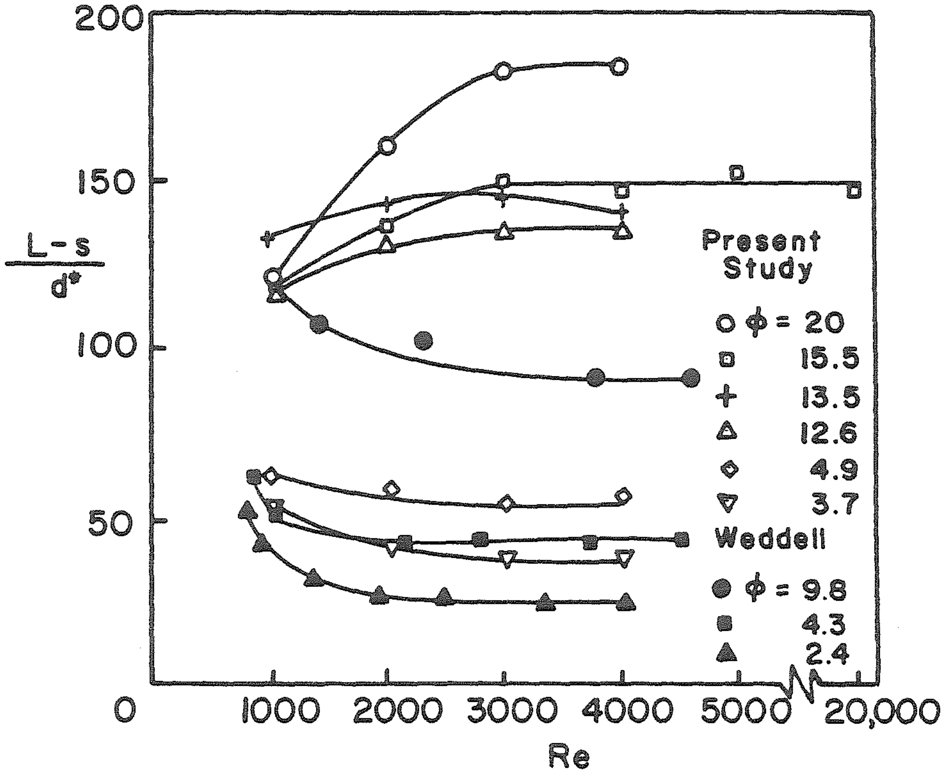

Figure 3-9. Mean flame length vs. Re for various ϕ.

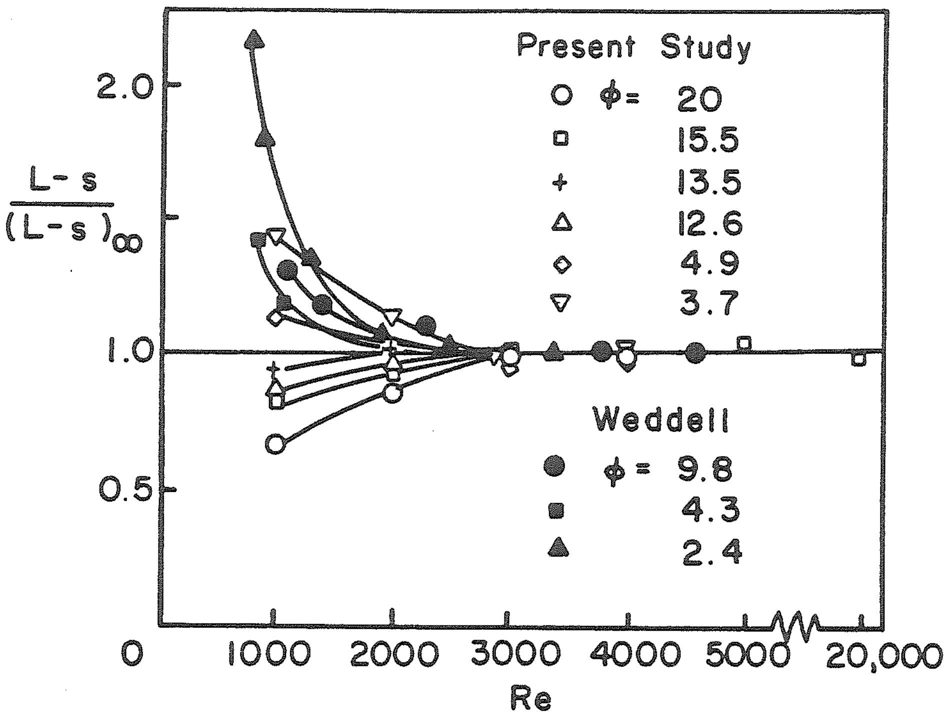

Figure 3-10. Normalized mean flame length vs. Re for various φ.

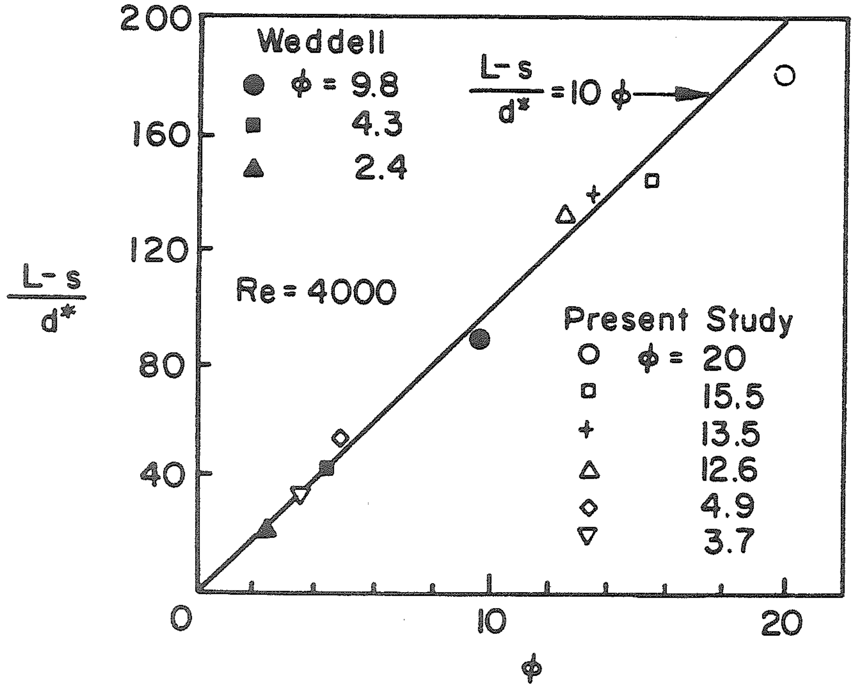

Figure 3-11. Mean flame length vs. φ for Re ≥ 3,000 .

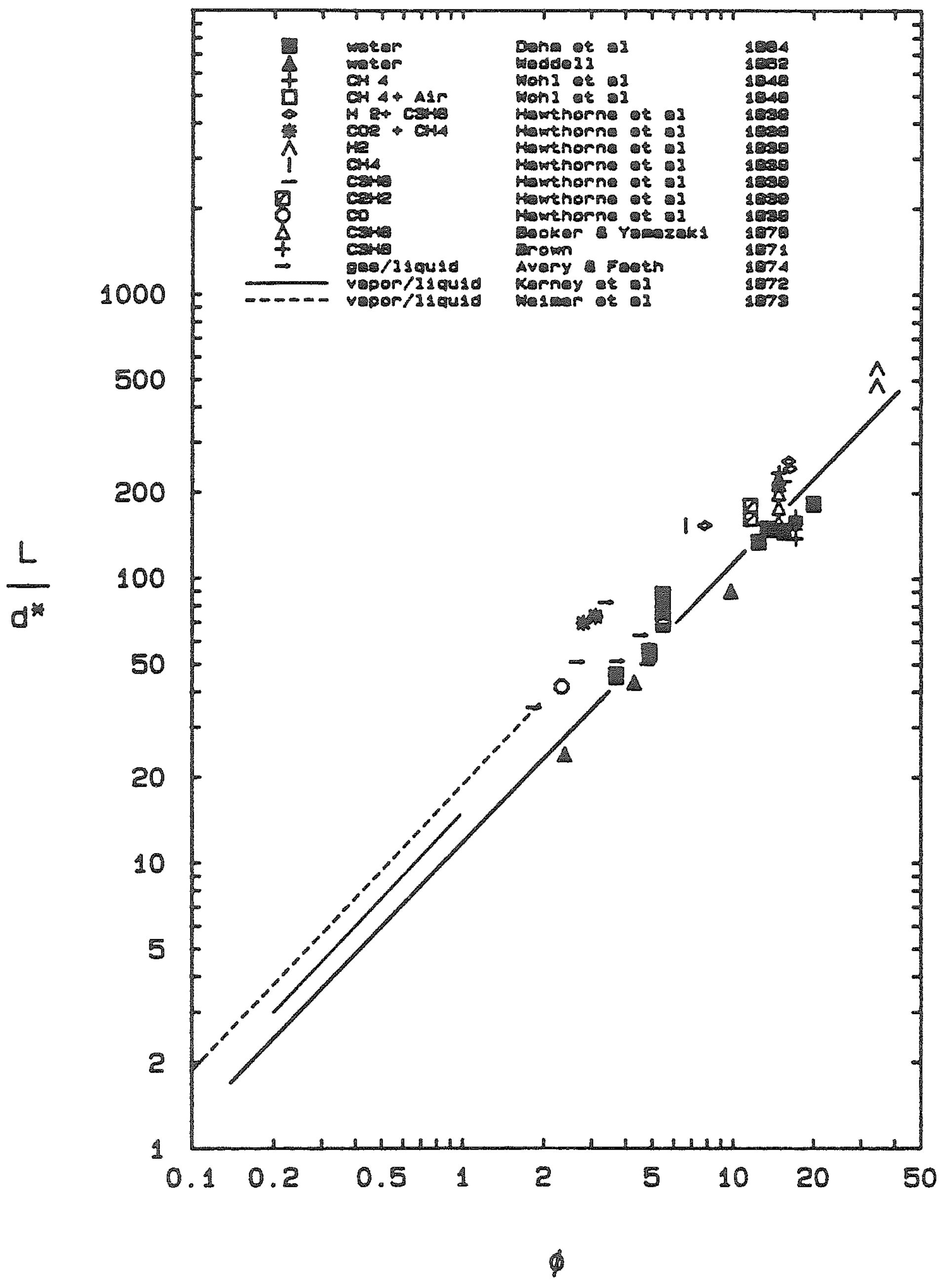

Figure 3-12. Mean flame length vs. ϕ for various reacting jets.

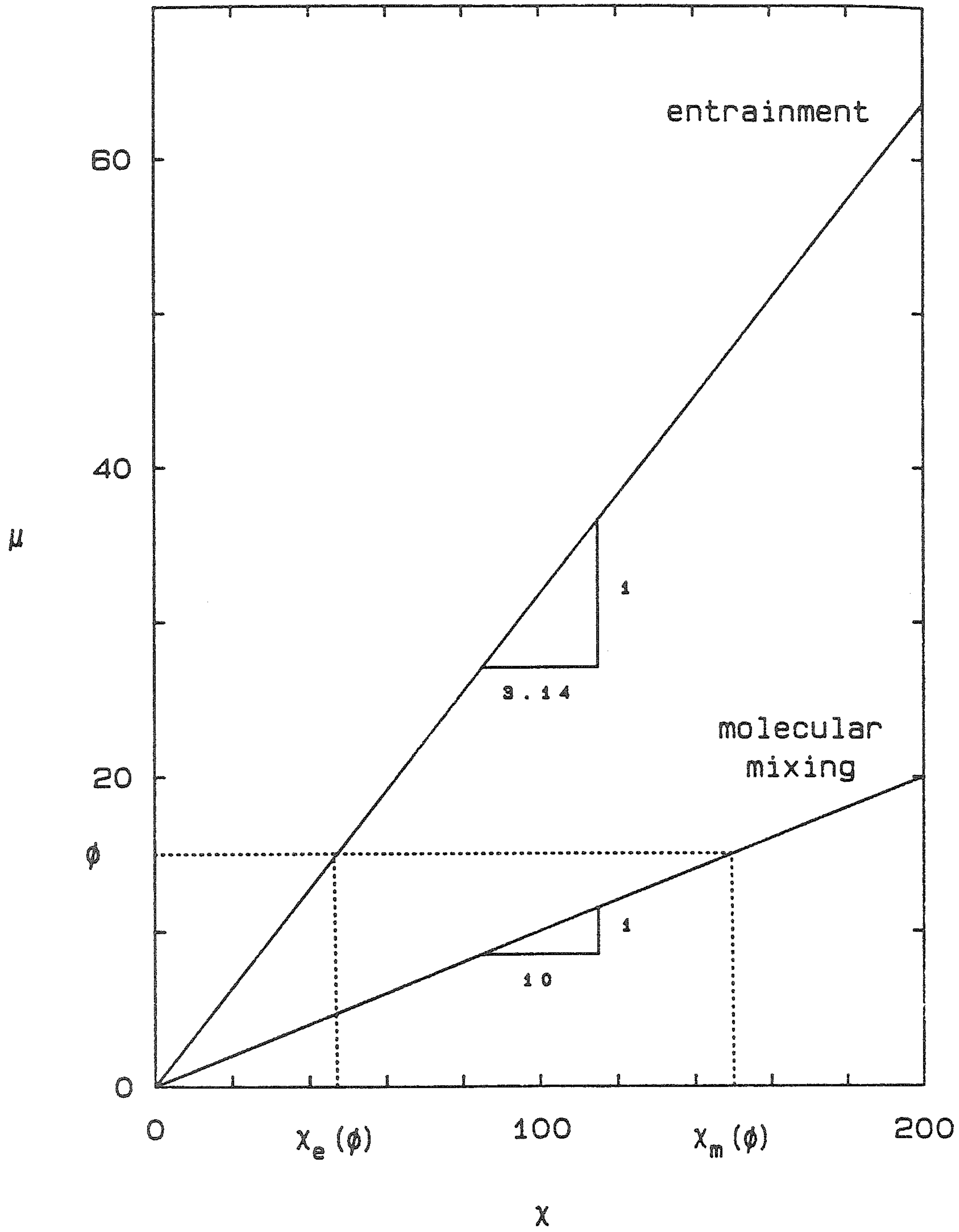

Figure 3-13. $\chi_e(\phi)$ and $\chi_m(\phi)$ vs. ϕ.

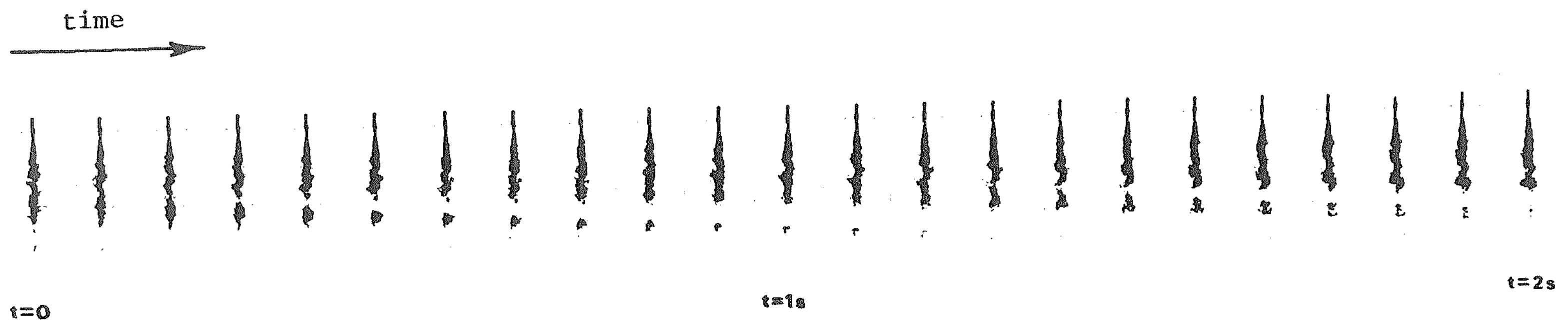

Figure 3-14. Flame length vs. time using single sheet technique, showing flame length fluctuations; $Re = 10,000$, $\phi = 15$.

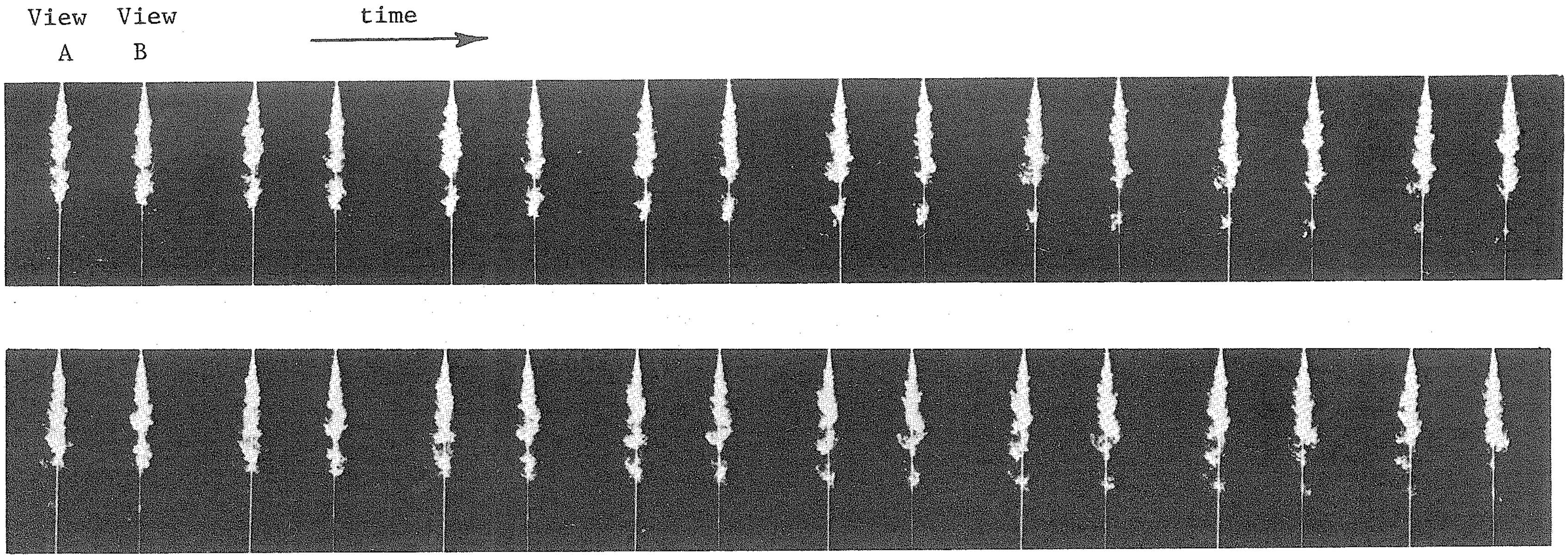

Figure 3-15. Flame length vs. time using double sheet technique, showing flame length fluctuations; Re = 10,000 , $\phi = 15$.

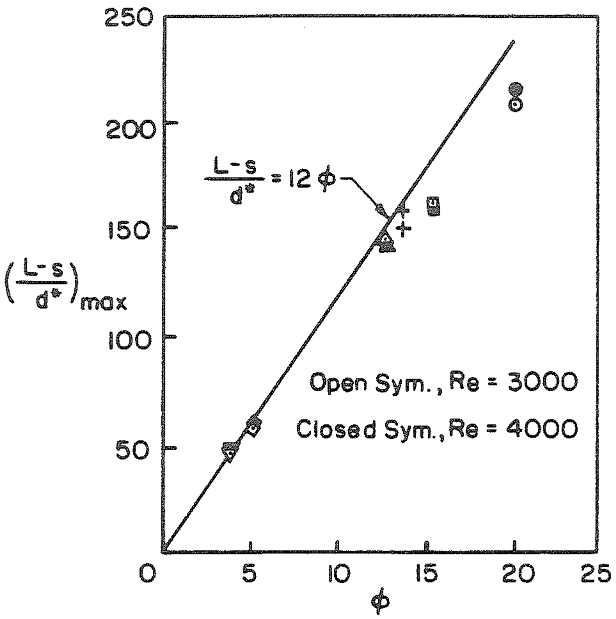

a. Maximum

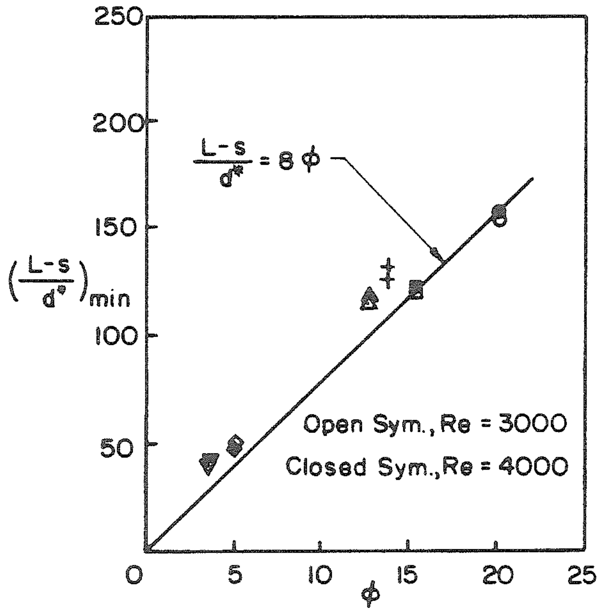

b. Minimum

Figure 3-16. Maximum and minimum flame length vs. ϕ for $Re \geq 3{,}000$.

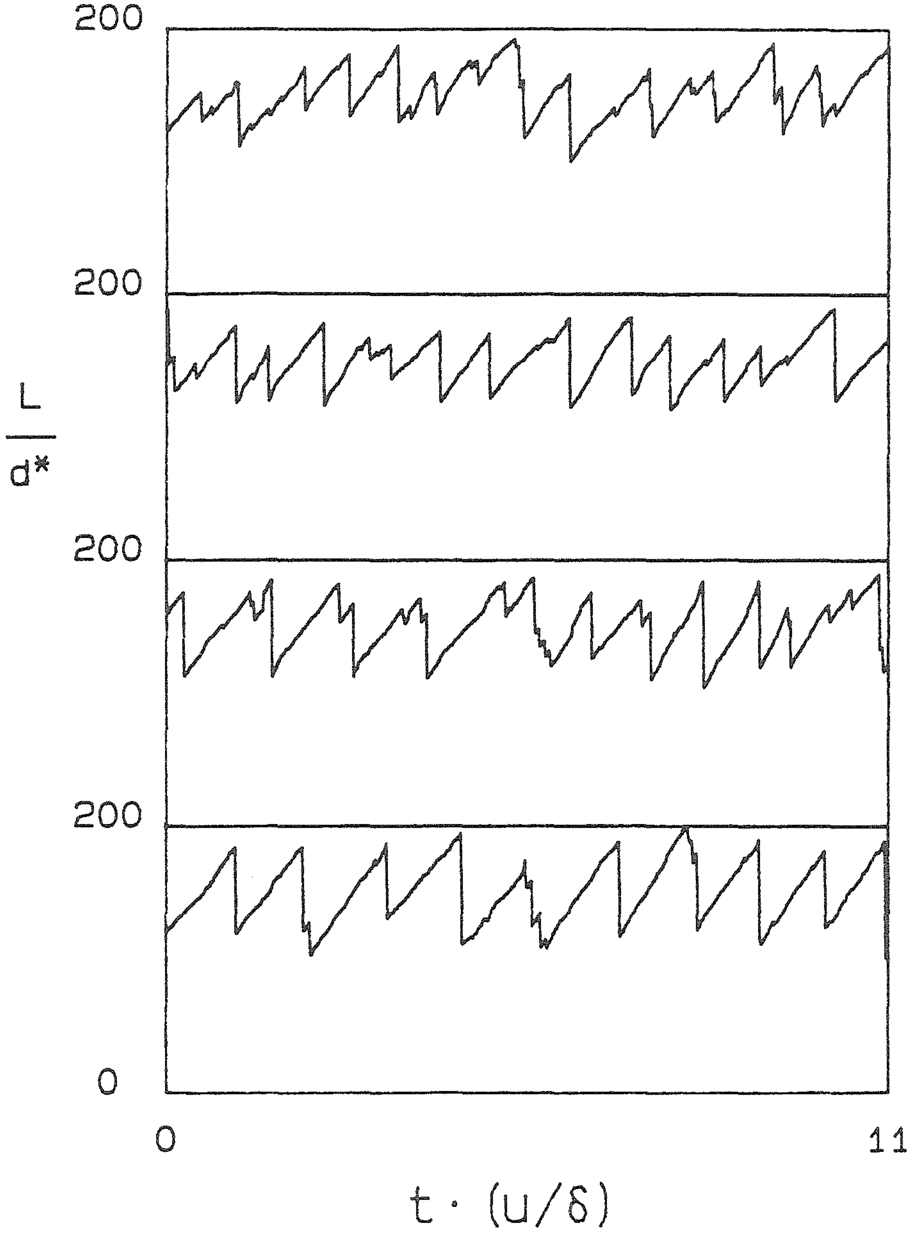

Figure 3-17. Flame length vs. time; Re = 10,000 , $\phi = 15$.

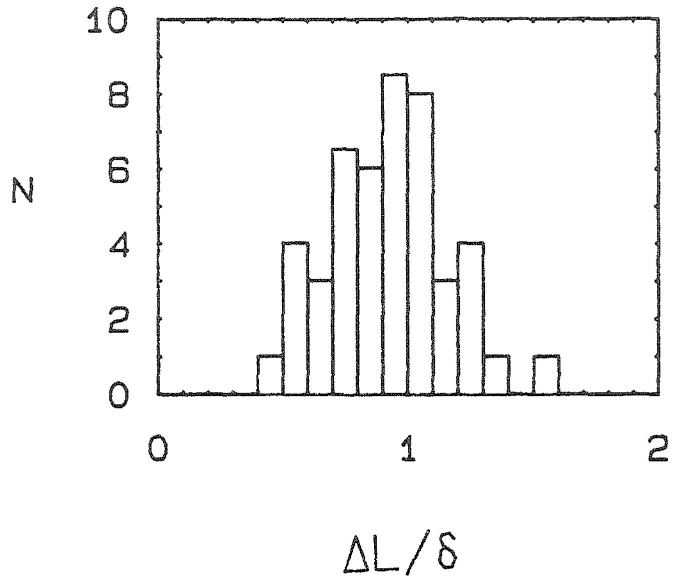

a. Length scaling

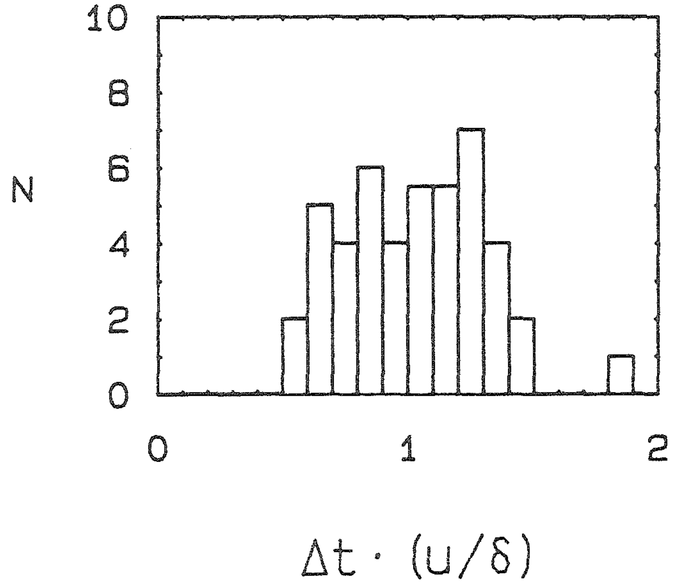

b. Time scaling

Figure 3-18. Histograms from flame length fluctuations in figure 3-17 .

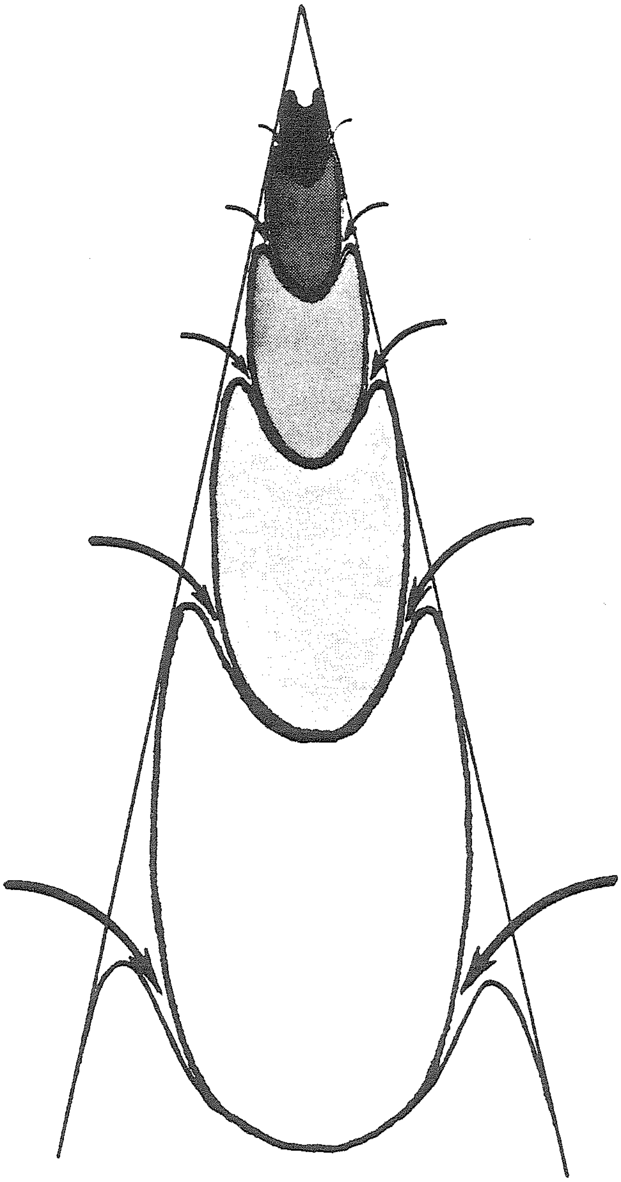

Figure 3-19. Idealized conceptual picture of organized entrainment and mixing in the far field of turbulent jets.

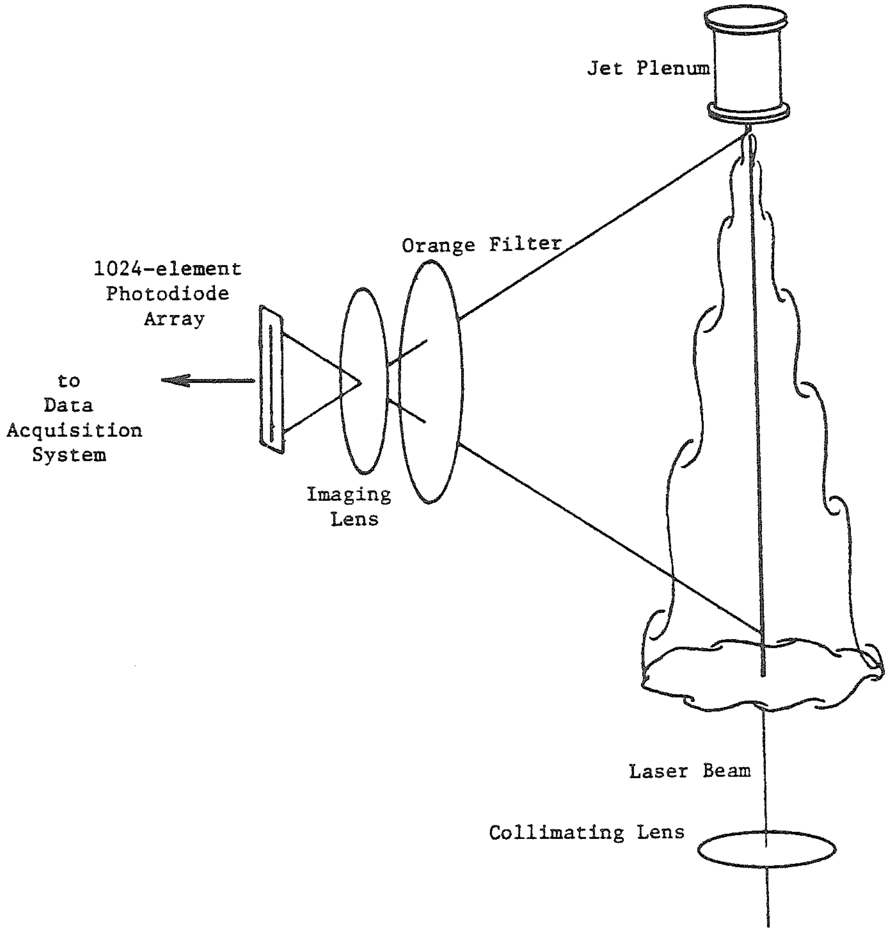

Figure 4-1. Schematic of axial imaging configuration.

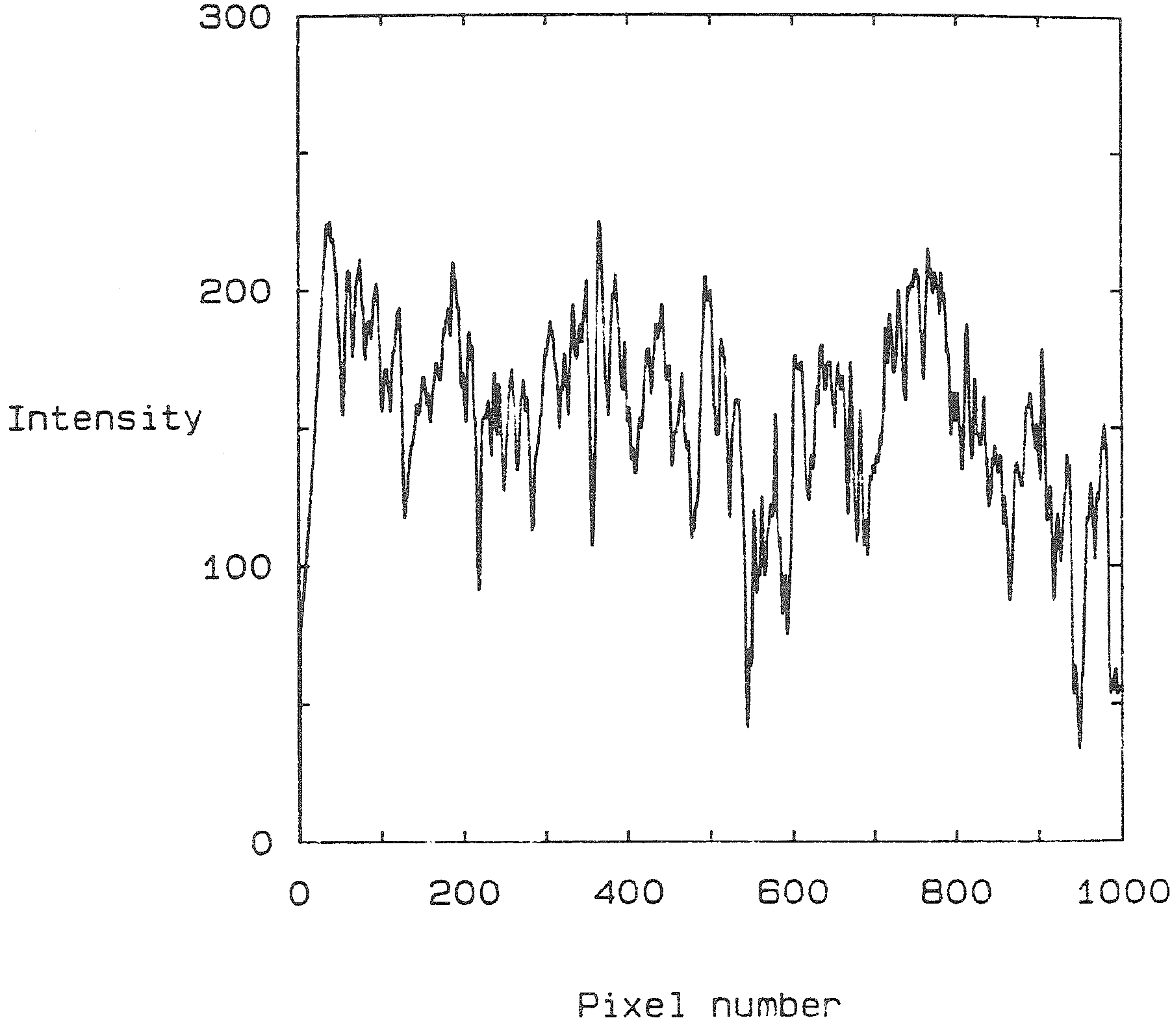

Figure 4-2. Typical centerline fluorescence intensity profile; $0 \leq \chi \leq 300$, $Re = 5{,}000$.

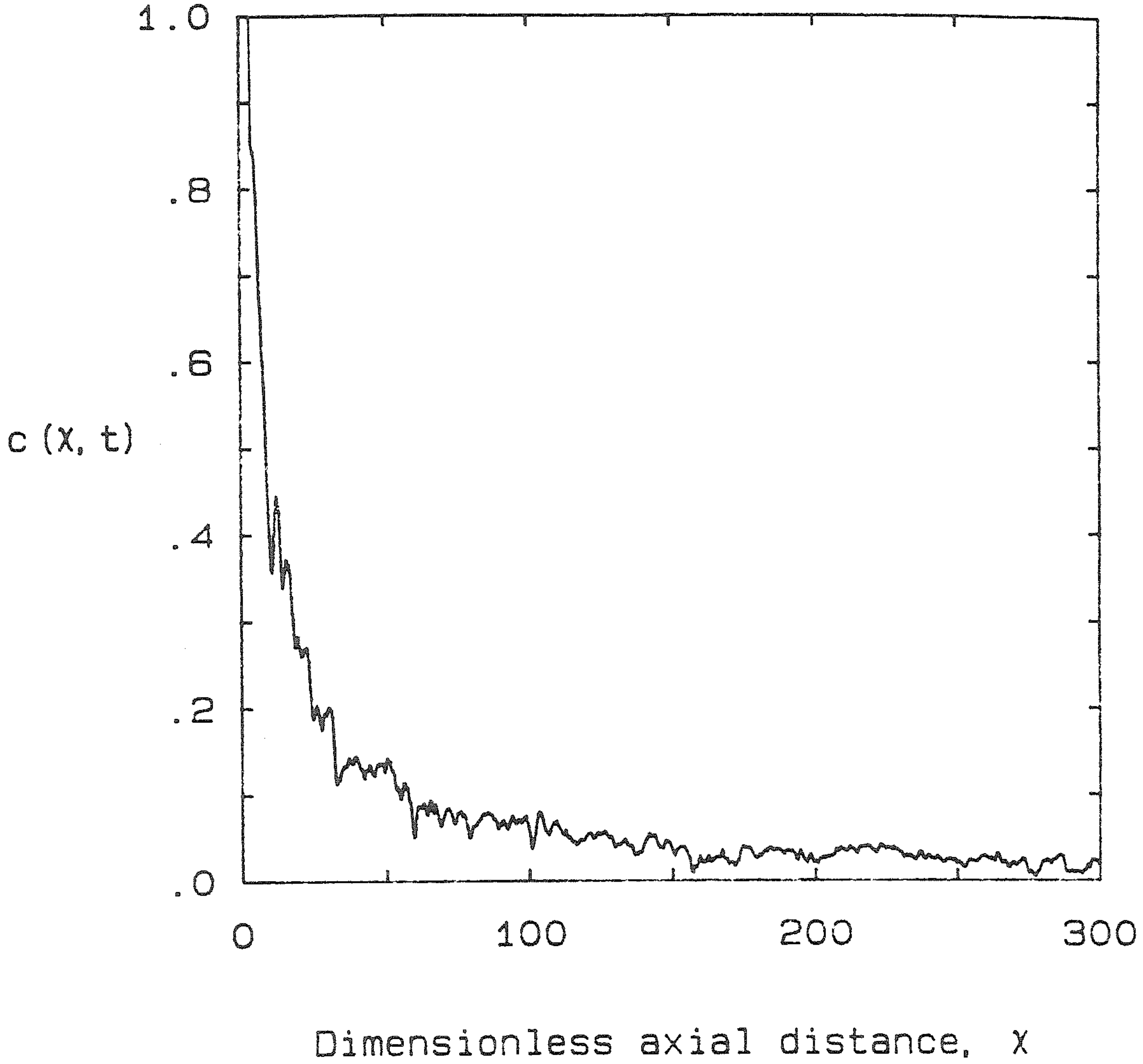

Figure 4-3. Jet fluid concentration profile from figure 4-2 .

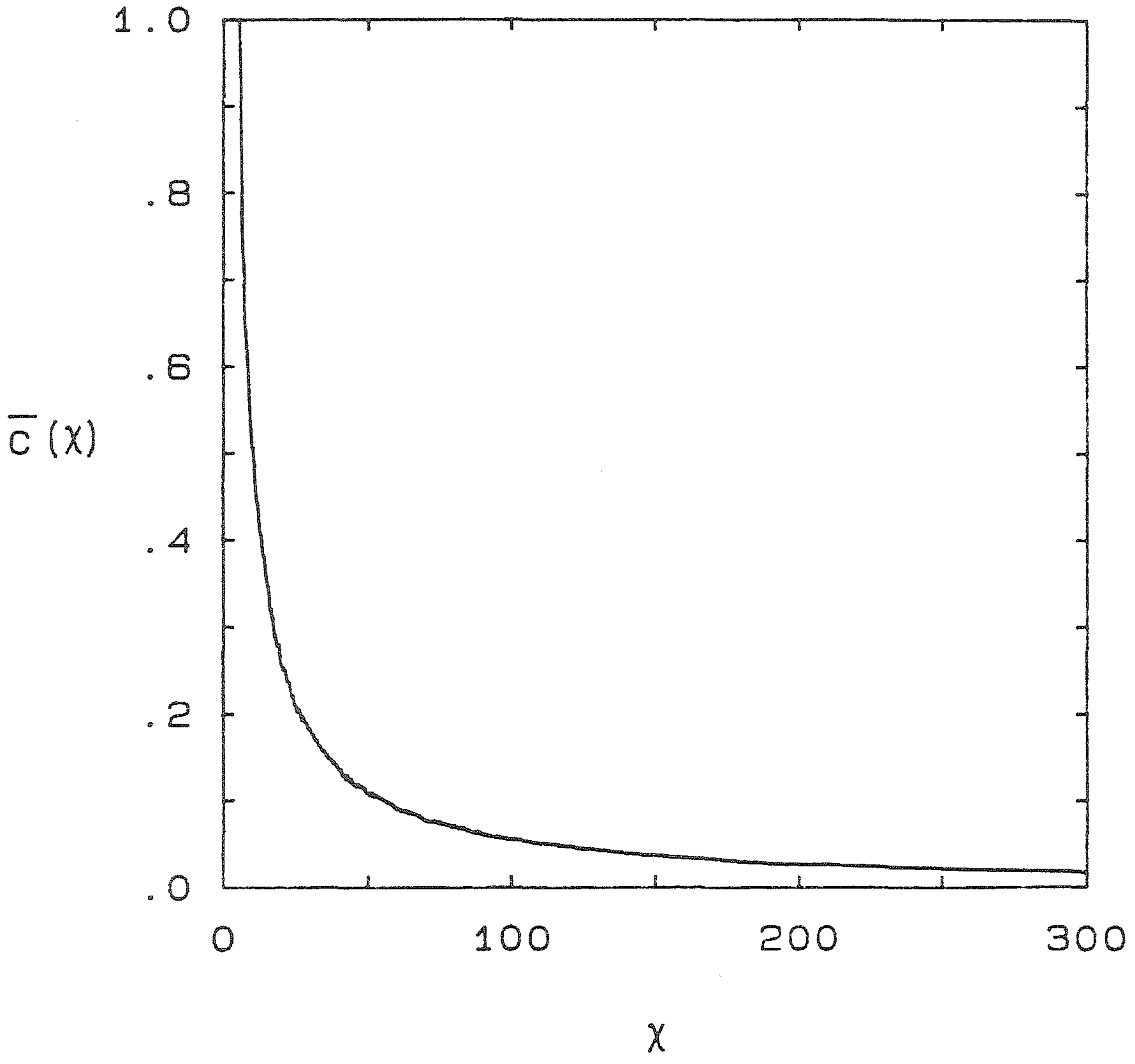

Figure 4-4. Mean centerline jet fluid concentration profile; $0 \leq \chi \leq 300$, Re = 5,000 .

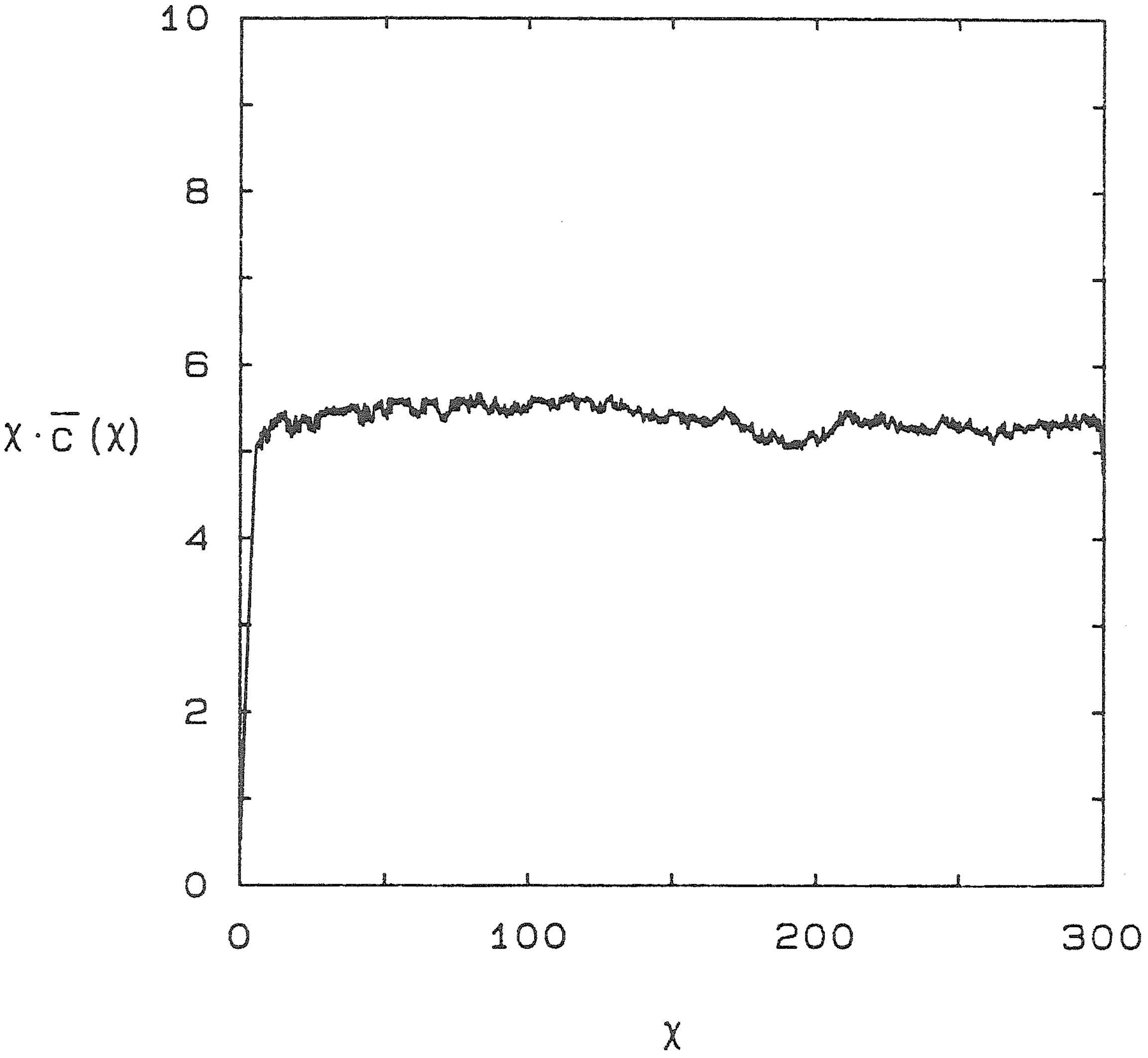

Figure 4-5. Verification of similarity in figure 4-4 ; $0 \leqq \chi \leqq 300$, $Re = 5{,}000$.

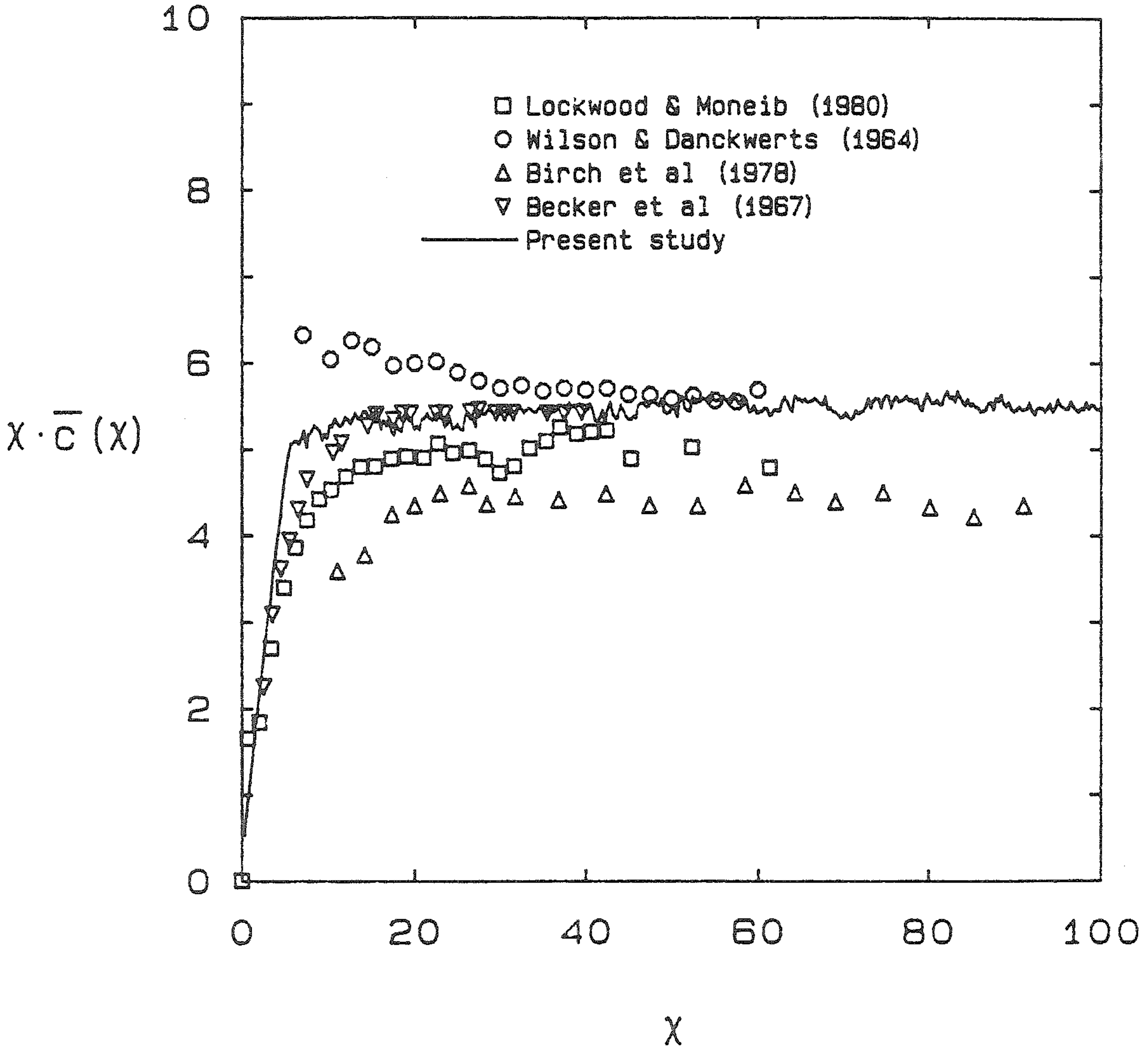

Figure 4-6. $\chi \cdot \overline{c}(\chi)$ profile from figure 4-5 compared with other experiments; $0 \leq \chi \leq 100$.

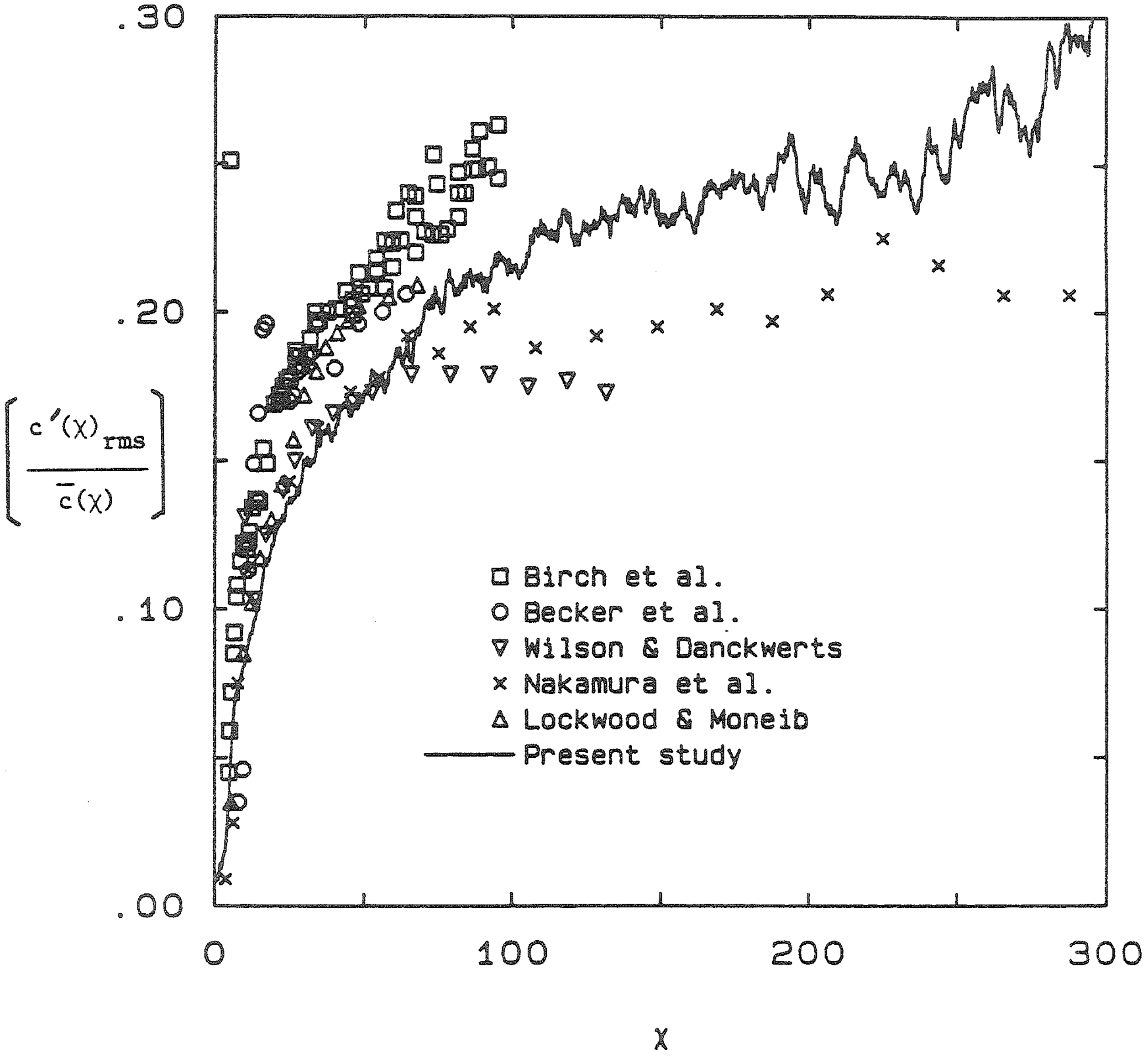

Figure 4-7. Centerline concentration fluctuation intensity profiles; $0 \leq \chi \leq 300$.

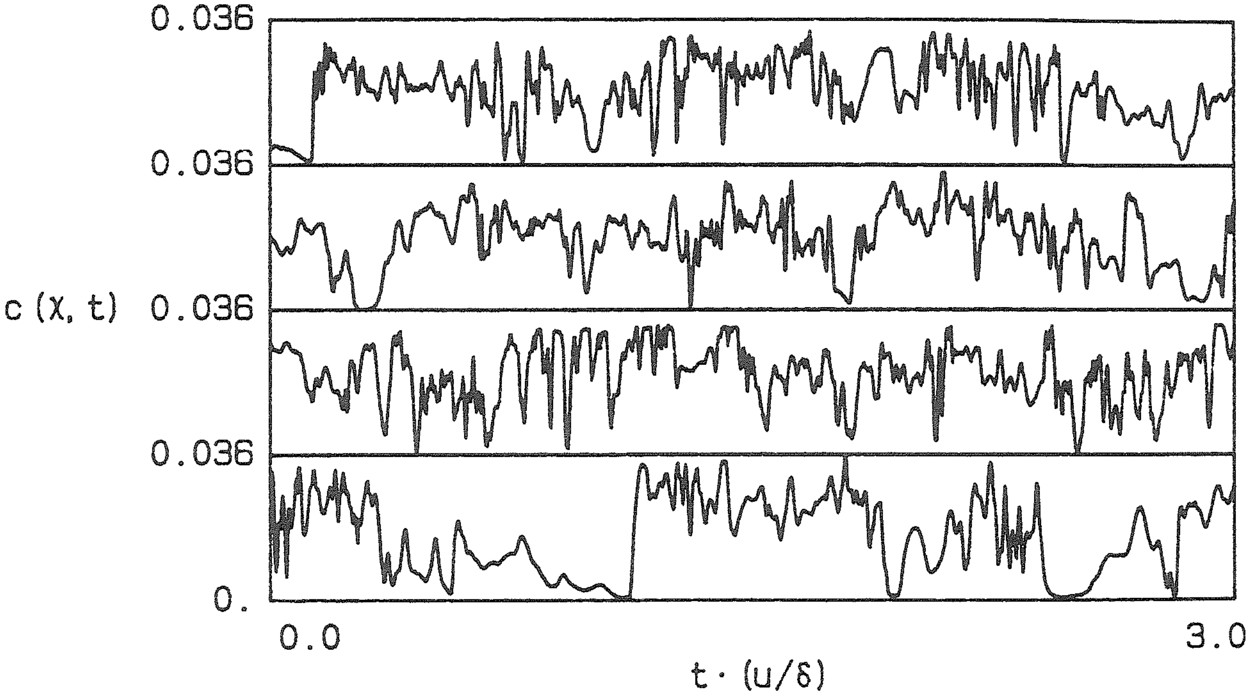

Figure 4-8a. Concentration vs. time at $\chi = 300$, $\eta = 0$; Re = 1,500.

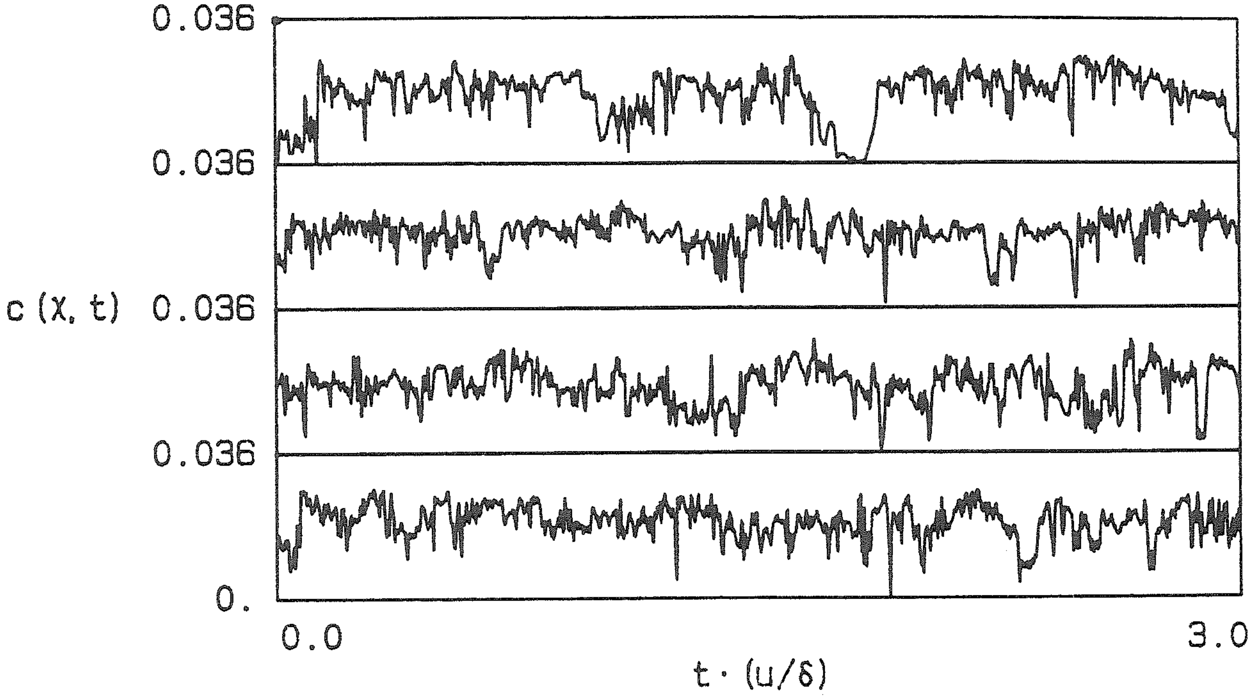

Figure 4-8b. Concentration vs. time at $\chi = 300$, $\eta = 0$; Re = 5,000 .

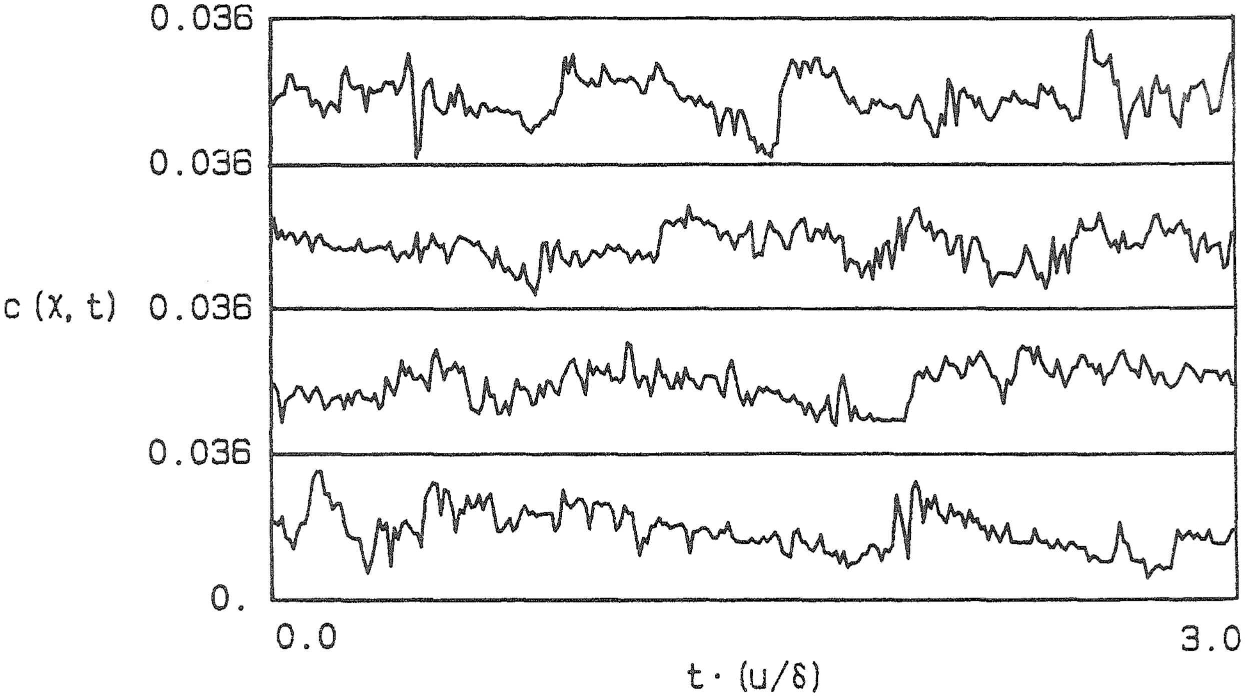

Figure 4-8c. Concentration vs. time at $\chi = 300$, $\eta = 0$; Re = 20,000.

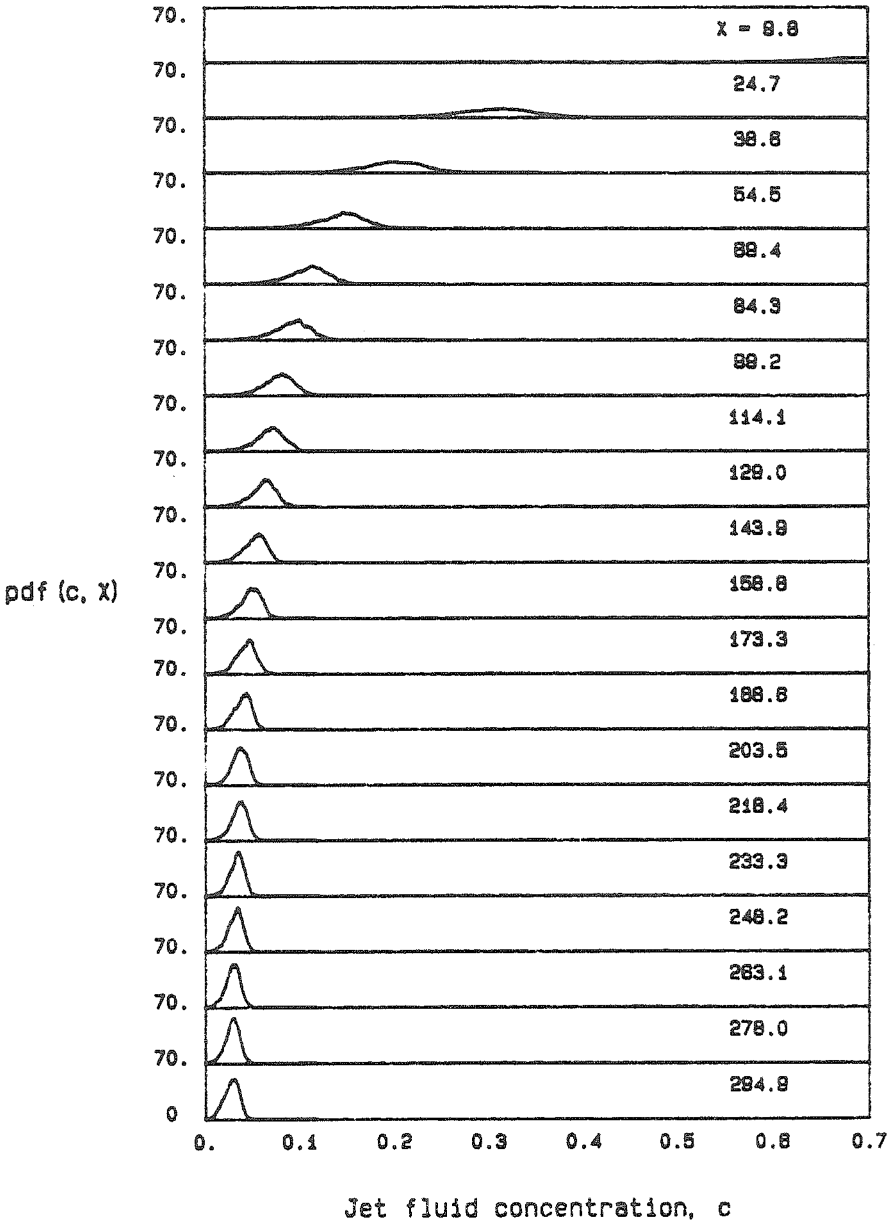

Figure 4-9. PDFs of jet fluid concentration along the jet axis; $0 \leq \chi \leq 300$, Re = 5,000.

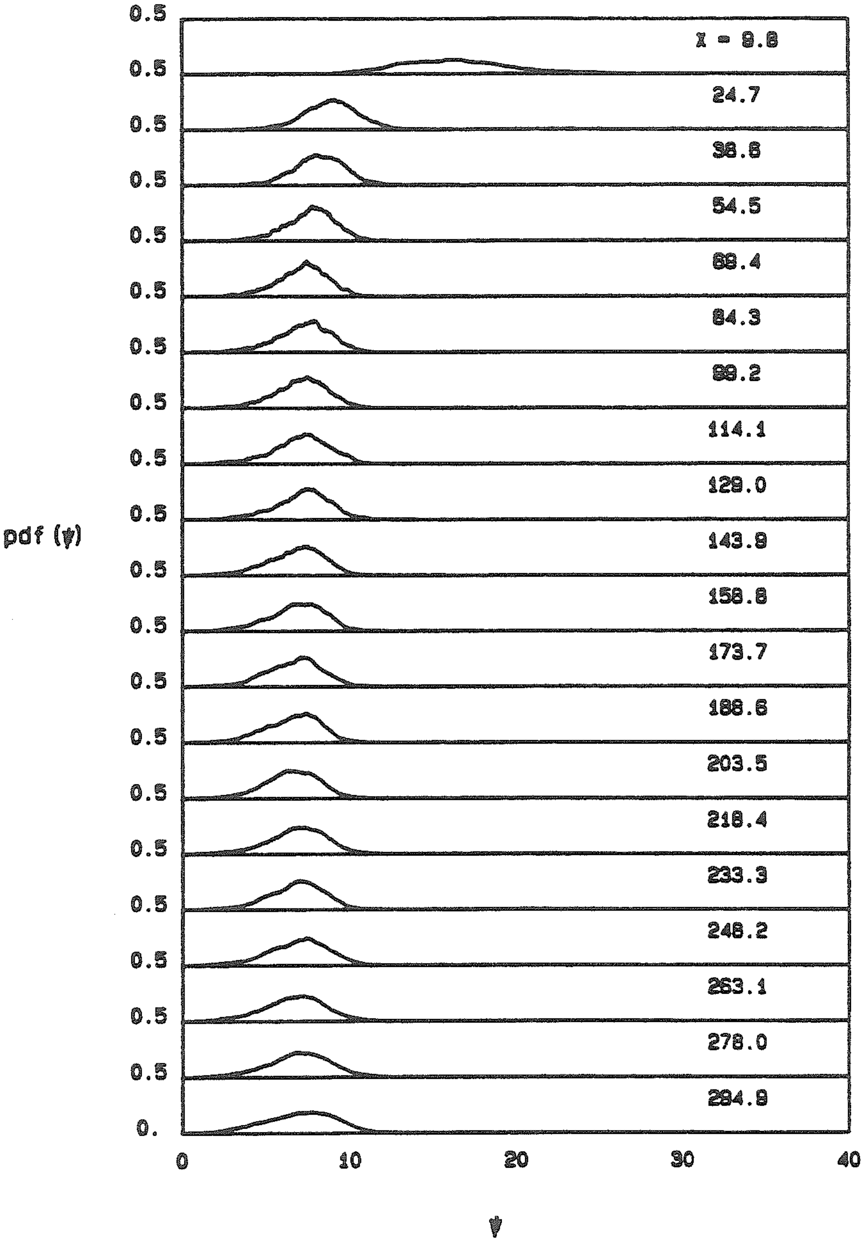

Figure 4-10. PDFs of the proposed axial similarity concentration ψ; $0 \leq \chi \leq 300$, Re = 5,000 .

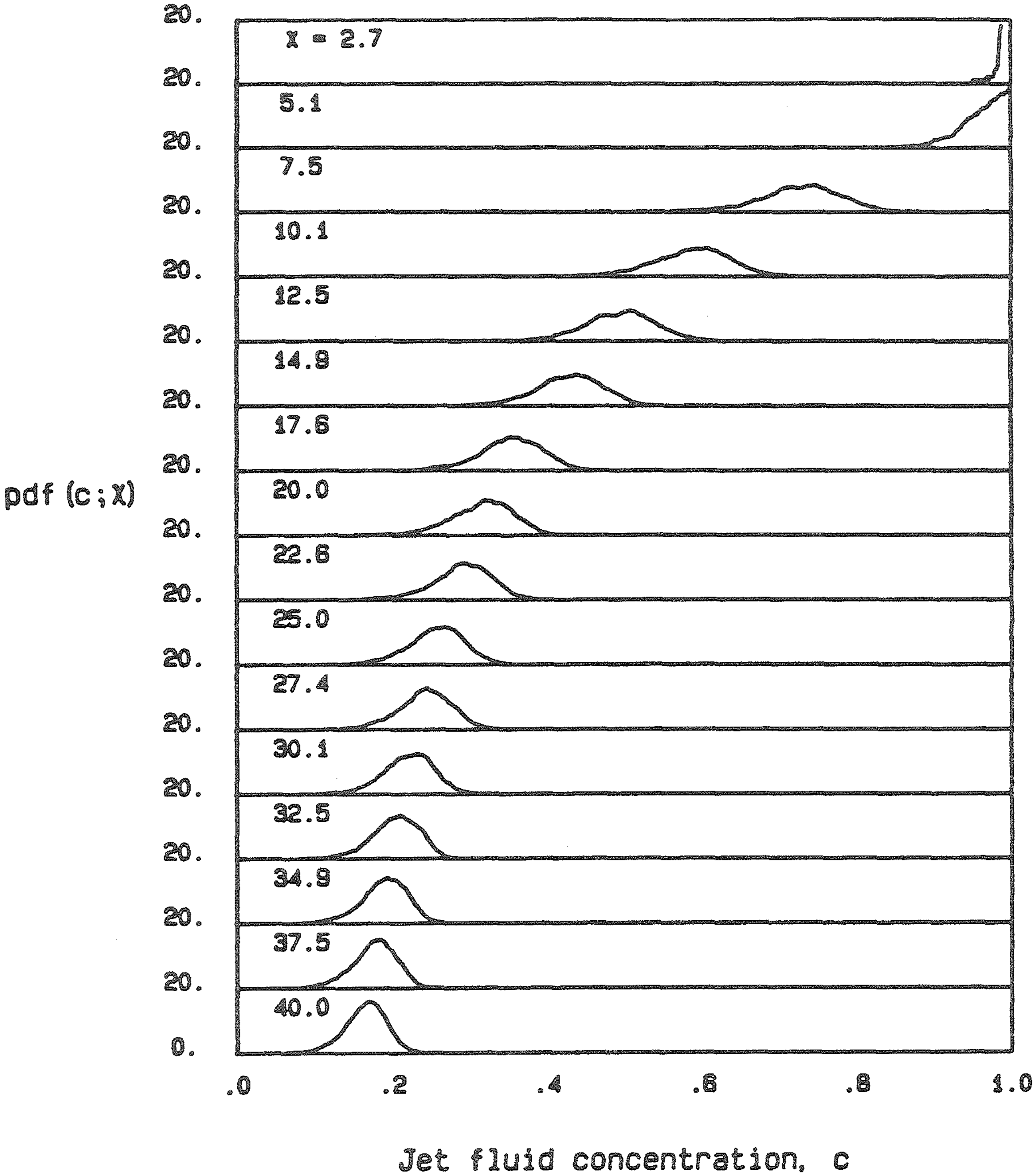

Figure 4-11. PDFs of jet fluid concentration along the jet axis; $0 \leq \chi \leq 40$, $Re = 5{,}000$.

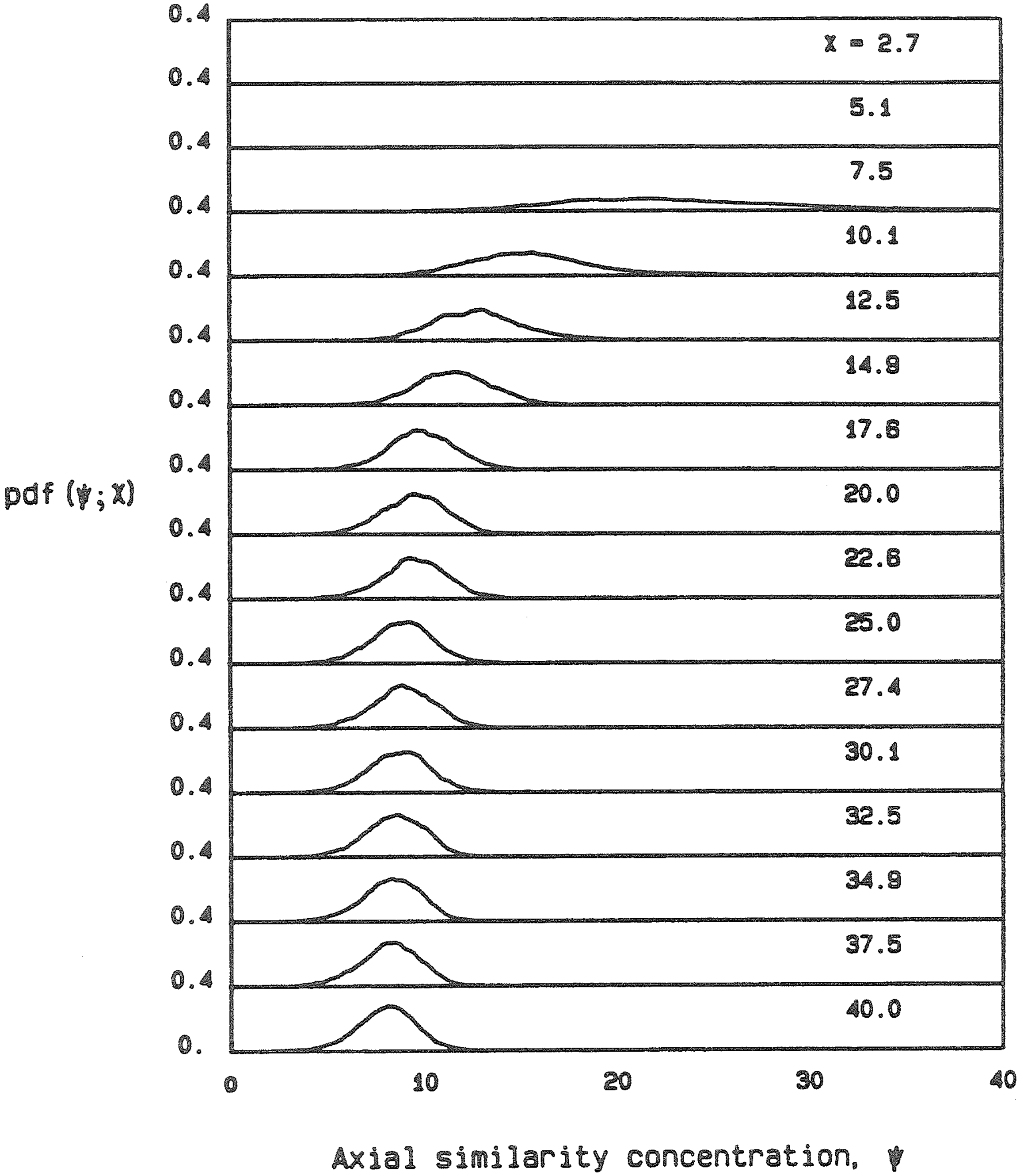

Figure 4-12. PDFs of the proposed axial similarity concentration ψ; $0 \leq \chi \leq 40$, $Re = 5{,}000$.

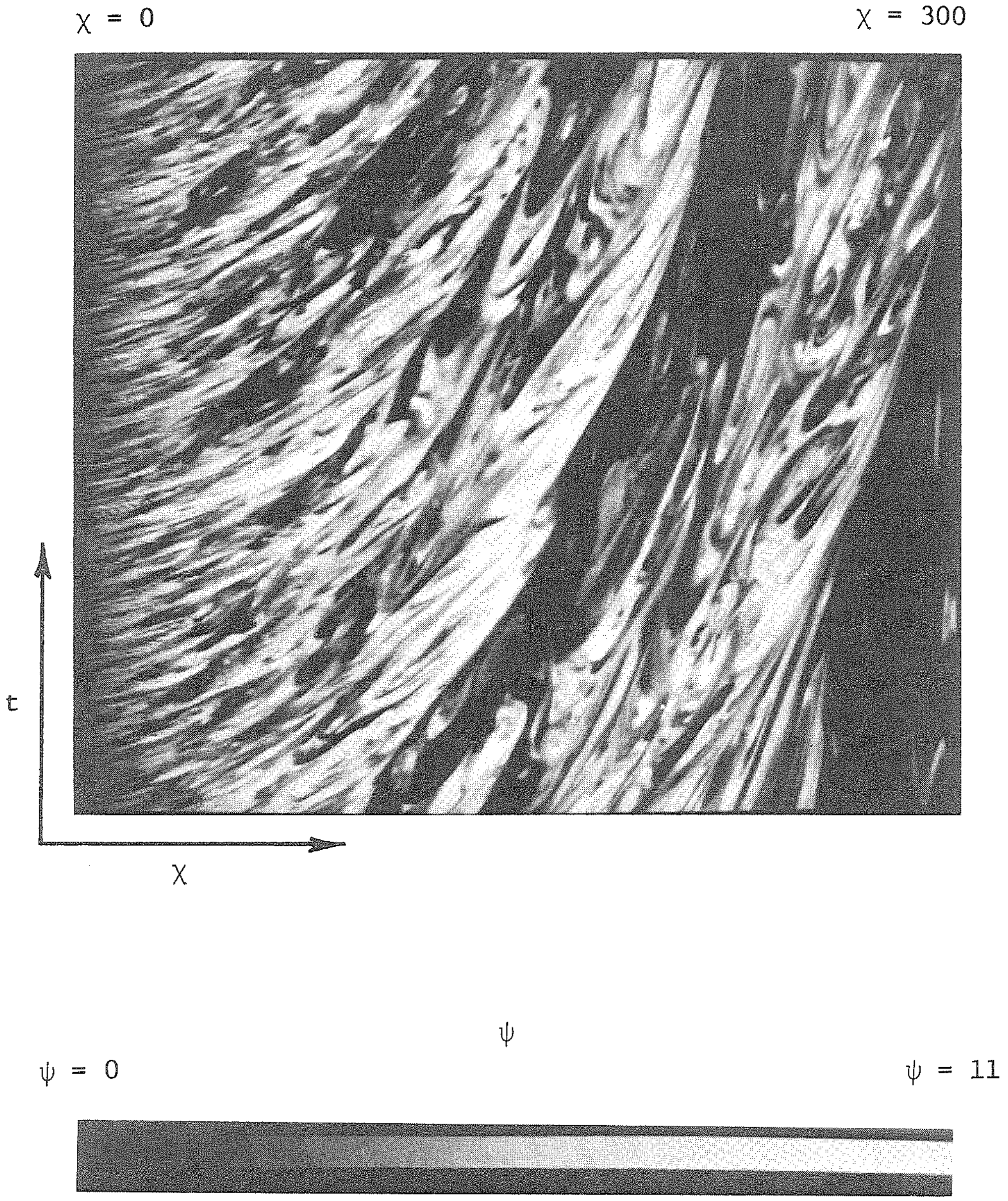

Figure 4-13a. χ-t diagram of the axial similarity concentration ψ; Re = 1,500, Monotone.

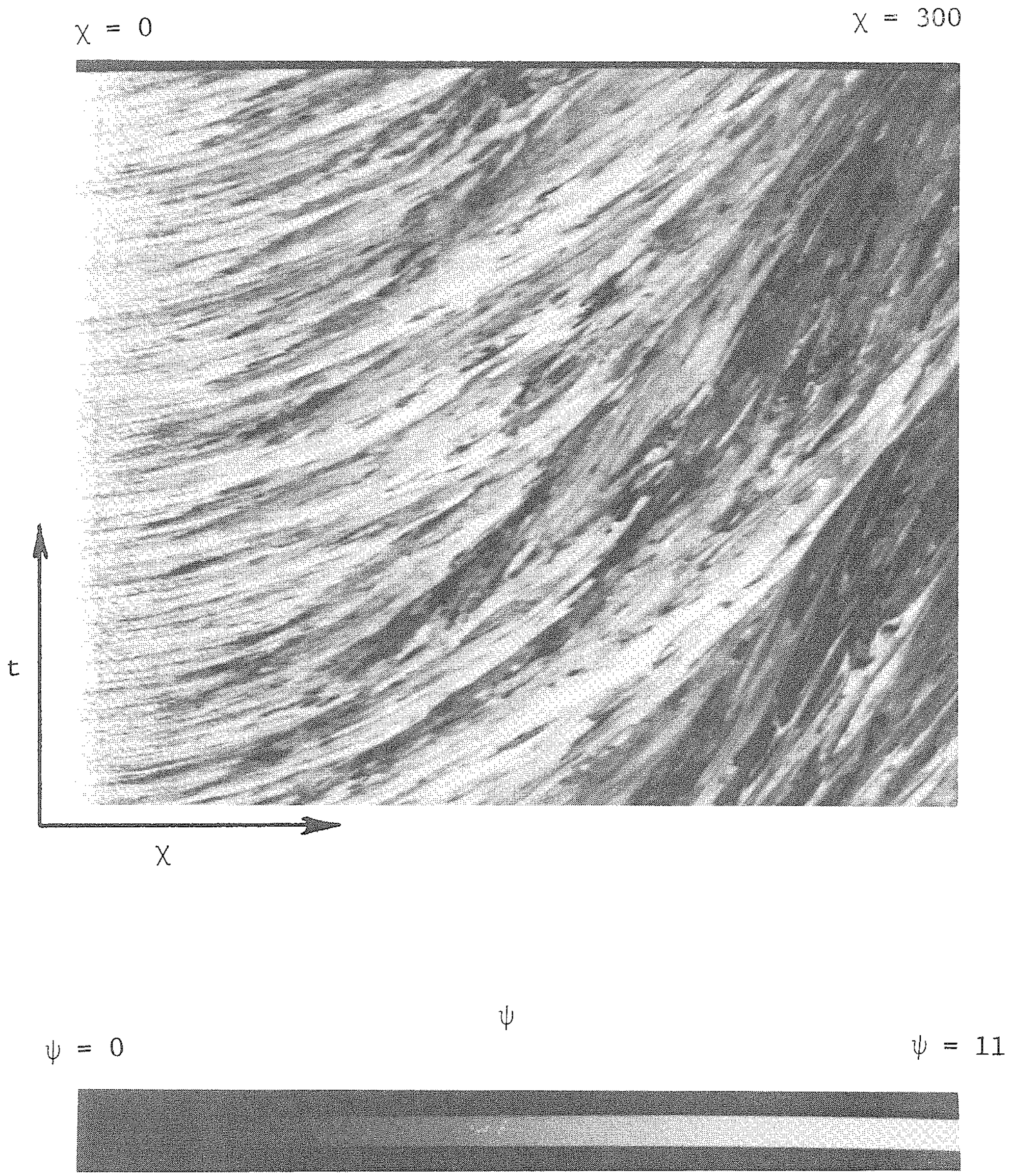

Figure 4-13b. χ-t diagram of the axial similarity concentration ψ; Re = 5,000, Monotone.

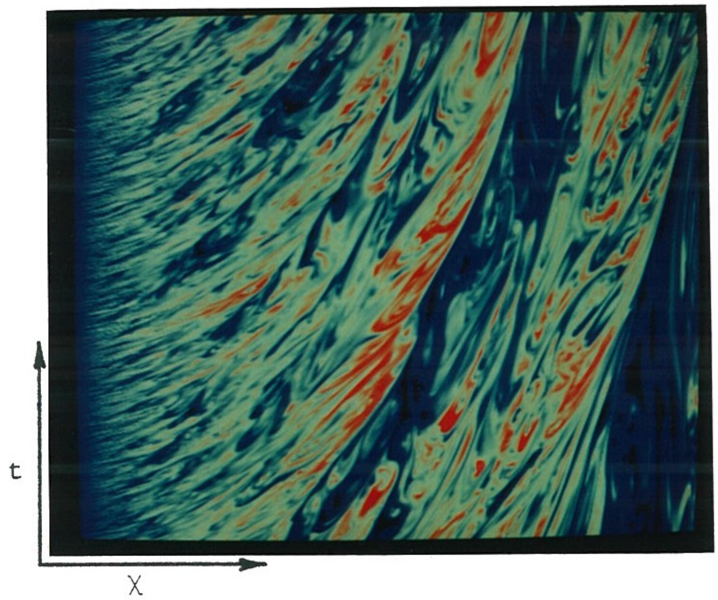

Figure 4-14a. χ-t diagram of the axial similarity concentration ψ; Re = 1,500 , Pseudocolor.

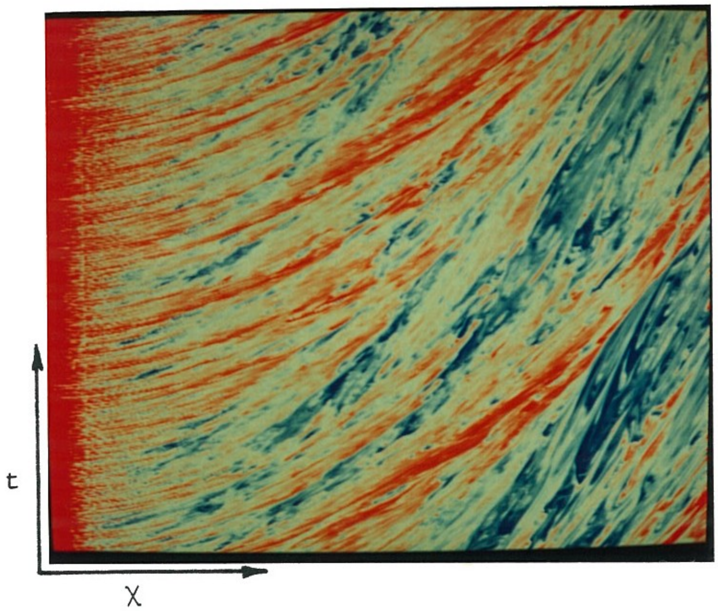

Figure 4-14b. χ-t diagram of the axial similarity concentration ψ; Re = 5,000 , Pseudocolor.

a. Re = 1,500

b. Re = 5,000

Figure 4-15. Composite χ-t diagrams of the similarity concentration ψ.

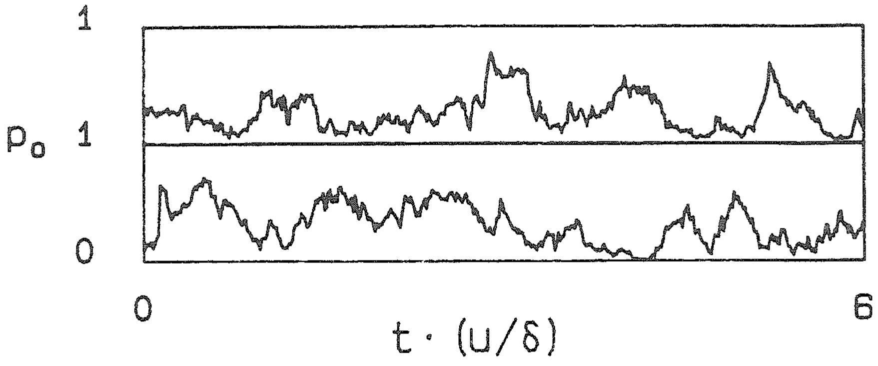

a. Re = 1,500

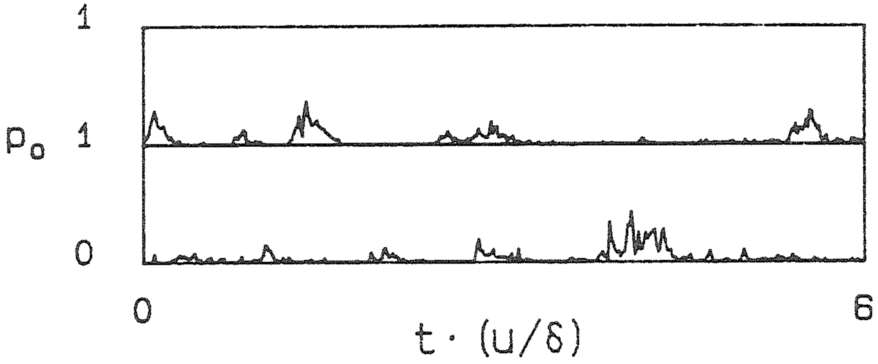

b. Re = 5,000

Figure 4-16. Unmixed ambient fluid probability $p_o(0,t)$ vs. time.

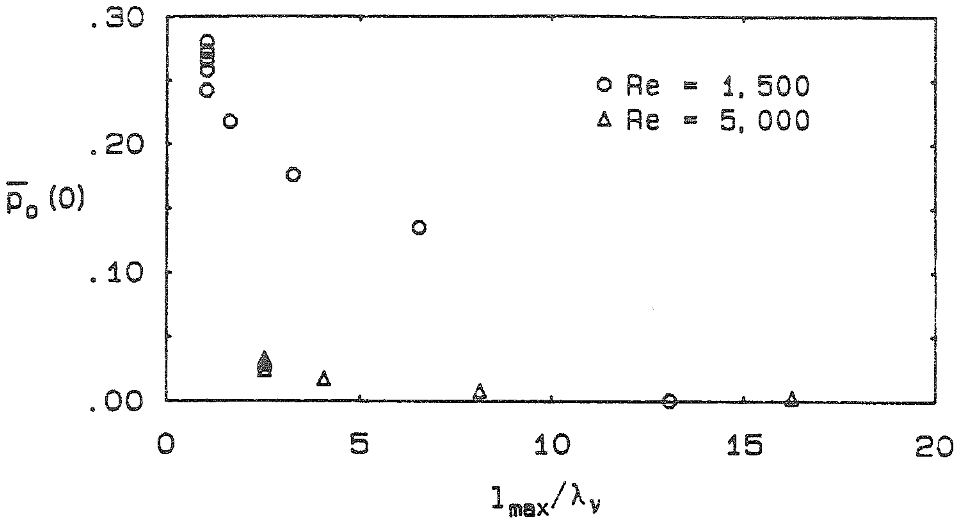

a. Resolution based on maximum image volume dimension.

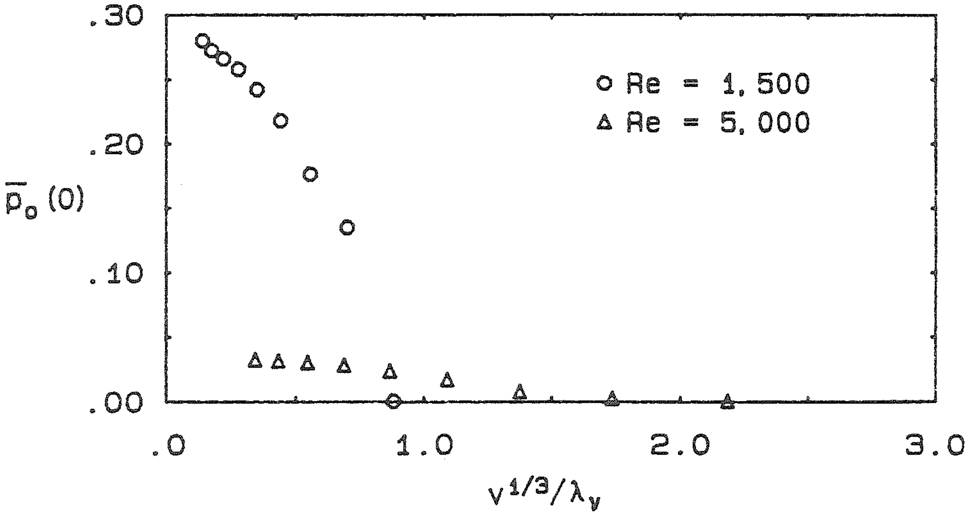

b. Resolution based on cube root of image volume.

Figure 4-17. Effect of resolution on measured $\overline{p}_o(0)$.

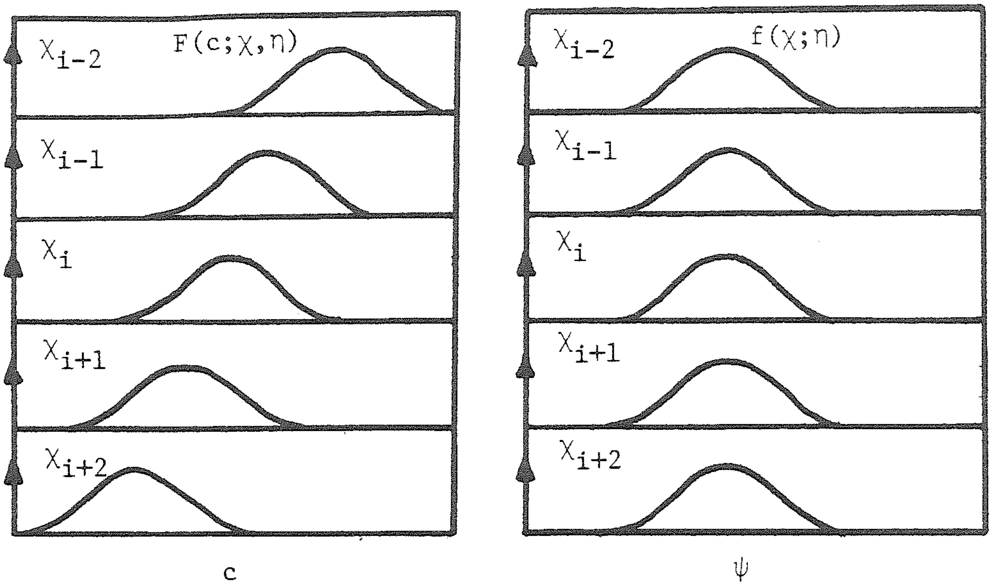

a. PDF of jet fluid concentration for a non-reacting jet.

b. PDF of similarity concentration for a non-reacting jet.

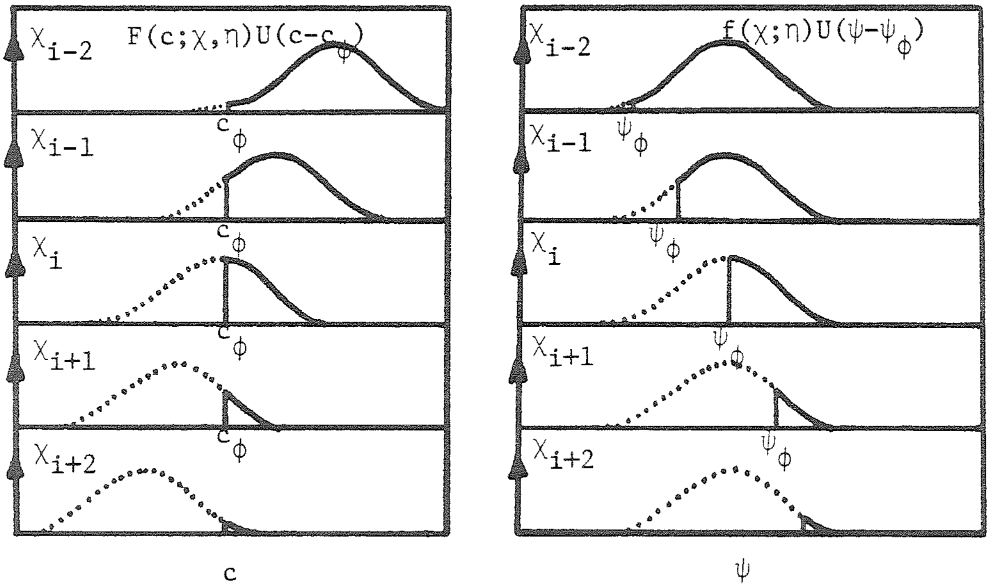

c. PDF of jet fluid concentration for a reacting jet.

d. PDF of similarity concentration for a reacting jet.

Figure 4-18. PDFs of c and ψ for non-reacting and reacting jets.

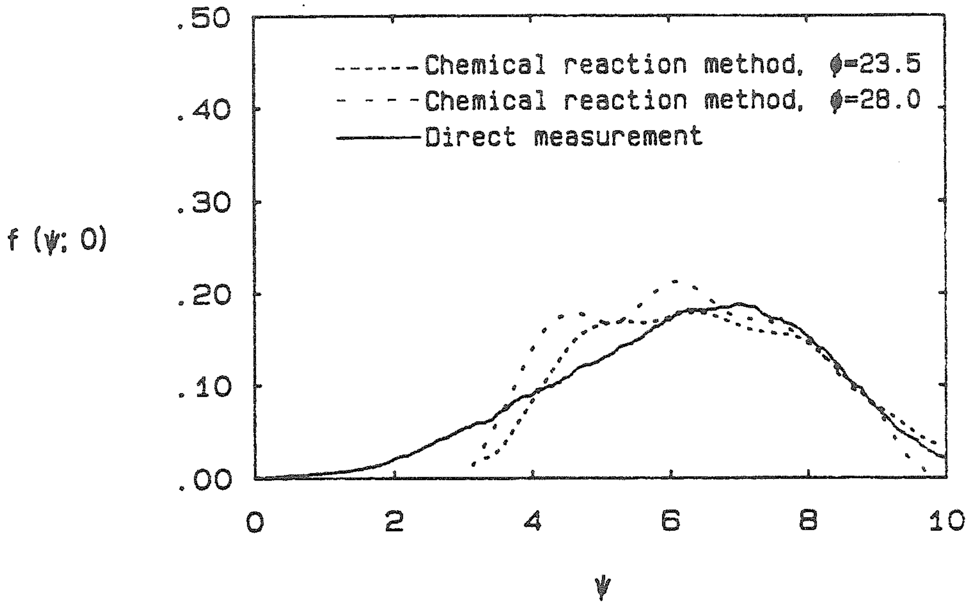

a. Re = 5,000

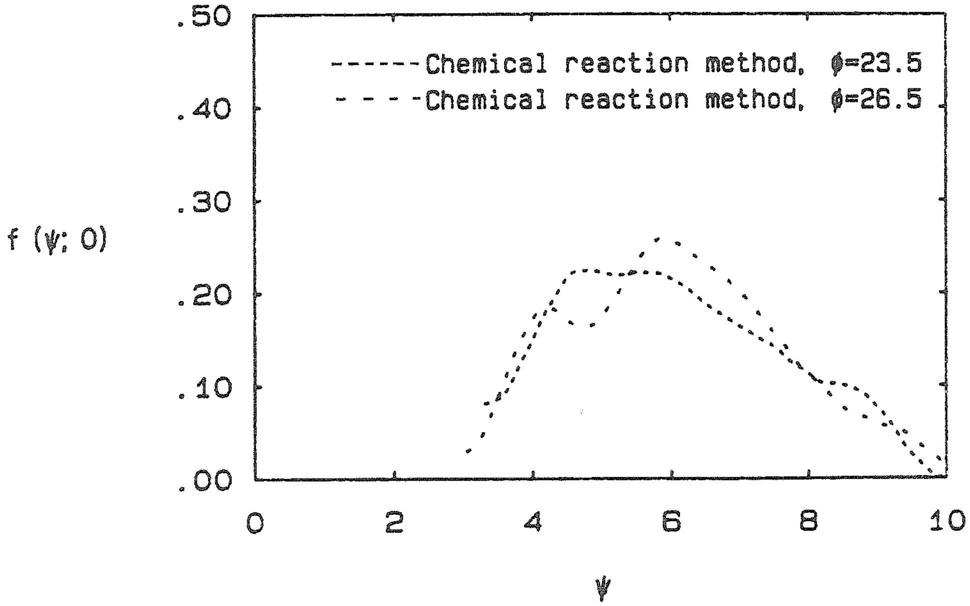

b. Re = 25,000

Figure 4-19. Similarity PDFs from the chemical reaction method; $\eta = 0$.

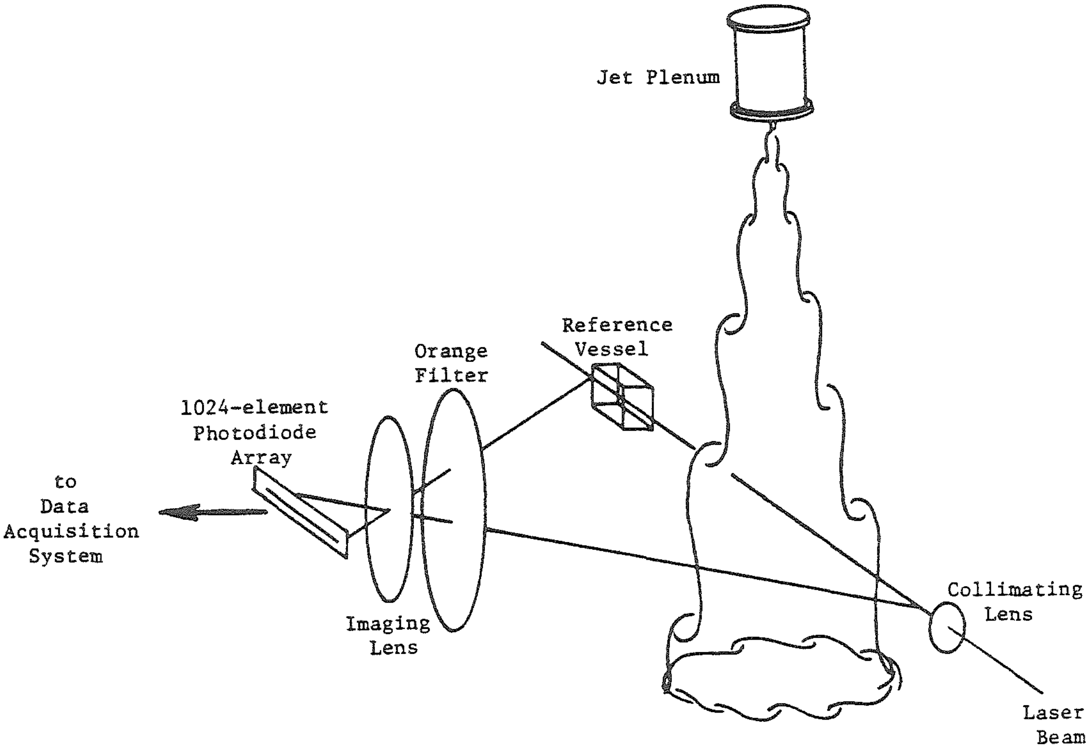

Figure 5-1. Schematic of radial imaging configuration.

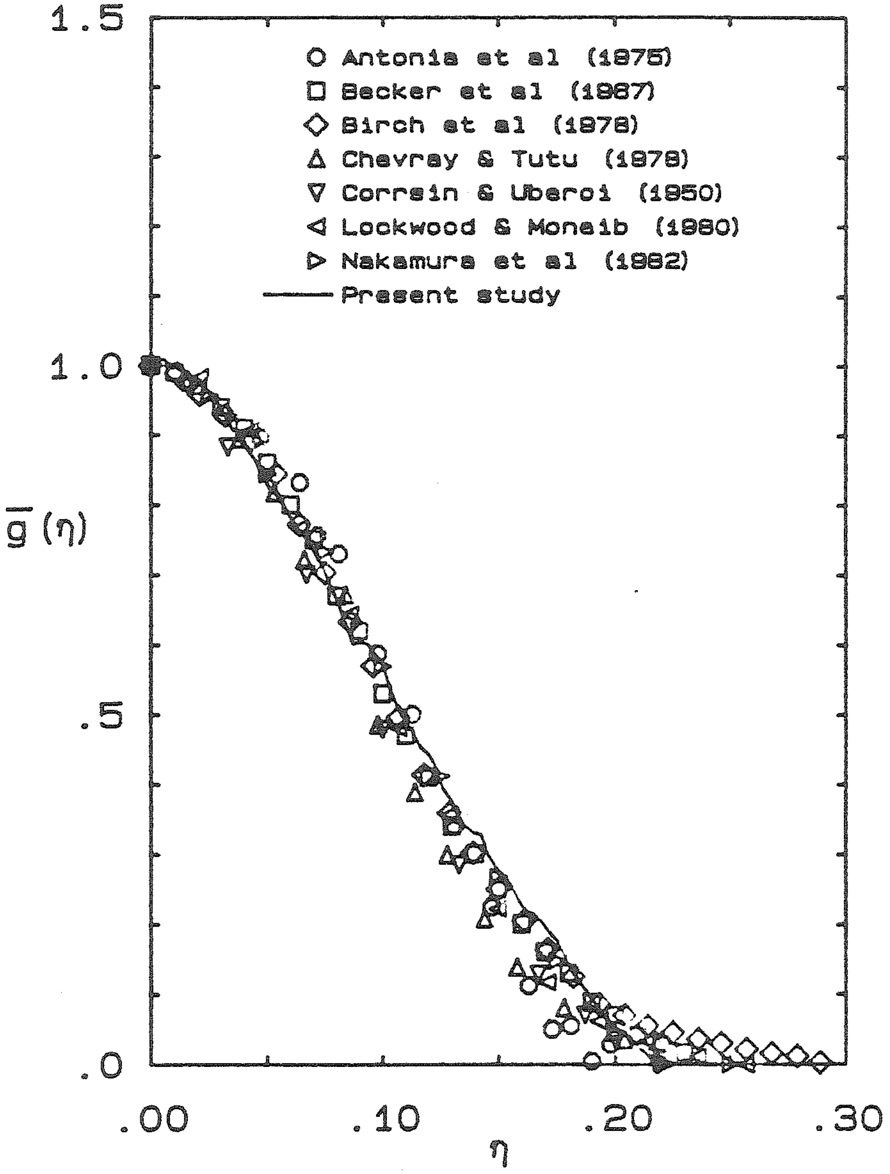

Figure 5-2. Mean radial profiles of concentration in similarity form.

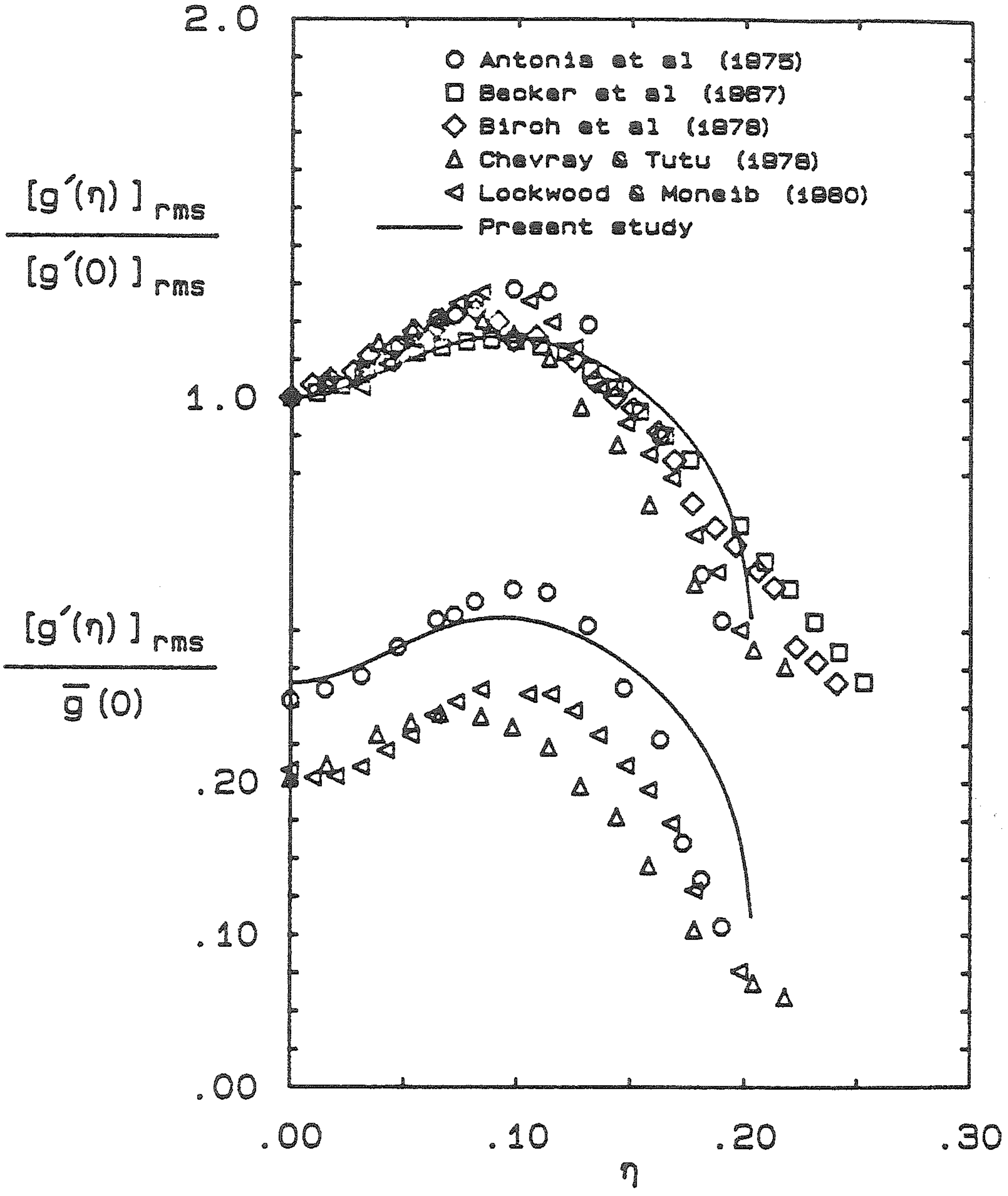

Figure 5-3. Radial profiles of concentration fluctuations.

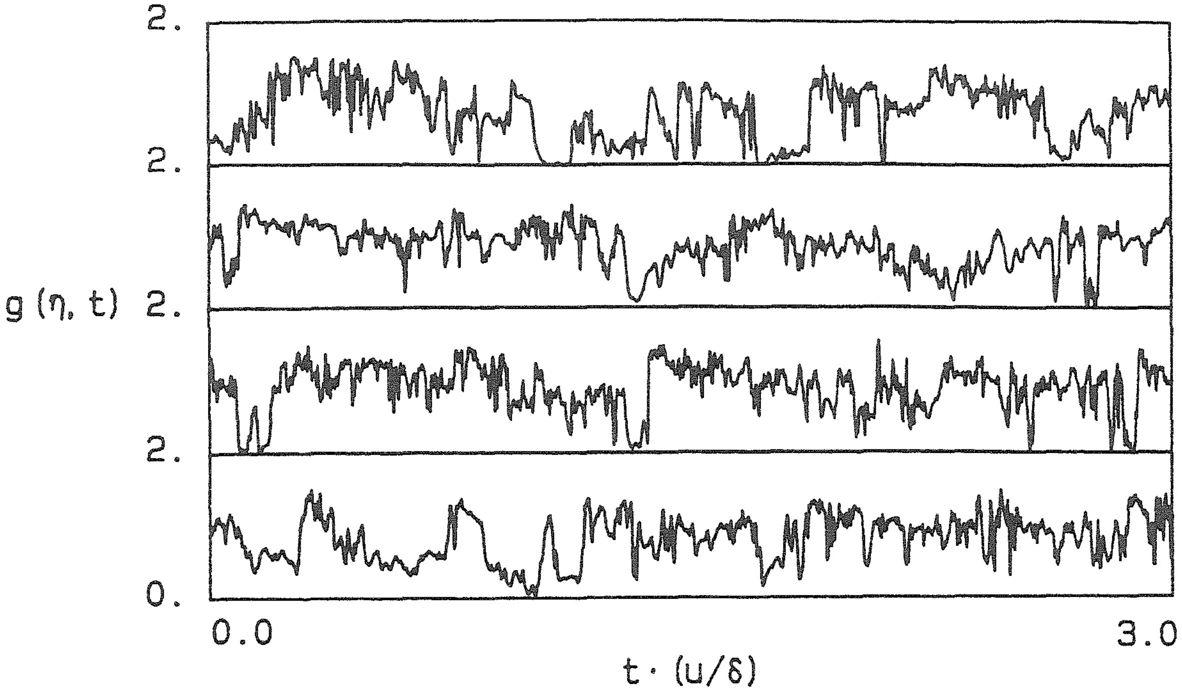

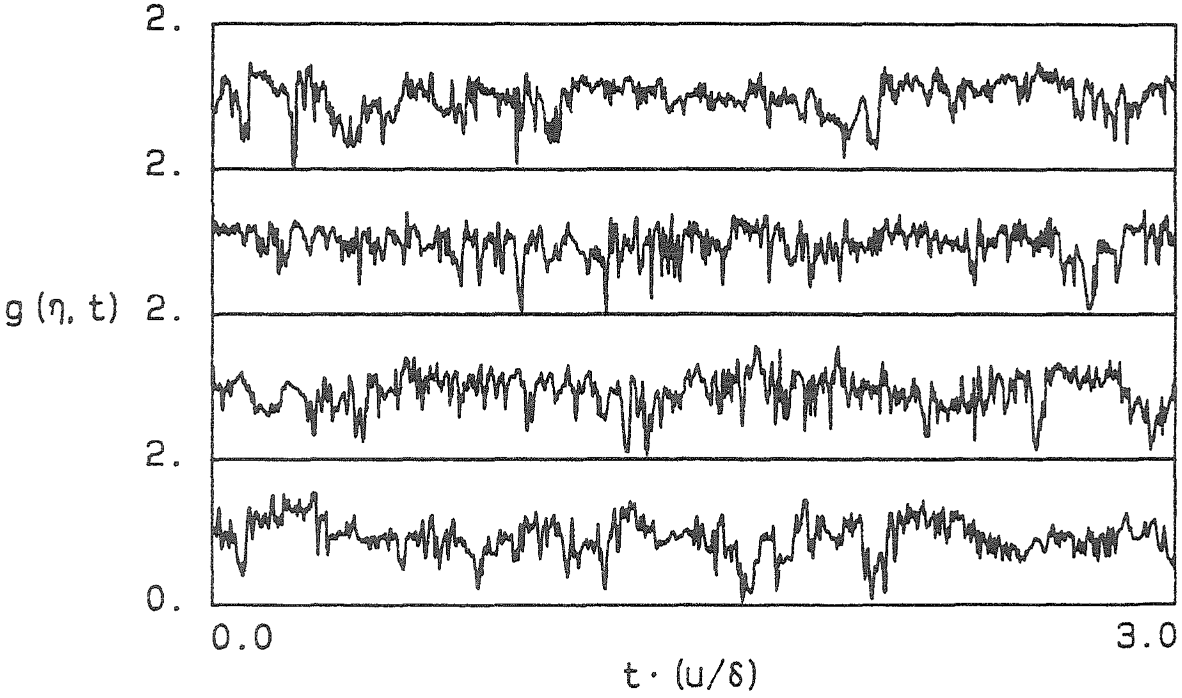

Figure 5-4a. Concentration vs. time at $\chi = 300$, $Re = 5{,}000$; $\eta = 0.04$.

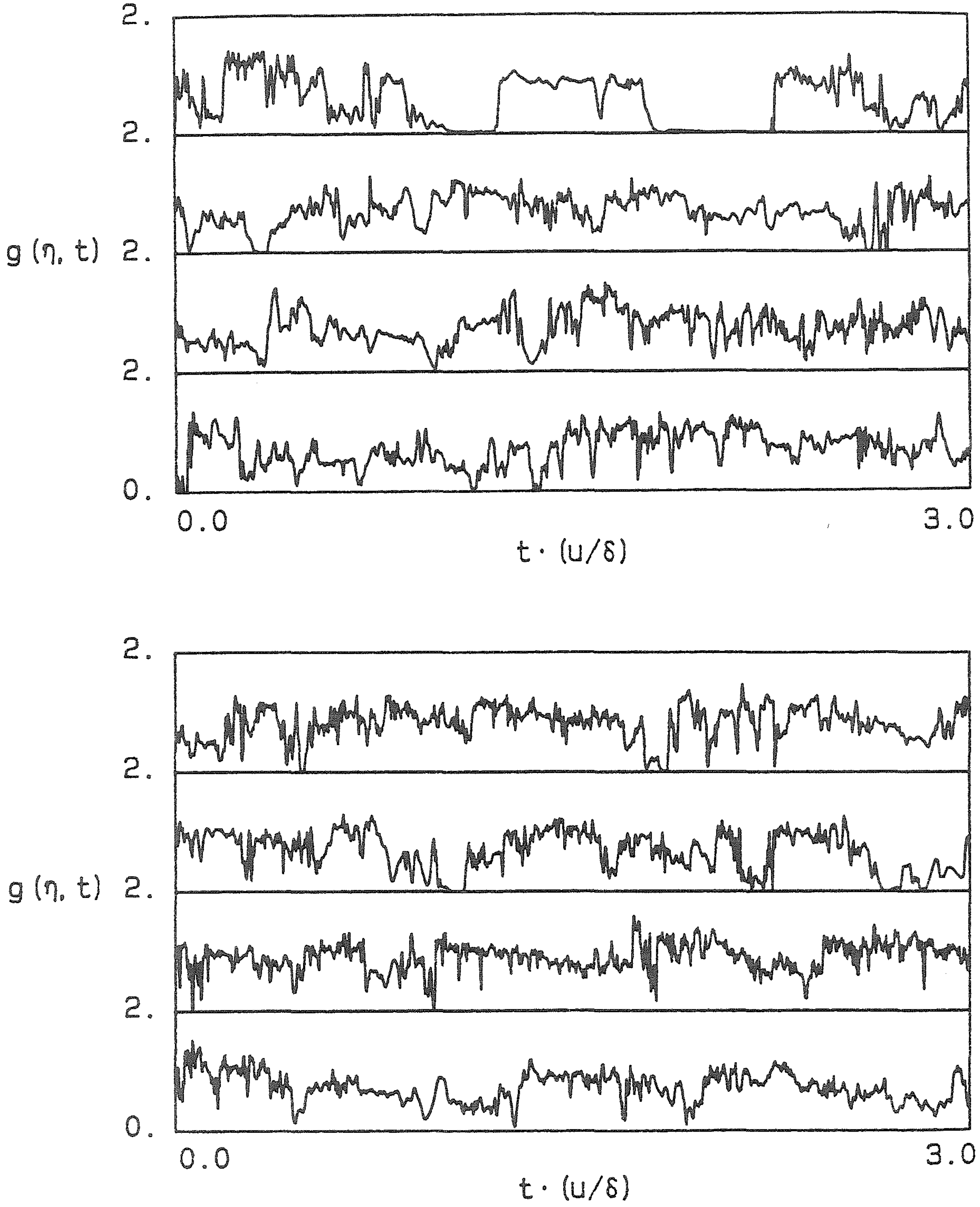

Figure 5-4b. Concentration vs. time at $\chi = 300$, Re = 5,000 ; $\eta = 0.08$.

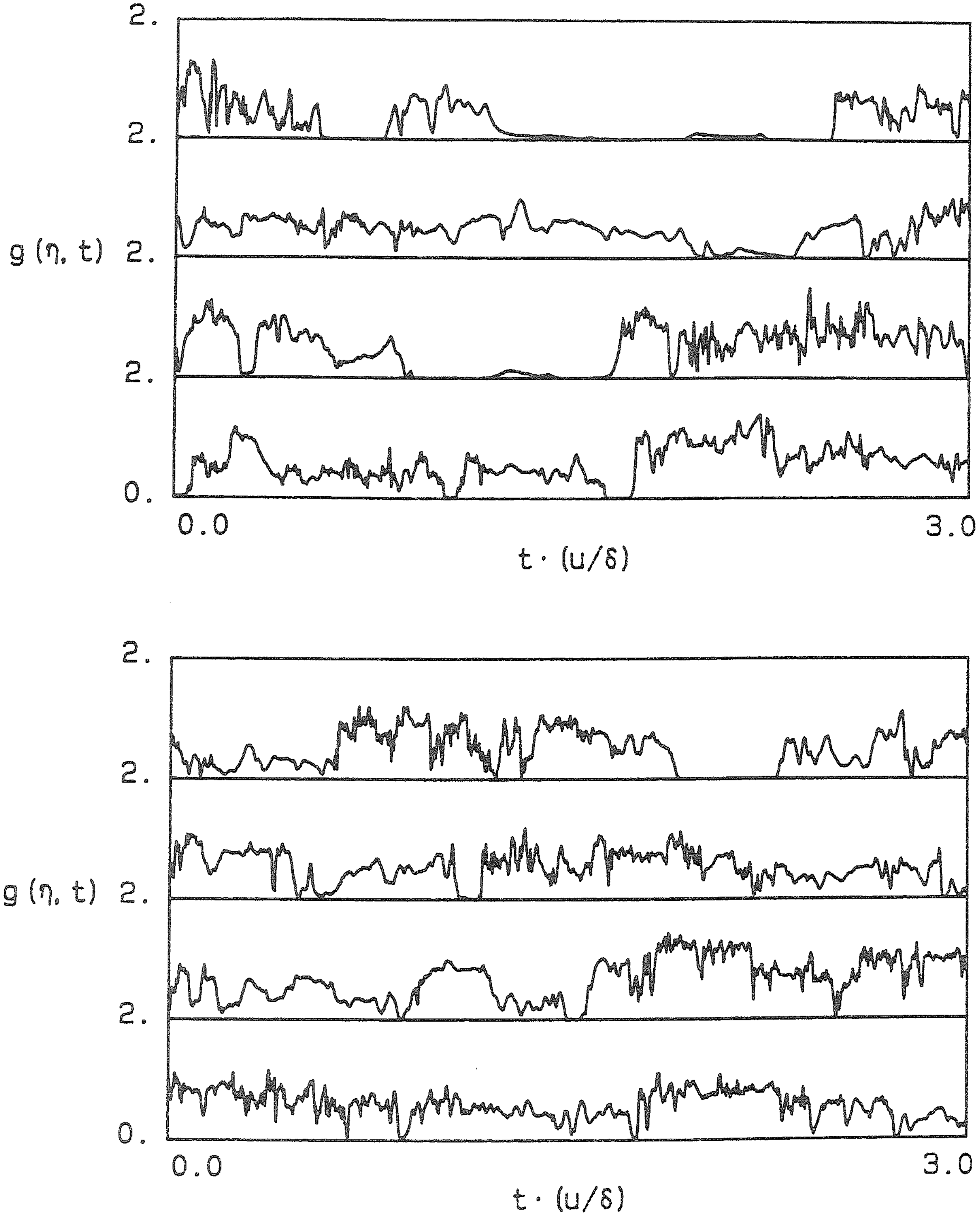

Figure 5-4c. Concentration vs. time at $\chi = 300$, $Re = 5,000$; $\eta = 0.12$.

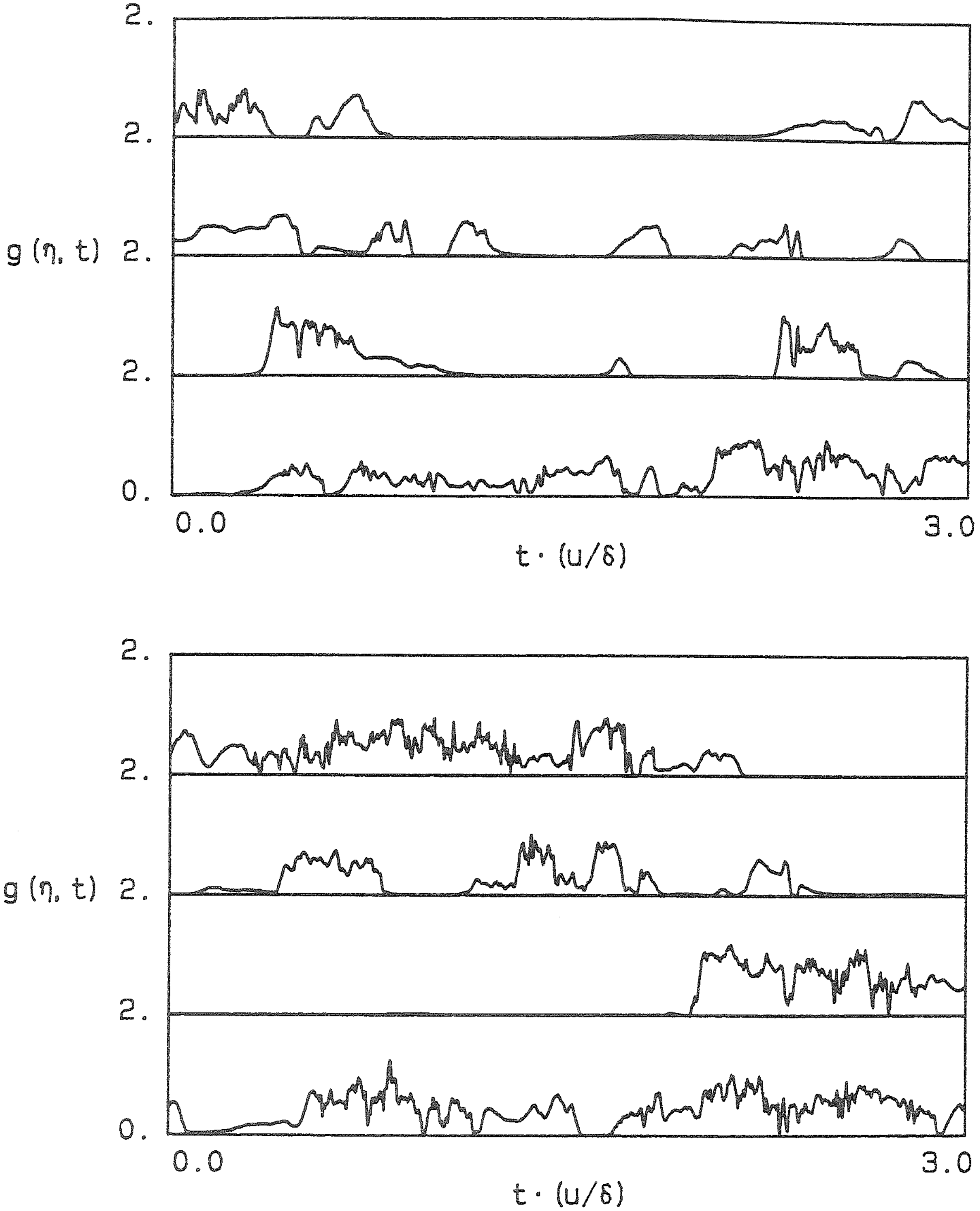

Figure 5-4d. Concentration vs. time at $\chi = 300$, Re = 5,000 ; $\eta = 0.16$.

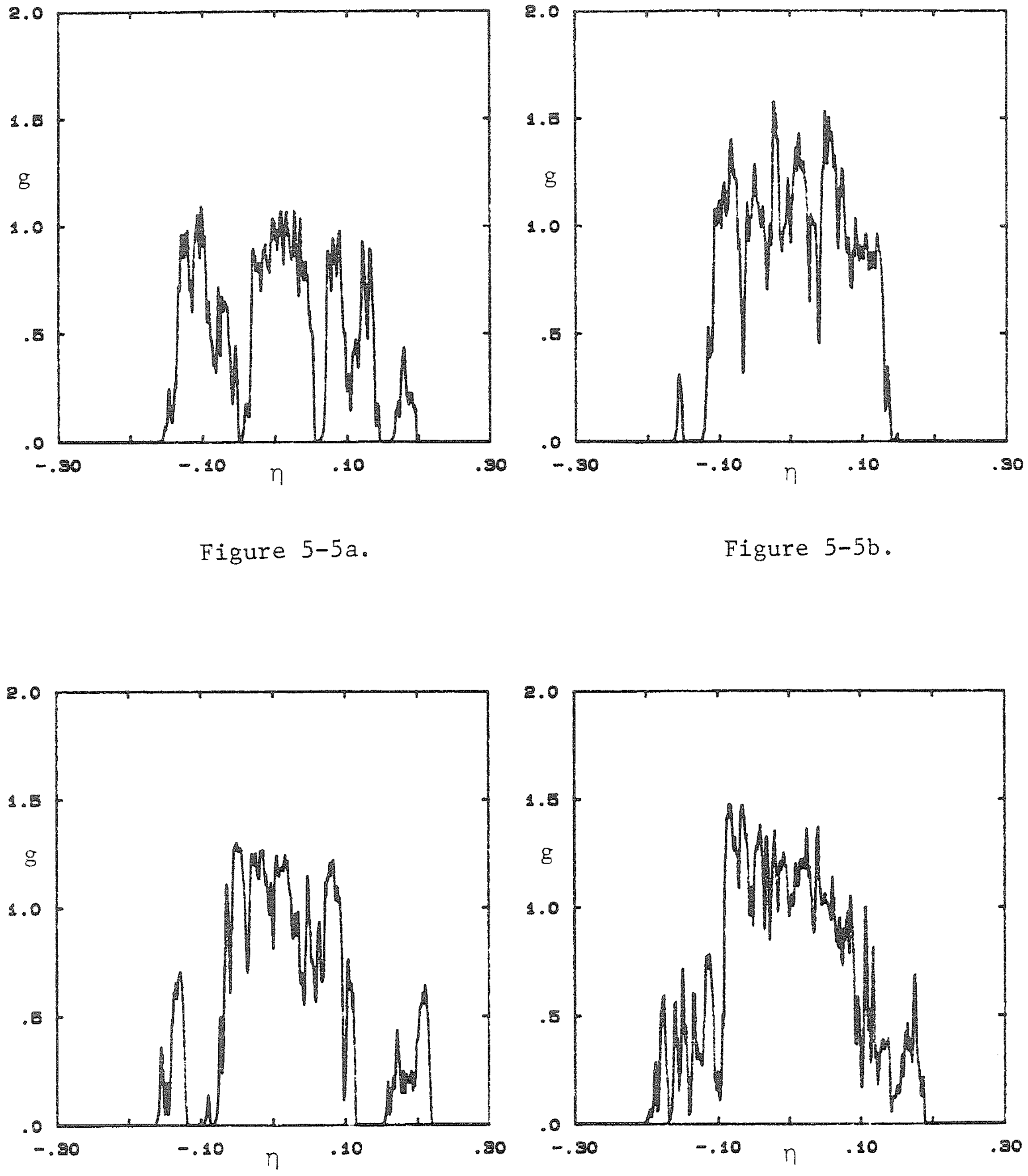

Figure 5-5a.

Figure 5-5b.

Figure 5-5c.

Figure 5-5d.

Figure 5-5. Several instantaneous radial profiles of concentration; $\chi = 300$, $Re = 5{,}000$.

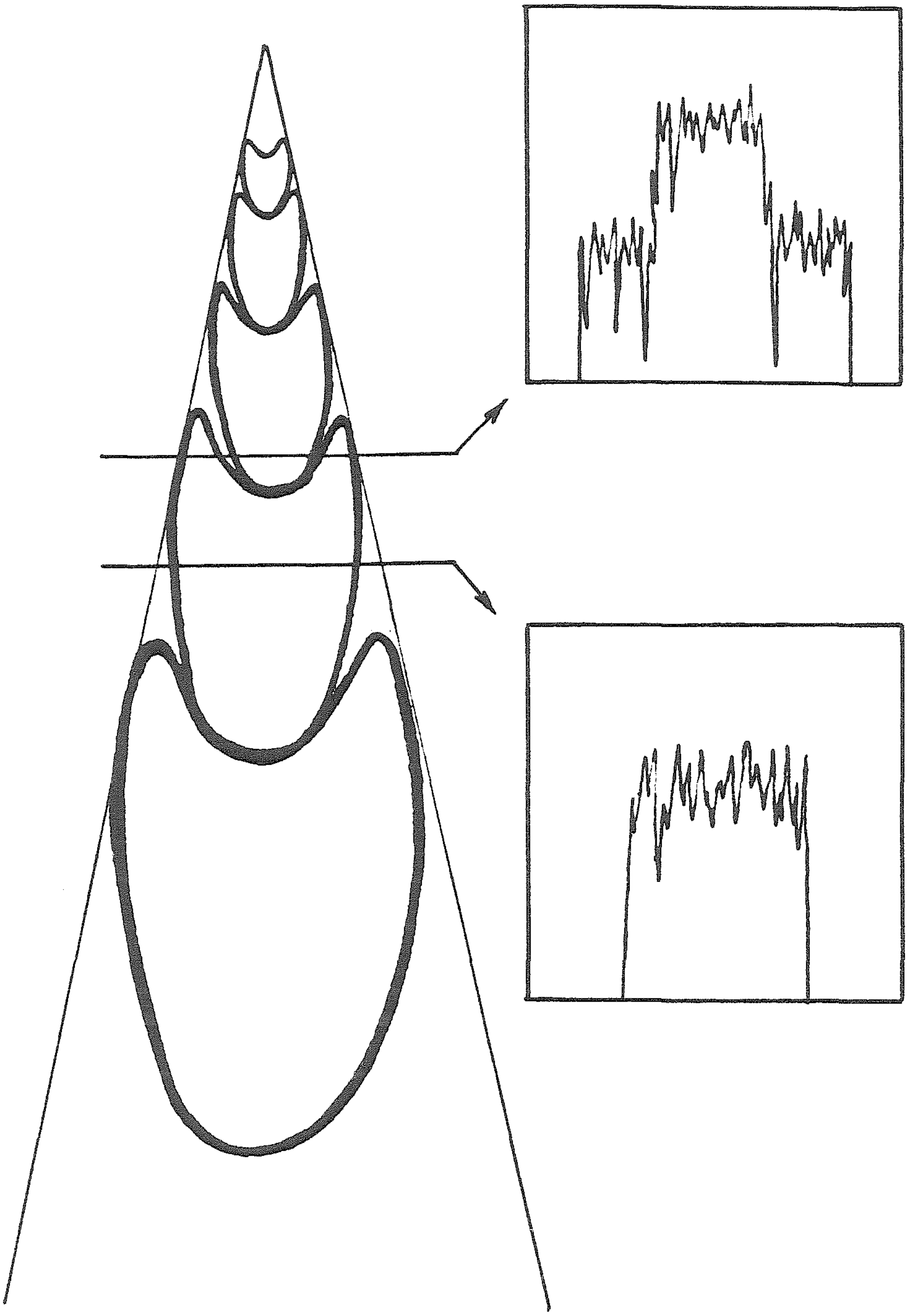

Figure 5-6. Interpretation of top-hat and two-level instantaneous profiles in the context of figure 3-19.

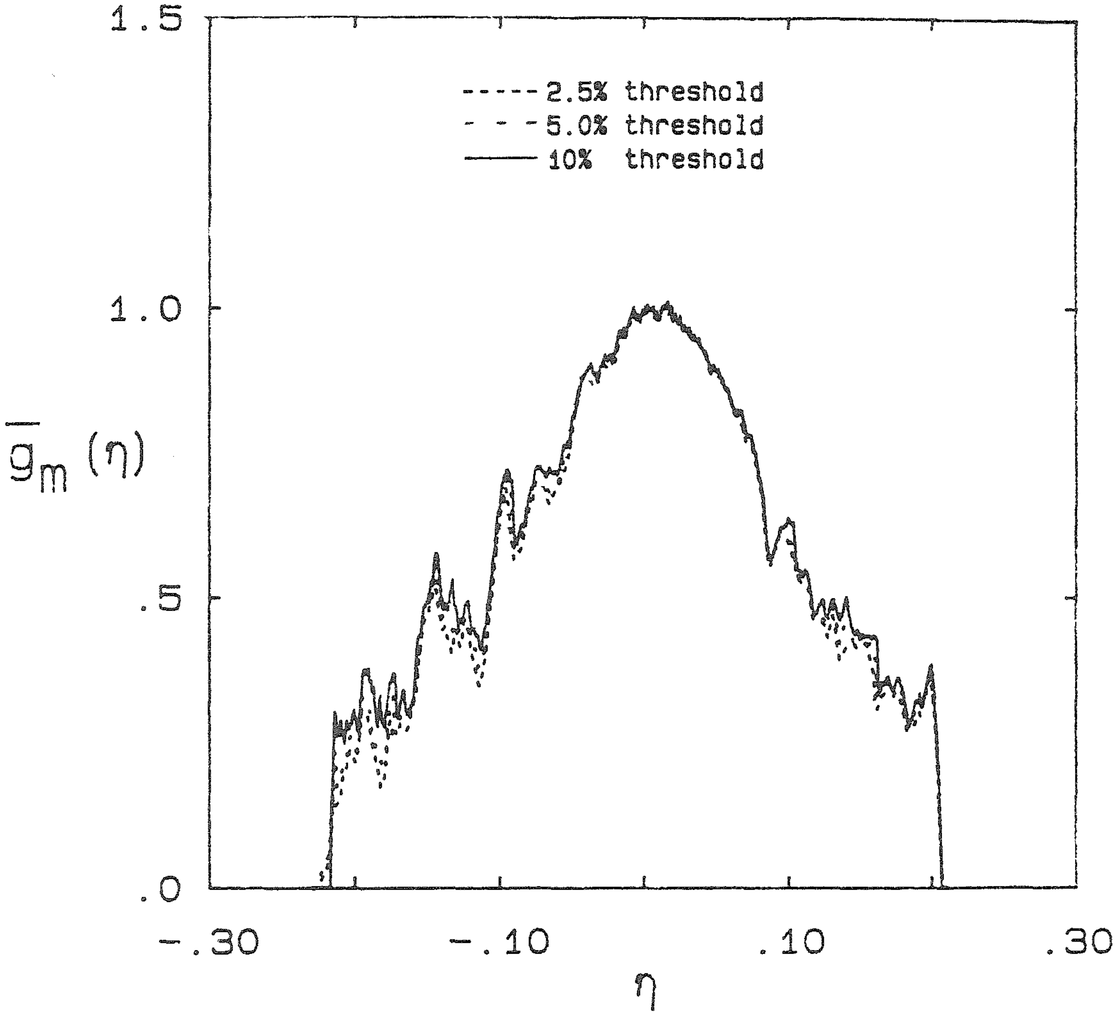

Figure 5-7. Effect of mixed/unmixed fluid threshold on $\overline{g}_m(\eta)$; $\chi = 300$, Re = 5,000, 1/4 of measurement duration.

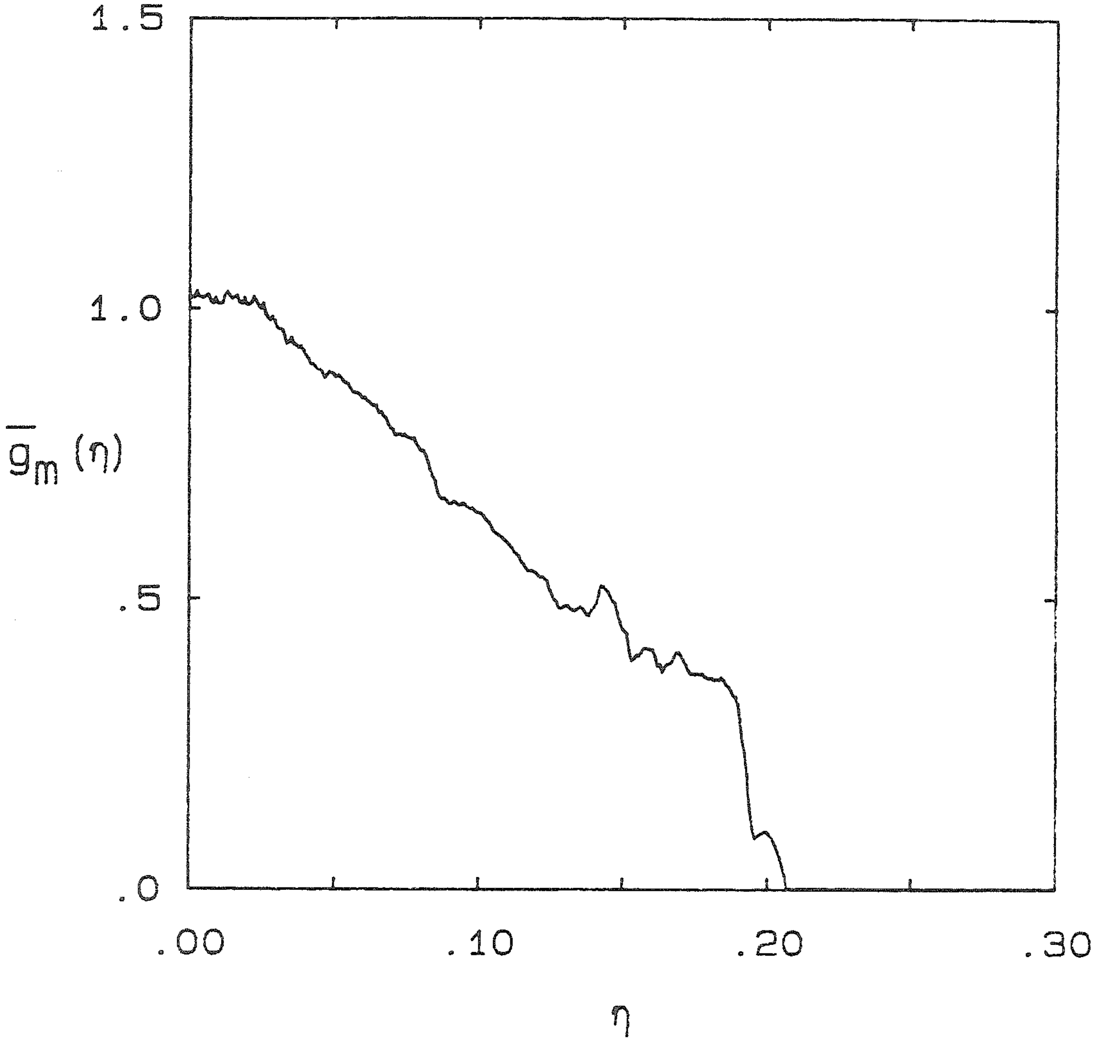

Figure 5-8. Mean radial profile of mixed fluid concentration; $\chi = 300$, $Re = 5{,}000$, 5% threshold.

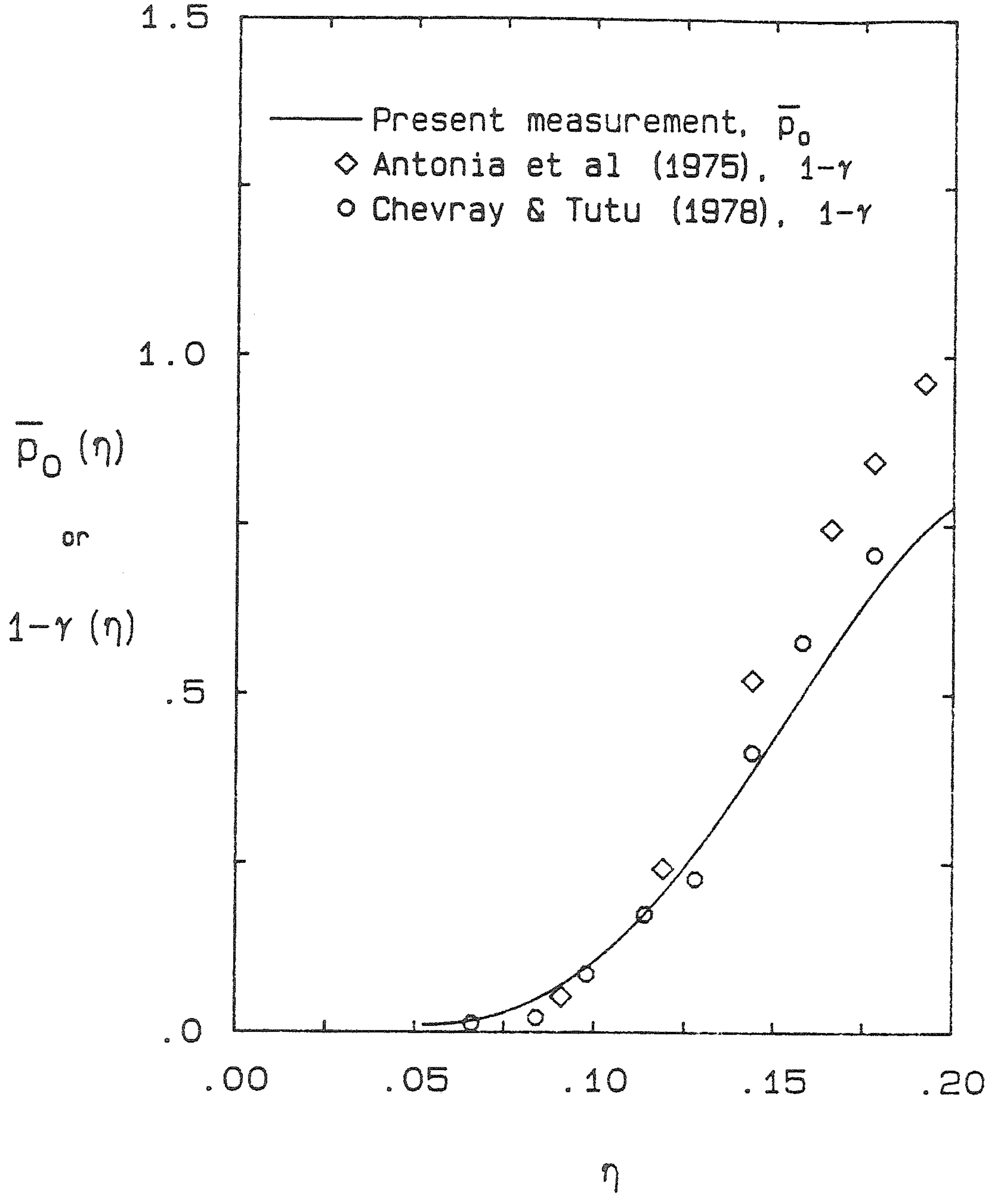

Figure 5-9. $\overline{p}_o(\eta)$ vs. η, $\chi = 300$, $Re = 5{,}000$; compared with "intermittency" from other experiments.

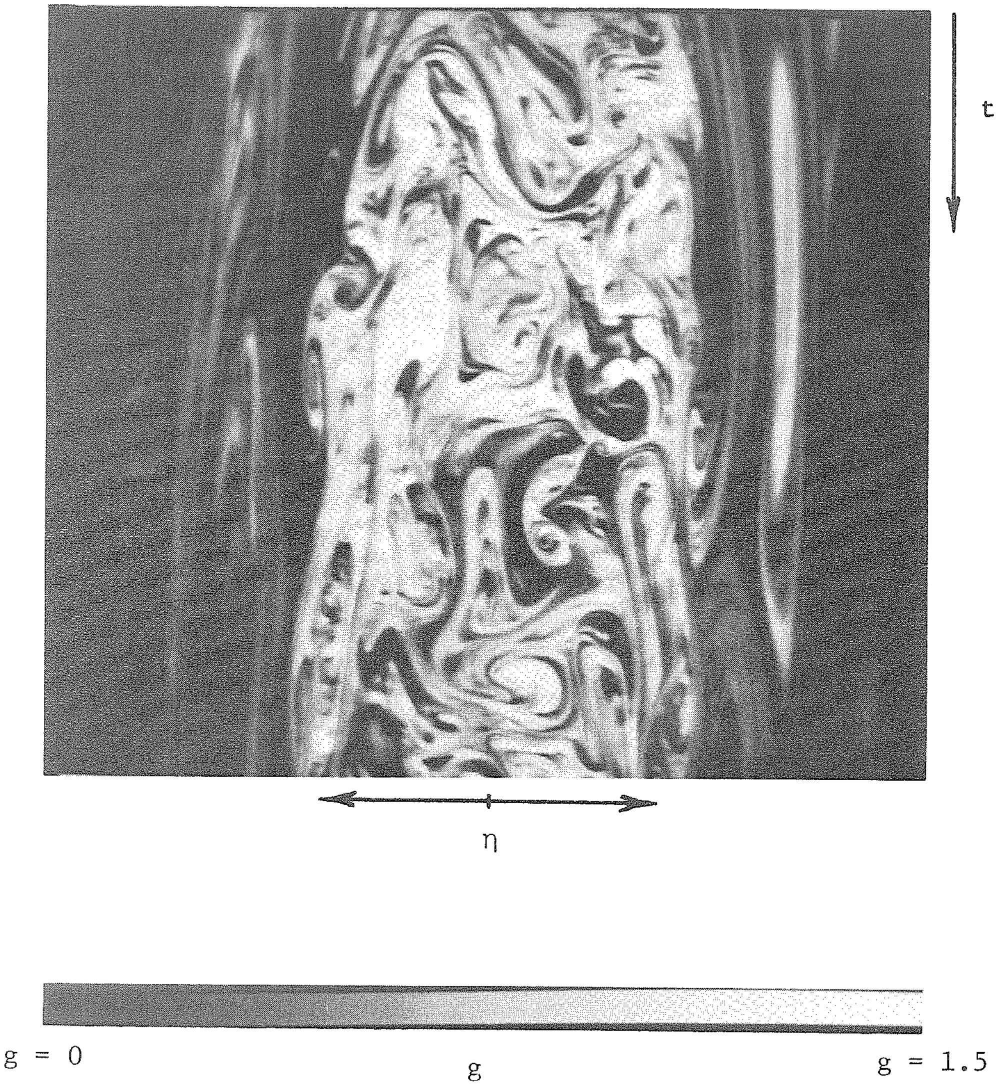

Figure 5-10a. η-t diagrams of the radial similarity concentration; $\chi = 300$, Re = 1,500, Monotone.

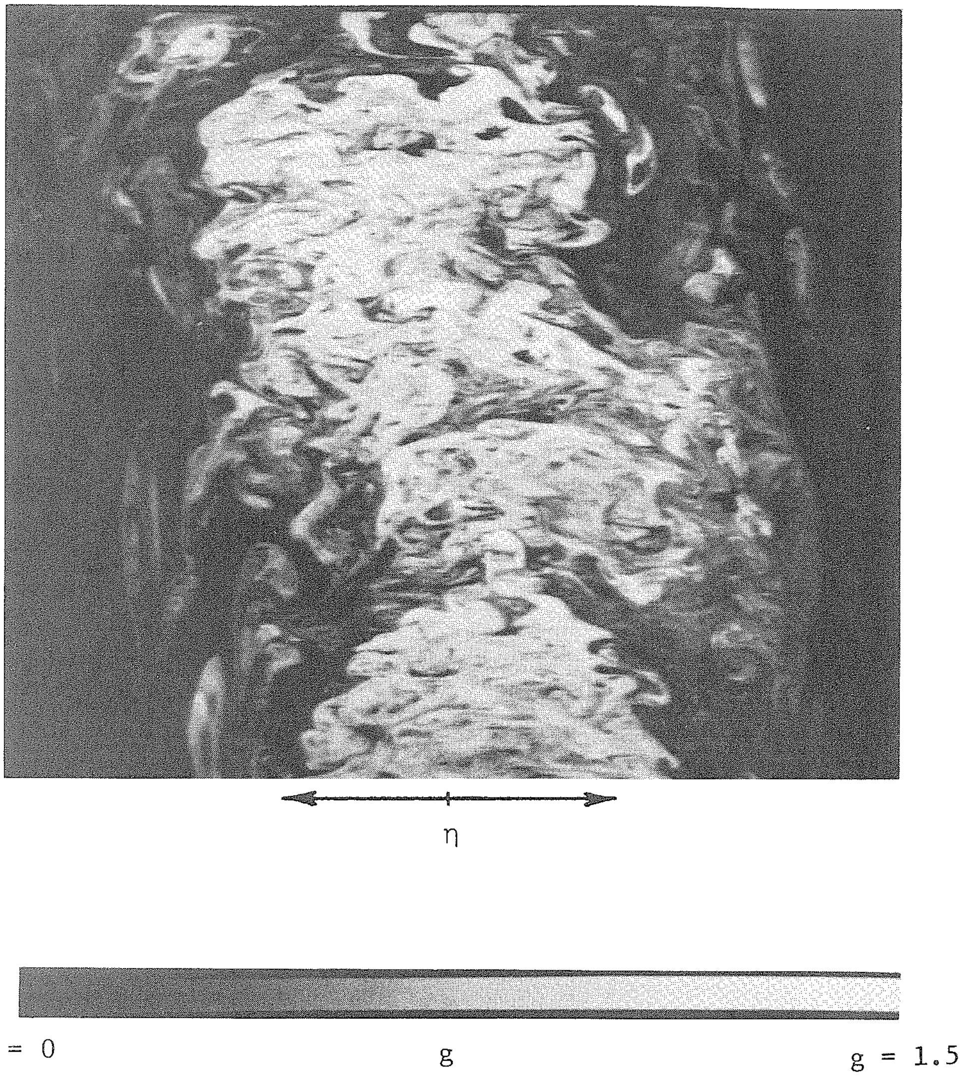

Figure 5-10b. η-t diagrams of the radial similarity concentration; $\chi = 300$, $Re = 5{,}000$, Monotone.

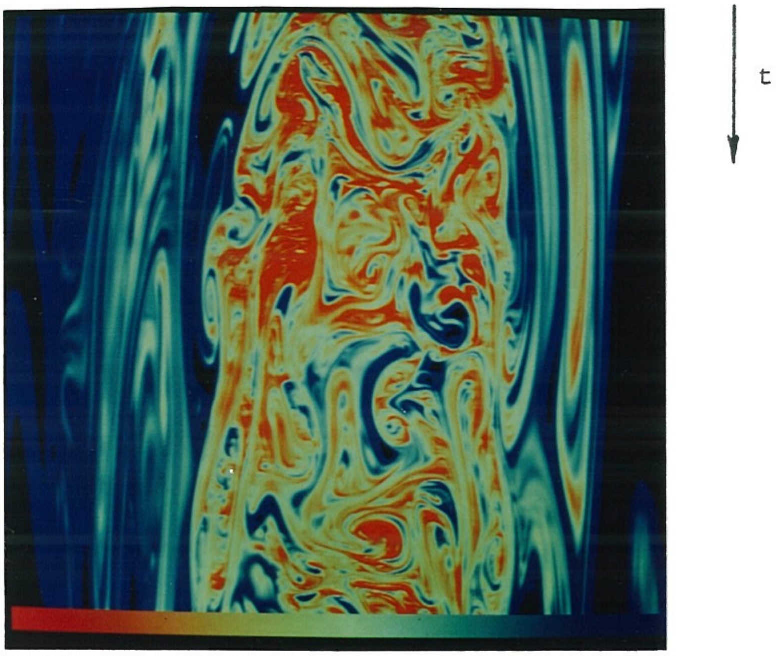

Figure 5-11a. η-t diagram of the radial similarity concentration; $\chi = 300$, Re = 1,500 , Pseudocolor.

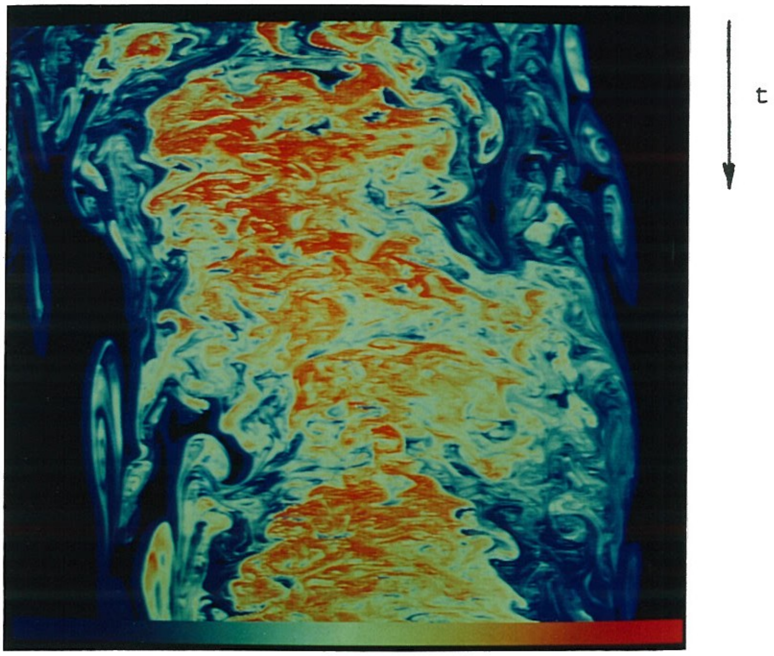

Figure 5-11b. η-t diagram of the radial similarity concentration $\chi = 300$, Re = 5,000 , Pseudocolor.

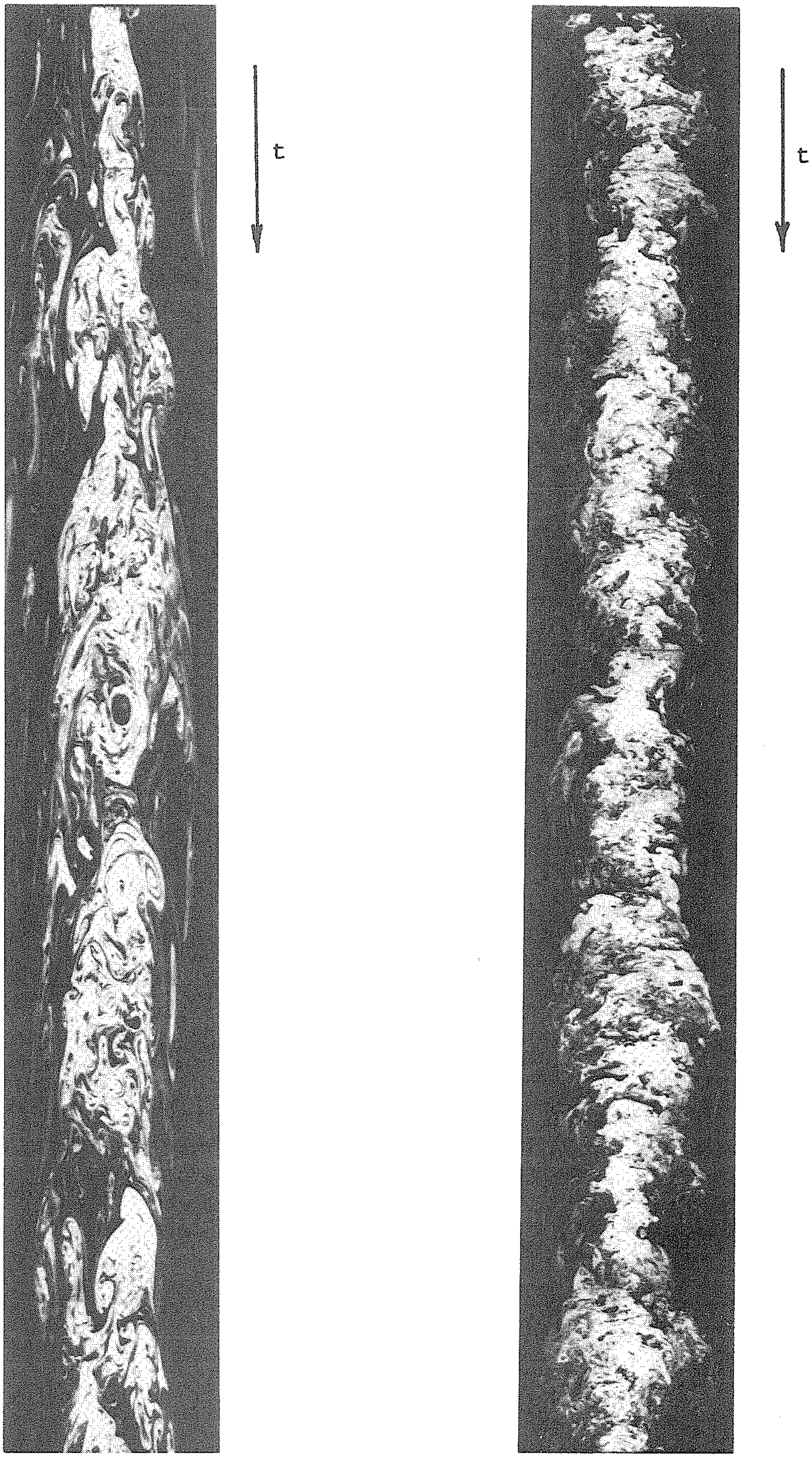

a. Re = 1,500

b. Re = 5,000

Figure 5-12. Composite η-t diagrams, $\chi = 300$.

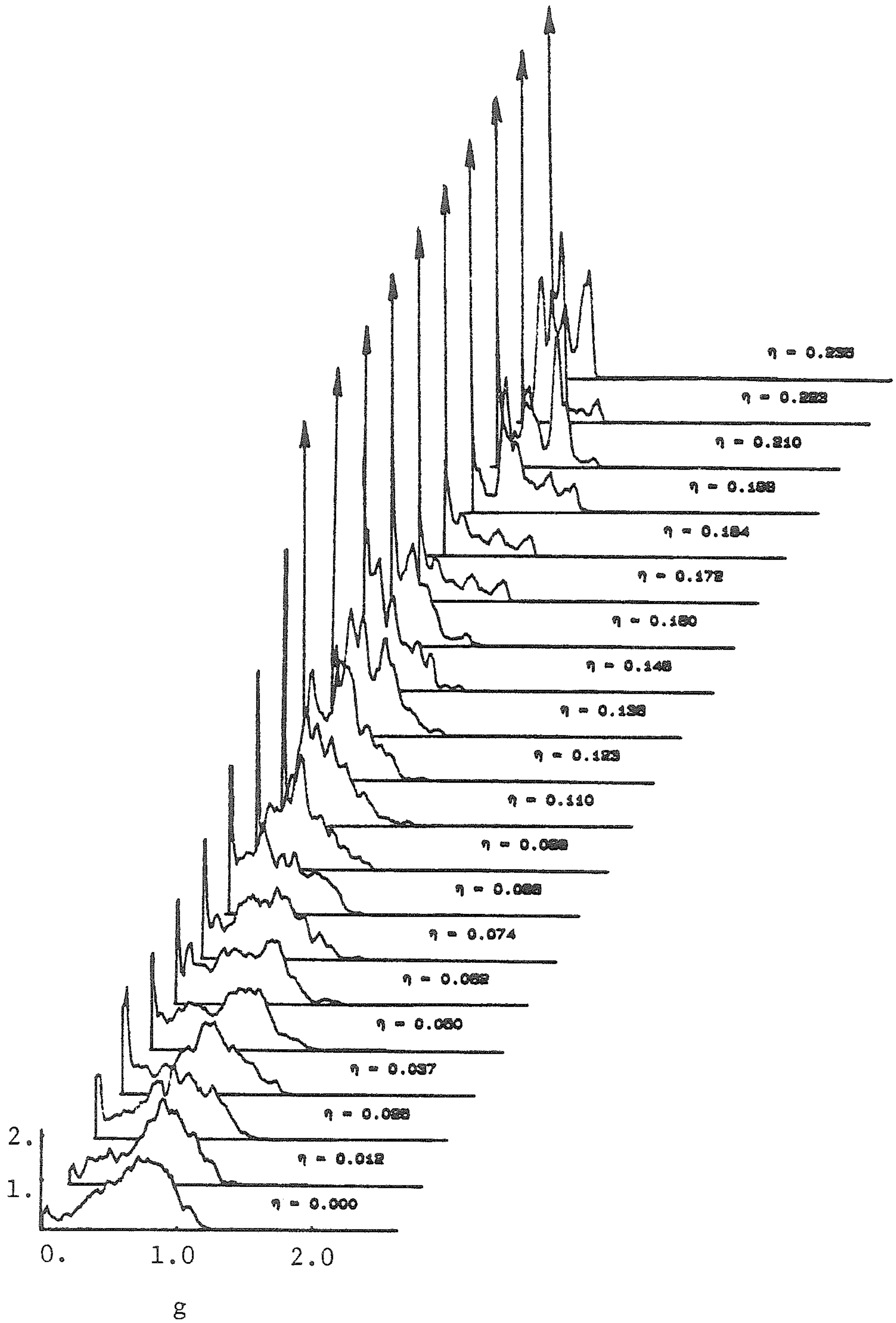

Figure 5-13a. PDFs of the radial similarity concentration; $\chi = 300$, $Re = 1,500$.

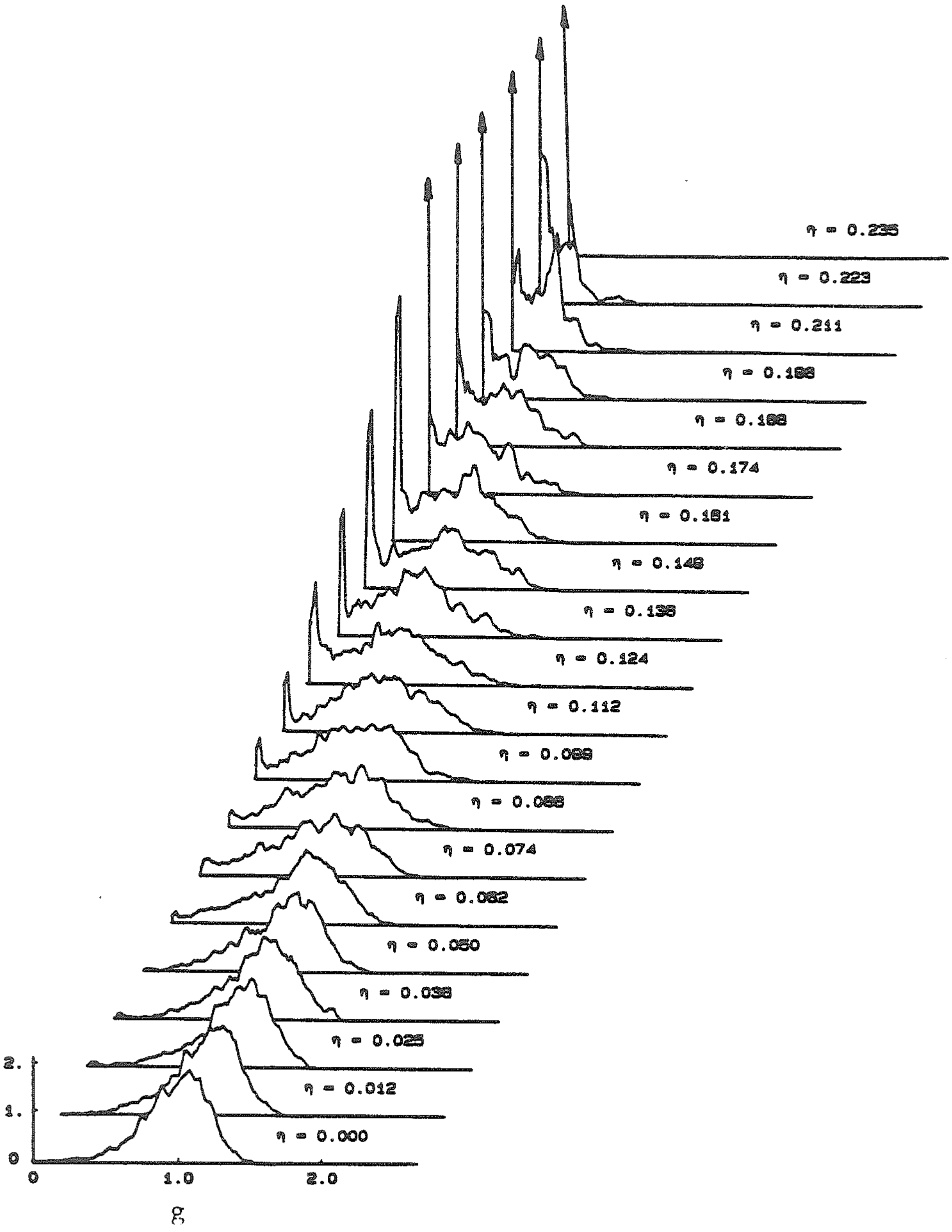

Figure 5-13b. PDFs of the radial similarity concentration; $\chi = 300$, $Re = 5{,}000$.